Numerical Simulation of Adiabatic Shear Bands and Crack Propagation in Thermoviscoplastic Materials

Matthew H. Lear

Dissertation submitted to the Faculty of the
Virginia Polytechnic Institute and State University
in partial fulfillment of the requirements for the degree of

Doctor of Philosophy
in
Engineering Mechanics

Prof. Romesh Batra, Chair
Prof. Rakesh Kapania
Prof. Liviu Librescu
Prof. Carl Prather
Prof. Surot Thangjitham

April 24, 2003
Blacksburg, Virginia

Keywords: MLPG method, finite element method, adiabatic shear band,
failure mode transition, dynamic fracture

Numerical Simulation of Adiabatic Shear Bands and Crack Propagation in Thermoviscoplastic Material

Matthew H. Lear

(Abstract)

Plane strain deformations of an elastoplastic material are studied using numerical methods. In the first chapter, a meshless formulation of the static small strain elastic-plastic problem is formulated using the meshless local Petrov-Galerkin method. The code is validated against the small strain plasticity routines in the commercial finite element code ABAQUS for two basic configurations with loading, unloading, and reloading. The results are found to agree within 5%. The validated code is then used to analyze the stress intensity factor (SIF) in a double edge-cracked plate. Deformations of the plate are studied both with and without exploiting the symmetry conditions. The penalty method is used to enforce the essential boundary condition in the former case. When analyzing the deformations of the entire plate, the diffraction method is employed in order to introduce the discontinuity in the displacement field across the crack faces. The log-log and a higher order extrapolation technique due to Dally and Berger (1996) are used to calculate the SIF. It is found that the penalty method was inadequate to enforce the essential boundary conditions in the vicinity of the crack tip and that in this region the deformations were oscillatory. Consequently, the SIF calculation using the higher order technique was not accurate. It is also found that for a small plastic zone (3% of the cracked length) the SIFs do not differ significantly from their

values for the corresponding linear elastic problem.

In the second chapter, a finite element formulation of the dynamic deformations of a microporous thermoviscoplastic solid is formulated. The heat conduction in a material is assumed to be governed by a hyperbolic heat equation; thus thermal and mechanical waves propagate with finite speeds. The formation and propagation of an adiabatic shear band (ASB) in plane strain tensile deformations is studied for eleven materials. The ASB is assumed to form when the maximum shear stress has been reduced to 80% of its peak value at a point and it is deforming plastically. The materials are ranked according their susceptibility to the formation of an ASB. A parametric study of the effect of the initial defect strength where the defect is assumed through an initially inhomogeneous distribution of porosity, the thermal conductivity, the thermal wave speed, and the applied strain-rate upon the ASB initiation and propagation is conducted. It is found that the susceptibility ranking for this configuration differs somewhat from that previously found for simple shear and torsion of thin-walled tubes. It is also found that thermal conductivity influences ASB initiation and propagation only for materials with large values of κ and that for such materials an adiabatic model may not be adequate. The effects of initial defect strength and the nominal strain-rates are both found to be consistent with simple shearing studies except that the ASB propagation speed was found to decrease with increasing nominal strain-rate. It is found that the criterion employed for ASB initiation accurately predicts the onset of the collapse of the total axial load applied to the body.

In the final chapter, the formulation from the previous chapter is modified to permit the formation and propagation of brittle and ductile fracture. Deformations of the impact loaded double edge-crack specimen of Kalthoff and Winkler (1987) are studied. The brittle to ductile failure mode transition with increasing impact speed was found. Previous studies have focused on identifying the transition speed and did not allow for crack propagation. In this study, crack propagation is achieved through a nodal release algorithm and interpenetration of the crack surfaces is prevented using stiff-spring contact elements. Brittle fracture is as-

sumed to occur when the maximum tensile principal stress achieves a critical value and the ductile fracture is assumed to occur when the effective plastic strain reaches a critical value. It is found that the transition speed for 4340 steel is approximately 54 m/s. For the brittle failure, the stress field is found to be significantly modified by the propagating crack and in the vicinity of the propagating crack the field is mode-I dominant. The crack formed through brittle fracture is found to completely propagate through the plate. For the ductile failure, the distribution of effective plastic strain about the crack tip is not significantly altered by the formation of the crack. The temperature rise in the vicinity of the ductile crack is found to be approximately 45% of the melting temperature of the material.

Acknowledgments

The author would like to express his deepest gratitude to his advisor Romesh C. Batra. Without his guidance and support this work would not have been possible. He would also like to thank his parents Carl and Sandra who gave him the confidence to try and the strength to persevere and his grandfather James L. Shoemaker who showed him that character and integrity still count for something. The author also would like to thank his first mentor and friend Dean "Dusty" Rhoads who gave him his first chance and continues to be an inspiration. To his dearest friend and eternal companion, Jennifer, the author can think of no words that adequately capture his feelings of love and appreciation – which (as she will most certainly remind him) shows he still doesn't know everything. And finally, though they are barely old enough to read this, the author owes all of his hopes, his dreams, and his happiness to his children Sam and Shannon whom he most sincerely wishes will someday surpass him.

Contents

1 Determination of Stress Intensity Factor from the Meshless Local Petrov-Galerkin (MLPG) Solution of an Elastoplastic Problem 1

1.1 Abstract 1

1.2 Introduction 1

1.3 Formulation of the Problem 3

1.4 Meshless Local Petrov-Galerkin (MLPG) Formulation of the Problem 6

1.5 Computation and Discussion of Results 9

1.5.1 Analysis of Two Problems for Code Validation 10

1.5.2 Determination of the SIF from the Far Field Solution 12

1.6 Conclusions 15

1.7 References 16

2 Adiabatic Shear Banding in Plane Strain Tensile Deformations of Eleven Thermoviscoplastic Materials with Finite Thermal Wave Speed 27

2.1 Abstract 27

2.2 Introduction 28

2.3 Formulation of the Problem 31

2.4 Weak Formulation of the Problem 36
2.5 Computation and Discussion of Results 38
2.5.1 Effect of Thermal Wave Speed 43
2.5.2 Ranking of the Eleven Materials According to the ASB Initiation Time 45
2.5.3 Effect of Thermal Conductivity 48
2.5.4 Effect of Nominal Strain-Rate 49
2.5.5 Variation of Effective Plastic Strain Along and Effective Plastic Strain Across an ASB 50
2.6 Conclusions 50
2.7 References 52

3 Simulation of Brittle and Ductile Fracture in an Impact Loaded Prenotched Plate 73

3.1 Abstract 73
3.2 Introduction 74
3.3 Formulation of the Problem 75
3.4 Computation and Discussion of Results 79
3.5 Conclusions 84
3.6 References 85

4 Contributions 101

4.1 Chapter 1 101
4.2 Chapter 2 101

4.3 Chapter 3 102

Vita **103**

List of Figures

1.1 Schematic sketch of (a) Problem A, and (b) Problem B, and time histories of the prescribed components of displacement 18

1.2 Comparison of the MLPG and the FE results for Problem A;

(a) Contours of the effective stress 19

(b) Variation of the effective stress at points on the centerline 19

(c) Variation of the effective stress at points on the bottom edge 20

1.3 Comparison of the MLPG and the FE results for Problem B;

(a) Time histories of the effective stress and the effective plastic strain at the point $x_1 = x_2 = 0.025$mm 21

(b) Effective stress vs. effective plastic strain at the point $x_1 = x_2 = 0.025$mm 21

(c) Contours of the effective stress in a small region around the lower left corner 22

1.4 Schematic sketch of a double-edge-cracked plate with axial displacements prescribed on the top and the bottom surfaces. Locations of the Cartesian and the cylindrical coordinate axes are also shown 23

1.5 (a) Vertical displacements of points on the crack axis computed when essential boundary conditions are enforced by the penalty method and when deformations of half of the plate are studied 24

(b) Distribution of the normal stress at points on the crack axis computed with the solutions of the quarter plate and the half plate problems 24

(c) Plastically deformed region around the crack-tip for $\Delta = 0.10$ mm 25

(d) Distance from the crack-tip of the farthest plastically deformed point on the crack axis vs. the axial displacement Δ 25

1.6 Mode-I stress intensity factor as a function of the applied axial displacement computed by;

(a) The plot of log (stress) vs. the log (distance from the crack tip) 26

(b) The Dally-Sanford method 26

2.1 Schematic sketch of the problem studied, and the time history of the applied axial velocity 59

2.2 Time histories of the effective plastic strain and the maximum shear stress at two material points W and P in a 4340 steel specimen;

(a) For point W within an ASB 60

(b) For point P outside of an ASB 60

2.3 Velocity distribution in the deformed configuration at an average axial strain of 0.35 61

2.4 Contours of the effective plastic strain in the deformed configuration at an average axial strain of 0.35 61

2.5 Time histories of the ASB length for six values of the thermal wave speed and the weak defect at the specimen centroid 62

2.6 Time histories of the ASB length for six values of the thermal wave speed and the weak defect at the specimen centroid 62

2.7 For the eleven materials studied, time histories of the length of an ASB for

(a) The weak defect 64

(b) The strong defect 66

2.8 For each one of the eleven materials studied, time histories of the evolution of

(a) The maximum shear stress 67

(b) The effective plastic strain 67

(c) The porosity 68

(d) The temperature at the centroid of the cross-section 68

2.9 Axial load vs. the effective plastic strain for 4340 steel, 7039 aluminum, and OFHC copper with the effective plastic strain from the Considerè condition (C), at the peak maximum shear stress (PS), and at shear band initiation (SB) indicated 69

2.10 Time histories of the length of the shear band for OFHC copper and 4340 steel; the solid and the dashed lines are respectively with and without the effects of heat conduction 69

2.11 Time history of the evolution of the maximum shear stress for OFHC copper at the centroid of the cross section with (solid line) and without (dashed line) the effects of heat conduction 70

2.12 For the 4340 steel using four values of the applied axial strain-rate, time histories of

(a) The evolution of the maximum shear stress 71

(b) The length of the ASB 71

2.13 (a) Variation of the effective plastic strain rate along an ASB in the 4340 steel 72

(b) Variation of the effective plastic strain across an ASB in the 4340 steel . 72

3.1 Schematic sketch of the problem studied. The notch tip radius is 0.15 mm . . 87

3.2 (a) Finite element discretization of the upper half of the plate 88

(b) The finite element mesh in a small region surrounding the notch tip. Locations of point B (50.09 mm, 25.20 mm) and point D (50.08 mm, 24.87 mm) where the maximum principal tensile stress and the maximum effective plastic strain occur are also indicated 88

3.3 For $v_o = 20$ m/s, contours of the nondimensional maximum principal stress for two meshes at $t = 20\mu$s. Dashed lines are for a mesh with 3,998 3-node elements, and solid lines are for a mesh of 8,712 3-node elements 89

3.4 For $v_o = 50$ m/s, contours of $\varepsilon_e^p/\varepsilon_c$ for two meshes at $t = 20\mu$s. Dashed lines are for a mesh with 3,998 3-node elements, and solid lines are for a mesh of 8,712 3-node elements 89

3.5 (a) Contours of the nondimensional maximum principal stress at $t = 18\mu$s for $v_o = 50$ m/s 90

(b) Contours of $\varepsilon_e^p/\varepsilon_c$ at $t = 15.1\mu$s for $v_o = 60$ m/s 90

(c) The variation of the nondimensional shear stress at points directly ahead of the notch tip 91

3.6 For $v_o = 20, 50$, and 60 m/s, the time history of the evolution of

(a) the nondimensional maximum principal stress at point B 92

(b) $\varepsilon_e^p/\varepsilon_c$ at point D 92

3.7 The dependance of the time of intiation of the brittle and the ductile fracture upon the impact speed, v_o 93

3.8 (a) For $v_o = 20$ m/s, contours of the nondimensional maximum principal stress around the notch tip at $t = 20\mu$s without the opening of a crack at the point where brittle failure initiates 94

(b) For $v_o = 20$ m/s, contours of the nondimensional maximum principal stress around the notch tip at $t = 20\mu$s with the opening of a crack at the point where brittle failure initiates 94

(c) For $v_o = 20$ m/s, contours of the nondimensional maximum principal stress at $t = 45\mu$s with the opening of a crack at the point where brittle failure initiates 95

3.9 (a) The time history of the crack length for brittle failure for $v_o = 20$ m/s and $v_o = 50$ m/s 96

(b) The deformed shape of the plate at $t = 100\mu$s for $v_o = 50$ m/s 96

3.10 For $v_o = 60$ m/s, contours of $\varepsilon_e^p/\varepsilon_c$ in a small region around the notch tip at

(a) $t = 15\mu$s 97

(b) $t = 21.5\mu$s 97

(c) $t = 28\mu$s 98

(d) $t = 33.5\mu$s 98

3.11 (a) The time history of $\varepsilon_e^p/\varepsilon_c$ at point D both with and without the opening of a crack at point B 99

(b) The time history of the nondimensional maximum principal stress at point B both with (solid line) and without (dotted line) the opening of a crack at point D 99

3.12 For $v_o = 60$ m/s, contours of the temperature rise in a small region around the notch tip at

(a) $t = 17.1\mu$s 100

(b) $t = 33.7\mu$s 100

List of Tables

2.1 For the 4340 steel and the weak defect, the initial and the final speeds of propagation of an ASB as a function of the thermal relaxation time 44

2.2 The ASB initiation times, and initial and final speeds of the ASB for four values of the average axial strain-rate 50

2.3 Values of thermomechanical parameters for the 11 materials studied 57

2.4 For the eleven material, values of the nominal strain, the effective plastic strain, and the homologeous temperature when the maximum shear stress peaks and when the ASB initiates. Values of the triaxialty ratio of the specimen centroid and the speed of an ASB are also listed 58

Chapter 1

Determination of Stress Intensity Factor from the Meshless Local Petrov-Galerkin (MLPG) Solution of an Elastoplastic Problem

1.1 Abstract

The meshless local Petrov-Galerkin (MLPG) method is used to analyze static infinitesimal elastoplastic deformations of an isotropic and homogeneous body. The validity of the code is established by comparing deformation fields of the MLPG solution of two problems with those obtained by the finite element method. The MLPG method is used to analyze mode-I deformations of a double edge-cracked plate. The stress intensity factor is determined by using the computed fields that are outside of the plastic zone developed at the stationary crack tip. For the size of the plastic zone equal to 3% of the crack length, the mode-I stress intensity factor is unaffected by the plastic deformations of the material near the crack tip.

1.2 Introduction

An advantage of a meshless method over the conventional finite element method of finding an approximate solution of a boundary-value problem is that in the meshless method nodes need not be connected to form closed polygons, and they can be placed somewhat arbitrarily

where needed to improve upon the accuracy of the computed solution. This is particularly advantageous in fracture mechanics problems since singular deformations near a crack tip can be easily analyzed.

Atluri and Zhu (1998, 2000) have developed a family of Meshless Local Petrov-Galerkin (MLPG) methods that require no background mesh to numerically evaluate integrals in the local weak formulation of the problem. Much of the work on the MLPG method can be found in Atluri and Shen's (2002) book. Kim and Atluri (2000) have demonstrated the use of the MLPG formulation in conjunction with the use of secondary nodes and no special crack tip modeling for finding accurately the mode-I stress intensity factor by the equivalent domain integration method. Ching and Batra (2001) used the MLPG method, basis functions enriched with those appropriate to describe singular deformation fields near a crack tip and either the visibility criterion of Belytschko et al. (1994) or the diffraction criterion of Organ et al. (1996) to analyze deformation fields near a crack tip in a single edge-cracked and a double edge-cracked plate. They exploited the symmetry of the problem about the crack axis and analyzed deformations of one-half of the plate. The computed stresses around the crack tip and the stress intensity factors were found to compare very well with analytical solutions of the corresponding problems. Batra and Ching (2002) have extended Ching and Batra's (2001) work to dynamic linear elastic fracture mechanics problems and computed the time histories of stress intensity factors for the following two problems: a rectangular plate with a central crack with plate edges parallel to the crack axis loaded in tension, and a double edge-notched plate with the edge between the notches loaded by compressive tractions. It was found that, for the double-edge notched orthotropic plate, the mode-mixity of deformations near a notch tip could be adjusted by suitably varying the in-plane elastic moduli of the plate material. Furthermore, the shear stress at points directly ahead of the notch tip exhibited a boundary layer effect near the notch tip. Rao and Rahman (2000) scrutinized, by the element free Galerkin (EFG) method coupled with the enriched basis functions and the diffraction criterion, stresses and deformations in an edge-cracked plate

with displacements given by the mode-I analytical solution prescribed on all edges. They employed a uniformly spaced mesh of 175 nodes with 13 nodes on each side. They used weight functions based on Student's t-distribution. Their computed values of the radial, the hoop and the shear stress matched well with the corresponding analytical values. Xu and Saigal (1998a,b) used the EFG method and the infinitesimal deformations theory to analyze stresses and deformations around the tip of a steadily propagating crack in an isotropic elastic and an isotropic elastic-plastic solid. Problems with known analytical solutions were solved to demonstrate the applicability of the EFG method. Here we use the MLPG method to study infinitesimal deformations of an isotropic and homogeneous elastoplastic body and also determine the stress-intensity factor (SIF) from the far field solution as proposed by Dally and Berger (1996).

The paper is organized as follows. Equations governing infinitesimal deformations of an elasto-plastic strain-hardening body are given in Section 2, and the MLPG formulation of the problem is described in Section 3. Section 4 compares results for two problems from the MLPG method with those obtained by using the finite element code ABAQUS. After having validated the MLPG code, the stress intensity factor (SIF) is computed for a double edge-cracked plate loaded in tension. Section 5 summarizes conclusions.

1.3 Formulation of the Problem

We use rectangular Cartesian coordinates to describe plane strain infinitesimal static elasto-plastic deformations (in the x_1x_2-plane) of an isotropic and homogeneous body occupying the region Ω in the reference configuration. In the absence of body forces, deformations are governed by the balance of linear momentum

$$\sigma_{ij,j} = 0 \qquad \text{in} \qquad \Omega,\ i,j = 1,2, \tag{1.1}$$

and boundary conditions

$$\begin{aligned} u_i &= \bar{u}_i \quad \text{on} \quad \Gamma_u, \\ t_i = \sigma_{ij} n_j &= \bar{t}_i \quad \text{on} \quad \Gamma_t. \end{aligned} \tag{1.2}$$

Here $\boldsymbol{\sigma}$ is the stress tensor, $\mathbf{u}$ the displacement, $\mathbf{t}$ the traction, $\mathbf{n}$ an outward unit normal to the boundary $\partial\Omega$ of Ω, $\sigma_{ij,j} = \partial\sigma_{ij}/\partial x_j$, $\mathbf{x}$ the position of a material particle, a repeated index implies summation over the range of the index, and Γ_u and Γ_t are parts of $\partial\Omega$ where displacements and tractions are prescribed respectively as $\bar{\mathbf{u}}$ and $\bar{\mathbf{t}}$. The strain tensor $\boldsymbol{\varepsilon}$ for infinitesimal deformations is related to displacements $\mathbf{u}$ by

$$\varepsilon_{ij} = (u_{i,j} + u_{j,i})/2. \tag{1.3}$$

We presume that the increment $d\boldsymbol{\varepsilon}$ in the strain tensor $\boldsymbol{\varepsilon}$ has additive decomposition into the elastic part $d\boldsymbol{\varepsilon}^e$ and the plastic part $d\boldsymbol{\varepsilon}^p$. That is

$$d\boldsymbol{\varepsilon} = d\boldsymbol{\varepsilon}^e + d\boldsymbol{\varepsilon}^p. \tag{1.4}$$

The elastic part of the incremental strain tensor is related to the stress increment $d\boldsymbol{\sigma}$ by Hooke's law

$$d\sigma_{ij} = D_{ijkl}\ d\varepsilon^e_{kl} \tag{1.5}$$

where $\mathbf{D}$ is a fourth-order tensor of elastic constants. For an isotropic and homogeneous body

$$D_{ijkl} = \frac{E}{2(1+\nu)}(\delta_{ik}\delta_{jl} + \delta_{il}\delta_{jk}) + \frac{E\nu}{(1+\nu)(1-2\nu)}\delta_{ij}\delta_{kl}, \tag{1.6}$$

where $0 < \nu < 0.5$ is Poisson's ratio, $E > 0$ the Young modulus and $\boldsymbol{\delta}$ the Kronecker delta.

We assume that plastic deformations of the body are governed by the von Mises yield criterion and the associated flow rule. Thus, plastic deformations ensue when

$$\phi \equiv \sigma_e - \sigma_y = 0,\ \sigma_e = \left(\frac{3}{2}s_{ij}s_{ij}\right)^{1/2},\ s_{ij} = \sigma_{ij} - \frac{1}{3}\sigma_{kk}\delta_{ij}, \tag{1.7}$$

and

$$d\varepsilon^p_{ij} = d\lambda\frac{\partial\phi}{\partial\sigma_{ij}} = d\lambda s_{ij}. \tag{1.8}$$

Here $d\lambda$ is a scalar, $\mathbf{s}$ the deviatoric stress tensor,σ_e the effective or the equivalent stress, and σ_y the yield stress of the material. Taking the inner product of each side of equation (1.8) with itself, we obtain $d\lambda = \frac{3}{2}\frac{d\varepsilon_e^p}{\sigma_y}$ where

$$d\varepsilon_e^p = \left(\frac{2}{3} d\varepsilon_{ij}^p d\varepsilon_{ij}^p\right)^{1/2} \tag{1.9}$$

is an increment in the equivalent (or the effective) plastic strain $\varepsilon_e^p = \int d\varepsilon_e^p$. Equation $(1.8)_1$ implies that the plastic part of the increment in strain is along the normal to the yield surface $\phi = 0$. For a strain-hardening material, σ_y depends upon the effective plastic strain ε_e^p; we take this dependence to be given by Swift's rule (1952)

$$\sigma_y = \sigma_0(1 + \varepsilon_e^p)^n, \tag{1.10}$$

where σ_0 is the initial yield stress in a quasistatic simple tension or compression test, and n is a material parameter. The stress state during continued plastic deformation satisfies $\phi = 0$. Thus $d\phi = 0$ and

$$s_{ij} ds_{ij} = \frac{2}{3}\sigma_y d\sigma_y = \frac{2}{3}\sigma_y \frac{d\sigma_y}{d\varepsilon_e^p} d\varepsilon_e^p. \tag{1.11}$$

By following the reasoning given, for example, by Hinton and Owen (1980), we conclude from (1.5), (1.8) and (1.11) that

$$d\sigma_{ij} = D_{ijkl}^{ep} d\varepsilon_{kl}, \tag{1.12}$$

where

$$D_{ijkl}^{ep} = \begin{cases} D_{ijkl} - \dfrac{D_{ijmn} s_{mn} D_{pqkl} s_{pq}}{\frac{4}{9}\frac{d\sigma_y}{d\varepsilon_e^p}\sigma_y^2 + s_{lm} D_{lmnp} s_{np}}, & \text{if} \quad \phi = 0, s_{ij} ds_{ij} \geq 0, \\ D_{ijkl}, & \text{if} \quad s_{ij} ds_{ij} < 0. \end{cases} \tag{1.13}$$

Equation (1.12) is the analog of Hooke's law (1.5) for an elastic-plastic material.

1.4 Meshless Local Petrov-Galerkin (MLPG) Formulation of the Problem

We follow Atluri and Zhu (1998, 2000) in deriving a meshless local Petrov-Galerkin formulation of the problem. Assume that several points, called nodes, have been located in Ω.

For each node, let Ω_s be a subdomain of Ω enclosing the node and $\boldsymbol{\psi}$ a test function defined on Ω_s. For node I we take Ω_s to be a circle centered at node I and of radius equal to the distance from node I to the nearest node. Taking the inner product of eqn. (1.1) with a test function $\boldsymbol{\psi}$ and of eqn. $(1.2)_1$ with $\alpha\boldsymbol{\psi}$, integrating the resulting equations over Ω_s and Γ_{su} respectively, and subtracting the second equation from the first equation we obtain

$$\int_{\Omega_s} \psi_i \sigma_{ij,j} d\Omega - \int_{\Gamma_{su}} \alpha\psi_i (u_i - \bar{u}_i) d\Gamma = 0, \tag{1.14}$$

where α is a penalty parameter and $\Gamma_{su} = \Gamma_u \cap \partial\Omega_s$ is the part of the boundary $\partial\Omega$ where essential boundary conditions (or displacements) are prescribed. The penalty parameter may be different at each point but is usually taken to be the same; henceforth we also set α = constant. Dimensions of α are N/m^3 and we take its value to be much larger than that of E/L where L is a typical length in Ω. This ensures that $u_i \simeq \bar{u}_i$ on Γ_{su}. Applying the divergence theorem to the first term on the left-hand side of eqn. (1.14) and setting $\sigma_{ij} n_j = t_i$ on $\partial\Omega_s$, we get

$$\int_{\Omega_s} \psi_{i,j} \sigma_{ij} d\Omega + \alpha \int_{\Gamma_{su}} \psi_i (u_i - \bar{u}_i) d\Gamma = \int_{\partial\Omega_s} t_i \psi_i d\Gamma. \tag{1.15}$$

We use the moving least squares (MLS) basis functions to approximate $\mathbf{u}(\mathbf{x})$ on Ω; (see Lancaster and Salkauskas, 1981). Let $\mathbf{u}^h(\mathbf{x})$ be an approximation of $\mathbf{u}(\mathbf{x})$ on Ω_s. We write $\mathbf{u}^h(\mathbf{x})$ as

$$u_k^h(\mathbf{x}) = \sum_{j=1}^{m} p_j(\mathbf{x}) a_{jk}(\mathbf{x}), \ k = 1, 2, \tag{1.16}$$

where $\mathbf{p}(\mathbf{x})$ with

$$p_1(\mathbf{x}) = 1, \ p_2(\mathbf{x}) = x_1, \ p_3(\mathbf{x}) = x_2, \ p_4(\mathbf{x}) = (x_1)^2, \ldots \tag{1.17}$$

is a complete monomial in x_1 and x_2 with m terms, and $\mathbf{a}(\mathbf{x})$ is the matrix of unknown functions to be determined. Krongauz and Belytschko (1996) have shown that any term in $\mathbf{u}^h(\mathbf{x})$ can be represented exactly by suitably enriching the monomials in (1.17). For problems involving stress singularities, terms such as $\sqrt{r}$, $\sqrt{r}\cos\theta/2$, $\sqrt{r}\sin\theta/2$ $\sqrt{r}\sin\frac{\theta}{2}\sin\theta$, $\sqrt{r}\cos\frac{\theta}{2}\sin\theta$ (e.g. see Flemming et al. (1997), Ching and Batra (2001)) may be added to

(1.17). We note that Kim and Atluri (2000) analyzed a crack problem without adding these terms. Here r is the distance of a point from the crack tip and θ its angular position with respect to the crack axis. In order to capture the singularity in the stress field in the vicinity of the crack tip, we take

$$\mathbf{p}^T(\mathbf{x}) = \{1,\ x_1,\ x_2,\ \sqrt{r}\}; \tag{1.18}$$

when solving a crack problem. Thus, $m = 4$ in eqn. (1.16). The a_{ij} in eqn. (1.16) is determined by minimizing

$$J = \sum_{i=1}^{n} W(\mathbf{x} - \mathbf{x}_i) \left[\sum_{j=1}^{m} p_j(\mathbf{x}_i) a_{jk}(\mathbf{x}) - \hat{u}_{ik} \right]^2,\ k = 1, 2, \tag{1.19}$$

with respect to a_{jk}. Here $\hat{u}_{ik}$ is the fictitious value of u^h_{ik} at $\mathbf{x} = \mathbf{x}_i$ and need not satisfy $\hat{u}_{ik} = u^h_k(\mathbf{x}_i)$. W is a weight function with non-negative values and a compact support. We take

$$W(\mathbf{x} - \mathbf{x}_i) = \begin{cases} \dfrac{e^{-\left(\frac{|\mathbf{x}-\mathbf{x}_i|}{c_i}\right)^2} - e^{-(r_i/c_i)^2}}{1 - e^{-(r_i/c_i)^2}}, & |\mathbf{x} - \mathbf{x}_i| \le r_i, \\ 0, & |\mathbf{x} - \mathbf{x}_i| \ge r_i, \end{cases} \tag{1.20}$$

where c_i is a constant that controls the shape of the function W, and is taken to equal the distance from the node at $\mathbf{x}_i$ to the third nearest non-repeating node as has been suggested by Lu et al. (1994). r_i should be chosen to include enough nodes so that equations resulting from the stationarity condition

$$\frac{\partial J}{\partial a_{jk}} = 0,\ j = 1, 2, \ldots, m;\ k = 1, 2, \tag{1.21}$$

can be solved for $\mathbf{a}$. However, a large value of n in eqn. (1.19) will make the solution lose its "local character" (Atluri and Zhu (2000)). We take $r_i = 4c_i$. Equations (1.19) and (1.21) give

$$\mathbf{a}(\mathbf{x}) = \mathbf{A}^{-1}(\mathbf{x})\mathbf{B}(\mathbf{x})\hat{\mathbf{u}}, \tag{1.22}$$

where

$$\mathbf{A}(\mathbf{x}) = \sum_{i=1}^{n} W(\mathbf{x} - \mathbf{x}_i)\mathbf{p}(\mathbf{x}_i)\mathbf{p}^T(\mathbf{x}_i) = \mathbf{A}^T(\mathbf{x}), \tag{1.23}$$

$$\mathbf{B}(\mathbf{x}) = [W(\mathbf{x} - \mathbf{x}_1)\mathbf{p}(\mathbf{x}_1),\ W(\mathbf{x} - \mathbf{x}_2)\mathbf{p}(\mathbf{x}_2), \ldots,\ W(\mathbf{x} - \mathbf{x}_n)\mathbf{p}(\mathbf{x}_n)]. \tag{1.24}$$

Substitution from (1.22) into (1.16) yields

$$u_k^h(\mathbf{x}) = \sum_{j=1}^{n} \phi_j(\mathbf{x}) \hat{u}_{jk}, \tag{1.25}$$

where

$$\phi_j(\mathbf{x}) = \sum_{i=1}^{m} p_i(\mathbf{x}) [\mathbf{A}^{-1}(\mathbf{x}) \mathbf{B}(\mathbf{x})]_{ji}, \ j = 1, 2, \ldots, n, \tag{1.26}$$

are the basis functions of the moving least squares (MLS) approximation. Equations (1.23), (1.24) and (1.26) imply that the smoothness and the support of the MLS basis functions depends upon the choice of the weight function W. We write the local weak form (1.15) for incremental displacements du_i and the resulting incremental stresses $d\sigma_{ij}$, substitute for $d\sigma_{ij}$ from (1.12), for $d\varepsilon_{ij}$ from (1.3), replace du_i by its approximation du_i^h and then substitute for du_i^h from (1.25) in terms of $d\hat{u}_{jk}$. The result is

$$\left[\int_{\Omega_s} \mathbf{B}_{\psi_i}^T \mathbf{D}^{ep} \mathbf{B}_{\phi_j} d\Omega + \alpha \int_{\Gamma_{su}} \boldsymbol{\psi}_i \mathbf{S} \phi_j d\Gamma \right] d\hat{\mathbf{u}}_j = \int_{\partial\Omega_s} \boldsymbol{\psi}_i \mathbf{t} d\Gamma + \alpha \int_{\Gamma_{su}} (\boldsymbol{\psi}_i \mathbf{S} d\bar{\mathbf{u}}) d\Gamma, \tag{1.27}$$

where

$$\begin{gathered} d\mathbf{u} = \{du_1 \ du_2\}^T, \ \boldsymbol{\psi}_i = \begin{bmatrix} \psi_i(\mathbf{x}) & 0 \\ 0 & \psi_i(\mathbf{x}) \end{bmatrix}, \ \mathbf{N} = \begin{bmatrix} n_1 & 0 & n_2 \\ 0 & n_2 & n_1 \end{bmatrix}, \\ \mathbf{B}_{\psi_i} = \begin{bmatrix} \dfrac{\partial \psi_i}{\partial x_1} & 0 \\ 0 & \dfrac{\partial \psi_i}{\partial x_2} \\ \dfrac{\partial \psi_i}{\partial x_2} & \dfrac{\partial \psi_i}{\partial x_1} \end{bmatrix}, \ \mathbf{B}_{\phi_j} = \begin{bmatrix} \dfrac{\partial \phi_j}{\partial x_1} & 0 \\ 0 & \dfrac{\partial \phi_j}{\partial x_2} \\ \dfrac{\partial \phi_j}{\partial x_2} & \dfrac{\partial \phi_j}{\partial x_1} \end{bmatrix}, \ \mathbf{S} = \begin{bmatrix} S_1 & 0 \\ 0 & S_2 \end{bmatrix}, \end{gathered} \tag{1.28}$$

where $\mathbf{t}$ is the incremental traction vector, and $\mathbf{n}$ is a unit outward normal to the boundary $\partial\Omega_s$ of Ω_s. $S_i = 1$ for u_i specified on Γ_u and $S_i = 0$ for u_i not specified on Γ_u. The first term on the right-hand side of (1.27) can be written as

$$\int_{\partial\Omega_s} \boldsymbol{\psi}_i \mathbf{t} d\Gamma = \int_{\Gamma_{su}} \boldsymbol{\psi}_i \mathbf{t} d\Gamma + \int_{\Gamma_{st}} \boldsymbol{\psi}_i \bar{\mathbf{t}} d\Gamma + \int_{L_s} \boldsymbol{\psi}_i \mathbf{t} d\Gamma, \tag{1.29}$$

where $\Gamma_{st} = \Gamma_t \cap \partial\Omega_s$ and $L_s = \partial\Omega_s - \Gamma_{st} - \Gamma_{su}$. Note that we have set $\mathbf{t} = \bar{\mathbf{t}}$ on Γ_{st}. We take the test function $\psi_i(\mathbf{x}) = W(\mathbf{x} - \mathbf{x}_i)$ except that r_i for $\psi_i(\mathbf{x})$ equals the distance from the node at $\mathbf{x}_i$ to the nearest node. Thus $\psi_i(\mathbf{x})$ vanishes on $\partial\Omega_s$. On Γ_{su}, we substitute

$\mathbf{t} = d\boldsymbol{\sigma}\mathbf{n} = \mathbf{N}\mathbf{D}^{ep}\mathbf{S}\mathbf{B}_{\phi_j} d\mathbf{u}_j$ and transfer this term to the left-hand side of (1.27). We thus arrive at

$$\left[\int_{\Omega_s} \mathbf{B}_{\psi_i}^T \mathbf{D}^{ep} \mathbf{B}_{\phi_j} d\Omega + \int_{\Gamma_{su}} (\alpha \boldsymbol{\psi}_i \mathbf{S} \boldsymbol{\phi}_j - \boldsymbol{\psi}_i \mathbf{N}\mathbf{D}^{ep}\mathbf{S}\mathbf{B}_{\phi_j}) d\Gamma\right] d\hat{\mathbf{u}}_j = \int_{\Gamma_{st}} \boldsymbol{\psi}_i \bar{\mathbf{t}} d\Gamma + \alpha \int_{\Gamma_{su}} (\boldsymbol{\psi}_i \mathbf{S} d\bar{\mathbf{u}})\, d\Gamma, \tag{1.30}$$

which we write as

$$\mathbf{K}^{ep} d\hat{\mathbf{u}} = d\mathbf{F}. \tag{1.31}$$

Here $\mathbf{K}^{ep}$ is the stiffness matrix for elastic-plastic deformations and $d\mathbf{F}$ is the increment in the load vector. Equations like (1.31) are written for each node in Ω. In the MLPG method, no assembly of equations is required.

1.5 Computation and Discussion of Results

The prescribed displacements and/or prescribed tractions are applied incrementally. Typically, either prescribed tractions or prescribed displacements are null and the difficulty of properly incrementing simultaneously displacements and tractions is avoided. For problems studied herein $\bar{\mathbf{t}} = \mathbf{0}$. During each increment in prescribed displacements, deformations of the body are first assumed to be elastic. After having solved equations (1.31) for the incremental displacements, incremental strains and hence incremental stresses are computed at each integration point. These are added to their previous respective values to get total strains and stresses. If the stress state even at one integration point lies outside the yield surface, the radial return algorithm is used to correct the computed incremental displacements. Since this is done without using the equilibrium equations (1.31), an iterative procedure is adopted to ensure that equilibrium is not violated. The solution is assumed to have converged when the sum of the magnitude of residual loads at all nodes where displacements are not prescribed is smaller than a pre specified percentage (δ) of the sum of the magnitudes of reactions at nodes where displacements are prescribed. Solutions of problems studied in this paper were obtained with $\delta = 0.5\%$.

1.5.1 Analysis of Two Problems for Code Validation

Equations of section 4 are used to develop a computer code. The domain integrals in equation (1.30) are evaluated numerically by using an 8×8 quadrature rule, and the line integrals with 8 integration points. The code is validated by comparing solutions from it for problems A and B illustrated respectively in Fig. 1.1a and 1.1b with those obtained by using the small strain elastoplasticity option in the finite element (FE) code ABAQUS. The time histories of the prescribed displacements are indicated in these Figs. Note that the time here is a dummy variable since a static problem is being solved. Values assigned to different material parameters are

$$E = 1\,\text{kPa}, \quad \nu = 0.25, \quad \sigma_0 = 100\,\text{Pa}, \quad n = 1.0. \tag{1.32}$$

For Δ(see Fig. 1.1a) = 0.2m, Figs. 1.2a, 1.2b and 1.2c depict respectively for Problem A contours of the effective stress in a small region surrounding the lower left corner, the variation of the effective stress at points on the bottom surface, and the variation of the effective stress at points on the midsurface. A large value has been purposely assigned to Δ so that differences, if any, between the MLPG and the FE solutions are noticeable even though the assumption of small strains is clearly violated. It is apparent from the results plotted in Figs. 1.2a-1.2c that the MLPG solution is very close to the FE solution; the maximum difference between the two solutions at any point is less than 5%. The MLPG solution is based on 441 uniformly distributed nodes. For the FE solution, a regular mesh of 2,025 8-node quadrilateral elements with a 3×3 Gauss integration rule is employed. A very fine FE mesh is used since this solution is taken as the reference solution for comparison purposes. It is interesting to observe that a rather coarse placement of nodes for the MLPG method gives very good values of the effective stress and the effective plastic strain throughout the entire domain. Contour plots of Fig. 1.2a evince that high values of the effective stress occur at the lower left corner. The effective stress at each corner on the left edge was found to be more than that at the corresponding corner on the right edge.

An objective of analyzing Problem B is to illustrate that the code can accurately model loading and unloading. Accordingly, time histories of the effective stress and the effective plastic strain at the material point located at $x_1 = x_2 = 0.025$mm are plotted in Figs. 1.3a and 1.3b respectively. It is obvious that the MLPG and the FE solutions are very close to each other. Also the MLPG code models elastic unloading correctly since the effective plastic strain remains unchanged when the material point unloads as signified by the drop in the effective stress. The FE results were computed by using the same mesh as that for Problem A. 1,326 uniformly placed nodes in the lower half of the domain with 51 nodes on the horizontal axis were used for the MLPG solution. Significantly more nodes are needed to accurately capture the deformation during the loading and the unloading than when prescribed displacements are increased monotonically and material points do not unload. Because of the symmetry of the problem about the horizontal centroidal axis, deformations of only the lower half of the plate were analyzed. The distributions of the effective stress and the effective plastic strain computed by the MLPG and the FE methods are found to be very close to each other as for Problem A. As should be evident from the contours of the effective stress near the lower left corner plotted in Fig. 1.3c, stresses are high at points adjacent to the corner.

1.5.2 Determination of the SIF from the Far Field Solution

We study infinitesimal plane strain elasto-plastic deformations of a double edge-cracked isotropic and homogeneous plate deformed in mode-I by prescribing axial displacements on its upper and the lower surfaces. In a laboratory it is easier to use a hard loading device that applies displacements than a soft loading device that prescribes tractions. A sketch of the problem, and locations of the Cartesian and the cylindrical coordinate axes are shown in Fig. 1.4. Because of the symmetry of the geometry and the boundary conditions about the horizontal and the vertical centroidal axes, deformations of only the upper left quarter of the plate are analyzed by the MLPG method. Various parameters are assigned the following

values.

$$E = 210 \text{ GPa},\ \nu = 0.27,\ \sigma_0 = 792.2 \text{ MPa},\ n = 1,\ a = 50 \text{ mm}. \tag{1.33}$$

Sixty-one nodes are placed uniformly in the x_1 and the x_2-directions. Area and line integrals in the weak formulation (1.30) are evaluated numerically by using 8×8 and 8 Gauss integration points respectively.

In order to check if the penalty method satisfactorily enforces the condition of null vertical displacements at points on the crack axis that are adjacent to the crack tip, the problem for the left half of the plate was analyzed by the MLPG method. For the half plate no boundary conditions are needed at nodes on the crack axis. Note that the crack faces are traction free. The crack is modeled as a notch of infinitesimally small radius. The diffraction criterion (e.g. see Organ et al. (1996)) is used to account for the discontinuity in the normal component of the displacement gradients at points on the crack plane. For $\Delta = 0.1$ mm, Figures 1.5a and 1.5b show respectively the vertical displacement of a point on the crack axis and the variation with the distance from the crack tip of the normal stress. It is clear that the penalty method does not adequately enforce the condition of zero vertical displacement at points on the crack axis that are close to the crack tip. Various values of the penalty parameter gave essentially the same result. The magnitudes of deviations in the vertical displacement and the normal stress are maximum for a point on the crack tip and diminish to essentially zero for points with $r/a \geq 0.2$.

Figure 1.5c depicts the plastically deformed region with $\varepsilon_e^p > 0$ around the crack tip for $\Delta = 0.10$ mm, and Fig. 1.5d gives the distance from the crack tip of the farthest plastically deformed point on the crack axis vs. the axial displacement Δ. Thus the area of the plastically deformed zone increases monotonically but not linearly with an increase in the applied axial displacement. Not only material points ahead of the crack tip but those behind it have also been plastically deformed. The size of the plastic zone is small as compared to the crack length and the specimen dimensions, and its shape shown in Fig. 1.5c resembles

that depicted schematically in Figs. 2.32 and 2.33 of Anderson's (1991) book.

For a linear elastic cracked plate and in the limit of $r \to 0$, the stress field (e.g. see Dally and Berger (1996)) at points near the crack-tip is given by

$$\begin{aligned}
\sigma_{11} &= A_0 \left(\cos\frac{1}{2}\theta - \frac{1}{2}\sin\theta \sin\frac{3}{2}\theta \right) r^{-1/2} + 2B_0 + A_1 \left(\cos\frac{1}{2}\theta - \frac{1}{2}\sin\theta \sin\frac{1}{2}\theta \right) r^{1/2} \\
&\quad + B_1(2\cos\theta)r + A_2 \left(\cos\frac{3}{2}\theta - \frac{3}{2}\sin\theta \sin\frac{1}{2}\theta \right) r^{3/2} + B_2(2 - 6\sin^2\theta)r^2, \\
\sigma_{22} &= A_0 \left(\cos\frac{1}{2}\theta + \frac{1}{2}\sin\theta \sin\frac{3}{2}\theta \right) r^{-1/2} + A_1 \left(\cos\frac{1}{2}\theta - \frac{1}{2}\sin\theta \sin\frac{1}{2}\theta \right) r^{1/2} \\
&\quad + A_2 \left(\cos\frac{3}{2}\theta + \frac{3}{2}\sin\theta \sin\frac{1}{2}\theta \right) r^{3/2} + B_2(2\sin^2\theta)r^2, \\
\sigma_{12} &= A_0 \left(\frac{1}{2}\sin\theta \cos\frac{3}{2}\theta \right) r^{-1/2} + A_1 \left(-\frac{1}{2}\sin\theta \cos\frac{1}{2}\theta \right) r^{1/2} + B_1(-2\sin\theta)r \\
&\quad + A_2 \left(-\frac{3}{2}\sin\theta \cos\frac{1}{2}\theta \right) r^{3/2} + B_2(4\sin\theta\cos\theta)r^2,
\end{aligned} \tag{1.34}$$

where $A_0,\ A_1,\ A_2,\ B_0,\ B_1$ and B_2 are constants, and (r, θ) are cylindrical coordinates of a point with the origin at the crack-tip. The mode-I SIF, K_I, equals $\sqrt{2\pi}\ A_0$. Thus

$$K_I = \lim_{r\to 0} \sqrt{2\pi r}\ \sigma_{22}(r, 0) = \lim_{r\to 0} \sqrt{2\pi r}\sigma_{22}(r, \theta) / \left(\cos\frac{1}{2}\theta + \frac{1}{2}\sin\theta \sin\frac{3}{2}\theta \right). \tag{1.35}$$

Since the material around the crack-tip is always deformed plastically, Dally and Berger (1996) postulated that eqns. (1.34) are valid at points outside of the plastically deformed region that are not too far from the crack-tip. Here constants $A_0,\ A_1,\ A_2,\ B_0,\ B_1$ and B_2 are evaluated by the least squares method from the values of stresses at 50 points in the region $0.2 \le r/a \le 0.3$.

For reference, the stress intensity factor for a linear elastic double edge notched plate loaded in tension by axial surface traction σ_∞ is given by (Tada et al. (1985))

$$K_I = \sigma_\infty \left(\frac{\pi a W}{2(W-a)} \right)^{1/2} \left[1.122 - 0.561\left(\frac{a}{W}\right) - 0.205\left(\frac{a}{W}\right)^2 + 0.471\left(\frac{a}{W}\right)^3 + 0.190\left(\frac{a}{W}\right)^4 \right] \tag{1.36}$$

where W is the plate width. With $a = 50$ mm and $W = 100$ mm in the present problem,

$$K_I/\sigma_\infty = 0.341\sqrt{m}. \tag{1.37}$$

σ_∞ is evaluated by averaging the normal reactions at points on the top surface of the plate which are determined from the computed displacement field. For $\Delta = 0.02$ mm, $\sigma_\infty =$ 32 MPa, and values of K_I/σ_∞ determined from the solution of the 1/4 plate and the 1/2 plate problems equal $0.41\sqrt{m}$ and $0.425\sqrt{m}$ which differ from the analytical values by about 20%. Reasons for these differences include the following. The distance 100 mm of the loaded surface from the crack face is not sufficient to satisfy the requirement that it be far from the crack face. Computed normal tractions on the top surface are not uniformly distributed as assumed in relation (1.36). Dally and Berger (1996) also found that the value of K_I computed from the far field solution differed from the analytical value for the linear elastic problem by about 20%.

Figure 1.6a,b exhibits the value of K_I as a function of the applied axial displacement Δ. Values of K_I were computed from stresses along three radial lines $\theta = 0°$, $30°$ and $60°$. The data on line $\theta = 0°$ was smoothened by averaging over five consecutive points; no smoothening was done for the data on lines $\theta = 30°$ and $60°$. The penalty method did not adequately satisfy the essential boundary conditions at nodes on the line $\theta = 0°$ and the resulting stresses were oscillatory. Values of K_I obtained by the Dally-Sanford method from the unsmoothened data at points on the line $\theta = 0°$ plotted in Fig. 1.6b are essentially meaningless. However, values obtained from the smoothened data agree well with those found from stresses at points on the lines $\theta = 30°$ and $60°$. Results plotted in Fig. 1.6a,b reveal that the mode-I stress intensity factor increases essentially linearly with an increase in the applied axial displacement. The slight deviation from the linear relationship occurs at an axial displacement of 0.06 mm; it is too small to be deciphered from the plots of Fig. 1.6a,b. For an applied axial displacement of 0.13 mm, the size of the plastic zone developed around the crack tip (cf. Fig. 1.5d) is about 1.4 mm which is 3% of the crack length. Thus the plastically deformed region around the crack tip is not large enough to significantly alter the mode-I stress intensity factor, and Irwin's (1961) correction of increasing the crack length by $a_y = \frac{1}{6\pi}\left(\frac{K_I}{\sigma_y}\right)^2$ is miniscule as compared to the length of the original crack.

1.6 Conclusions

We have analyzed plane strain static infinitesimal elastoplastic deformations of an isotropic and homogeneous body by using the incremental theory of plasticity and a meshless local Petrov-Galerkin (MLPG) method. Plastic deformations obey the von Mises yield criterion and the associated flow rule. The MLPG solutions for two problems are found to compare very well with their solutions by the finite element method. Whereas a coarse placement of nodes in the MLPG method is adequate during the monotonic loading of material points, a finer placement of nodes is needed when there is loading, unloading and reloading. The MLPG solution and the Dally-Berger technique are used to find the mode-I stress intensity factor of a double edge-cracked elastoplastic plate. The penalty method does not adequately satisfy the essential boundary condition at the node located on the crack-tip resulting in a somewhat oscillatory stress field ahead of the crack-tip. The mode-I stress intensity factor is unaffected by the development of the small (size equal to 3% of the crack length) plastically deformed region around the crack tip.

1.7 References

Anderson T. (1991): *Fracture Mechanics - Fundamental and Applications.* CRC Press, Boca Raton.

Atluri S.N. and Zhu T.L. (1998): A new Meshless Local Petrov-Galerkin (MLPG) Approach in Computational Mechanics. *Comp. Mech.*, Vol. 22, pp. 117-127.

Atluri S.N. and Zhu T.L. (2000): The Meshless Local Petrov-Galerkin (MLPG) Approach for Solving Problems in Elasto-Statics. *Comp. Mech.*, Vol. 25, pp. 169-179.

Atluri S.N. and Shen S.P. (2002): The Mesless Local-Petrov Galerkin (MLPG) Method. Tech Science Press.

Batra R.C. and Ching H.K. (2002): Analysis of Elastodynamic Deformations near a Crack/Notch Tip by the Meshless Local Petrov-Galerkin (MLPG) Method. *Comp. Modeling in Eng'g Sci.*, Vol. 3, pp.

Ching H.K. and Batra R.C. (2001): Determination of Crack Tip Fields in Linear Elastostatics by the Meshless Local Petrov-Galerkin (MLPG) Method. *Comp. Modeling Eng. Sci.*, Vol. 2, pp. 273-289.

Dally J.R. and Berger J.W. (1996): A Strain Gage Method for Determining K_I and K_{II} in a Mixed Mode Stress Field. *SEM Spring Conference on Experimental Mechanics*, pp. 603-612.

Flemming M., Chu Y., Moran B. and Belytschko T. (1997): Enriched Element-Free Galerkin Methods for Crack Tip Fields. *Int. J. Num. Methd. Engr.*, Vol. 40, pp. 1483-1504.

Irwin G. (1961): Plastic Zone Near a Crack and Fracture Toughness. *Sagamore Research Conference Proceedings*, Vol. 4, pp. 63-78.

Kim H.G. and Atluri S.N. (2000): Arbitrary Placement of Secondary Nodes and Error Control in the Meshless Local Petrov-Galerkin (MLPG) Method. *Comp. Modeling in Engr. and Sci.*, Vol. 1, pp. 11-32.

Krongauz Y. and Belytschko T. (1996): Enforcement of Essential Boundary Conditions in Meshless Approximations using Finite Elements. *Computer Methods in Applied Mechanics and Engineering*, Vol. 131, pp. 133-145.

Lancaster P. and Salkauskas, K. (1981): Surfaces Generated by Moving Least Squares Methods. *Meth. Comput.*, Vol. 37, pp. 141-158.

Lu Y.Y., Belytschko T. and Gu L. (1994): A New Implementation of the Element Free Galerkin Method. *Comp. Meth. Appl. Mech. Engr.*, Vol. 113, pp. 397-414.

Organ D.J., Fleming M. and Belytschko T. (1996): Continuous Meshless Approximations for Nonconvex Bodies by Diffraction and Transparency. *Computational Mechanics*, Vol. 18, pp. 225-235.

Owen D. and Hinton E. (1980): *Finite Elements in Plasticity - Theory and Practice*, Pineridge Press Limited, Swansea, UK.

Rao B.N. and Rahman S. (2000). Efficient Meshless Method for Fracture Analysis of Cracks. *Comp. Mech.*, Vol. 26, pp. 298-308.

Swift H.W. (1952): Plastic Instability Under Plane Stress. *J. Mech. Phys. Solids*, Vol. 1, pp. 1-18.

Tada H., Paris, P.C. and Irvin, G.R. (1985): *The Stress Analysis of Cracks Handbook*, 2nd Ed. Paris Productions Inc., St. Louis.

Xu Y. and Saigal S. (1998a): An Element Free Galerkin Formulation for Stable Crack Growth in an Elastic Solid. *Comp. Meth. Appl. Mech. Engr.*, Vol. 154, pp. 331-343.

Xu Y. and Saigal S. (1998b): Element Free Galerkin Study of Steady Quasi-static Crack Growth in Plane Strain Tension in Elastic-plastic Materials. *Comp. Mech.*, Vol. 22, pp. 255-265.

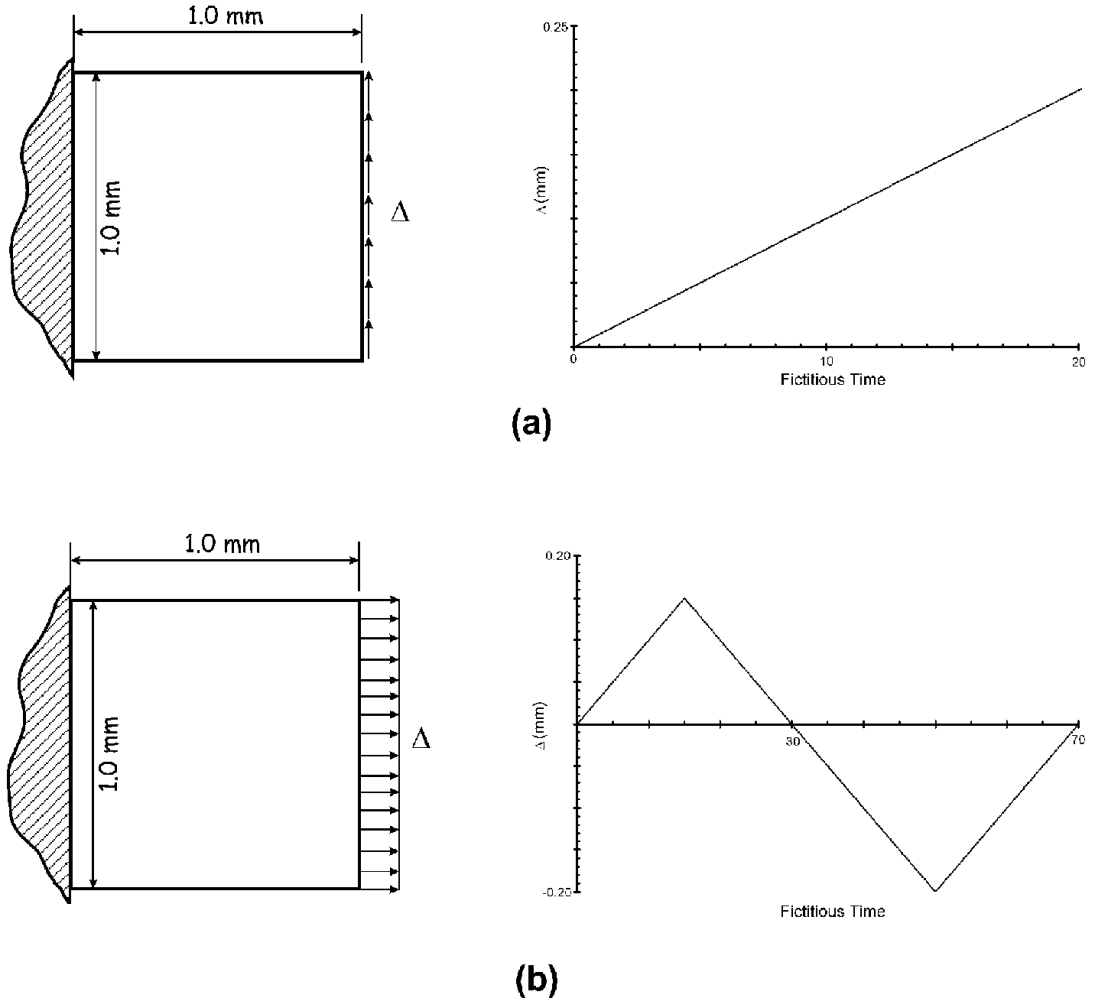

Figure 1.1: Schematic sketch of (a) Problem A, and (b) Problem B, and time histories of the prescribed components of displacement.

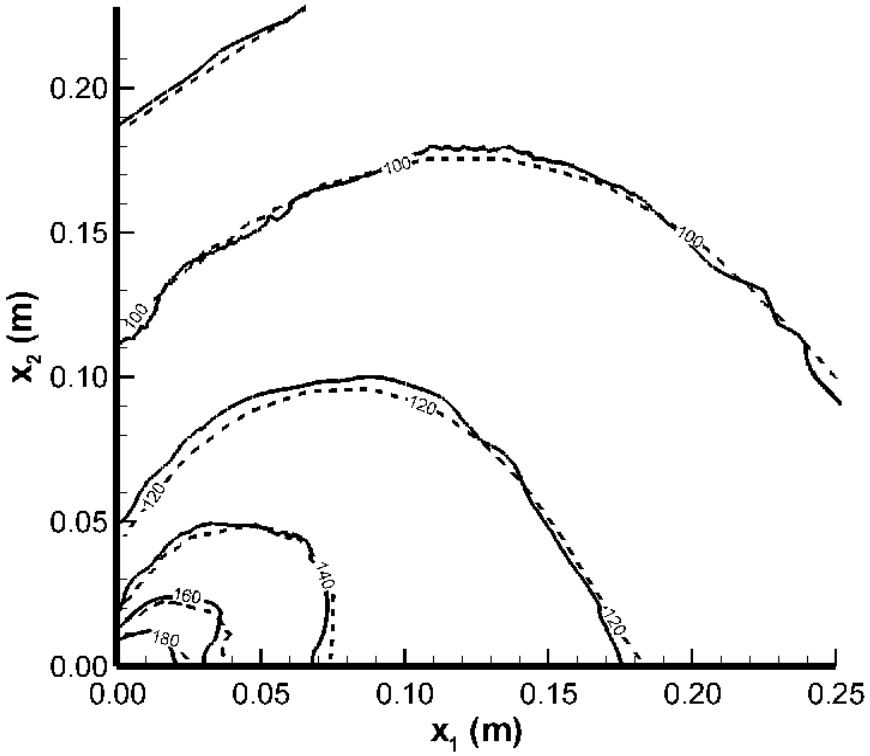
0.20
0.15
0.10
0.05
0.00
x2 (m)
0.00
0.05
0.10
0.15
0.20
0.25
x1 (m)
100
100
100
120
120
120
140
160
180

(a)

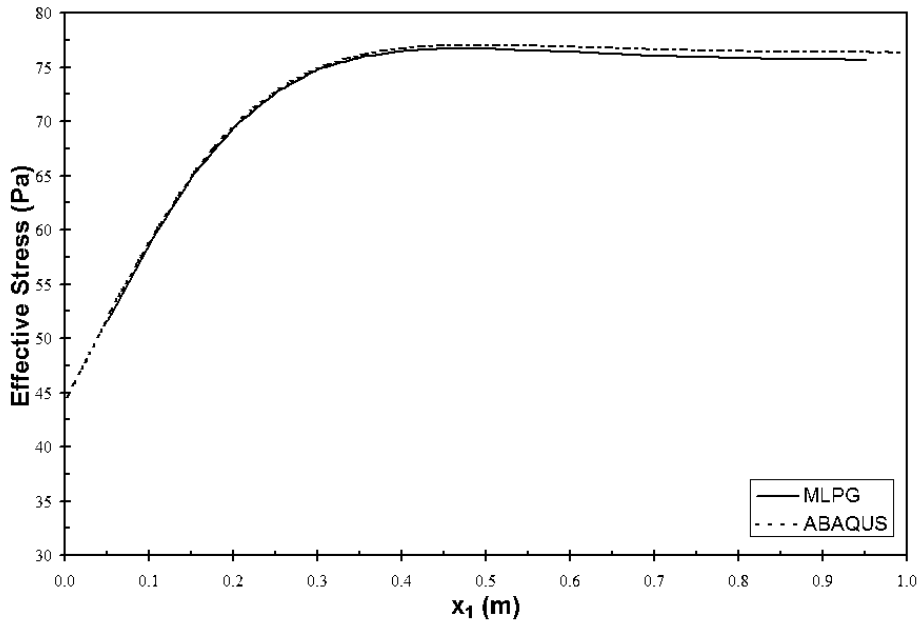
Effective Stress (Pa)
80
75
70
65
60
55
50
45
40
35
30
0.0
0.1
0.2
0.3
0.4
0.5
0.6
0.7
0.8
0.9
1.0
x1 (m)
MLPG
ABAQUS

(b)

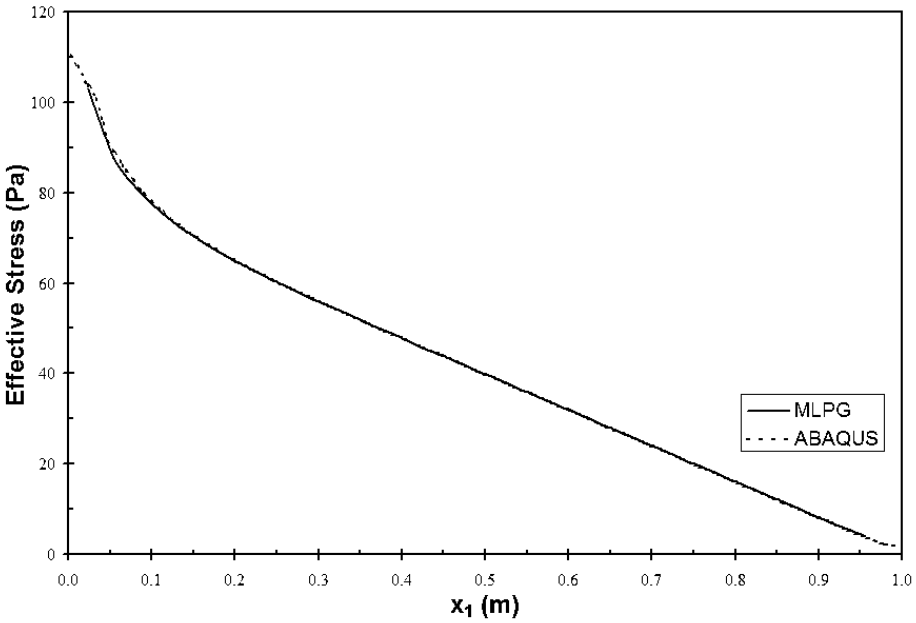

(c)

Figure 1.2: Comparison of the MLPG and the FE results for Problem A; (a) contours of the effective stress, (b) variation of the effective stress at points on the centerline, and (c) variation of the effective stress at points on the bottom edge.

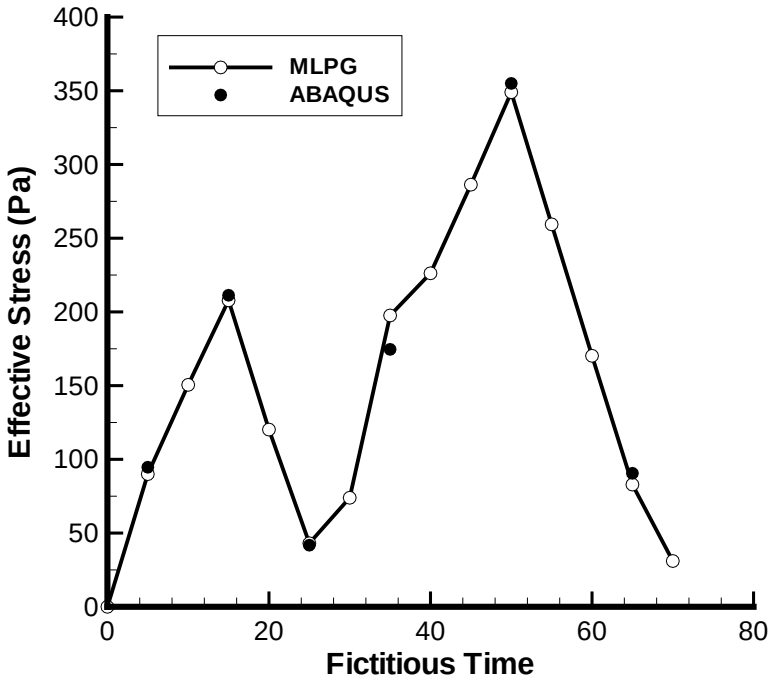
MLPG
ABAQUS
Effective Stress (Pa)
Fictitious Time
0
50
100
150
200
250
300
350
400
0
20
40
60
80

(a)

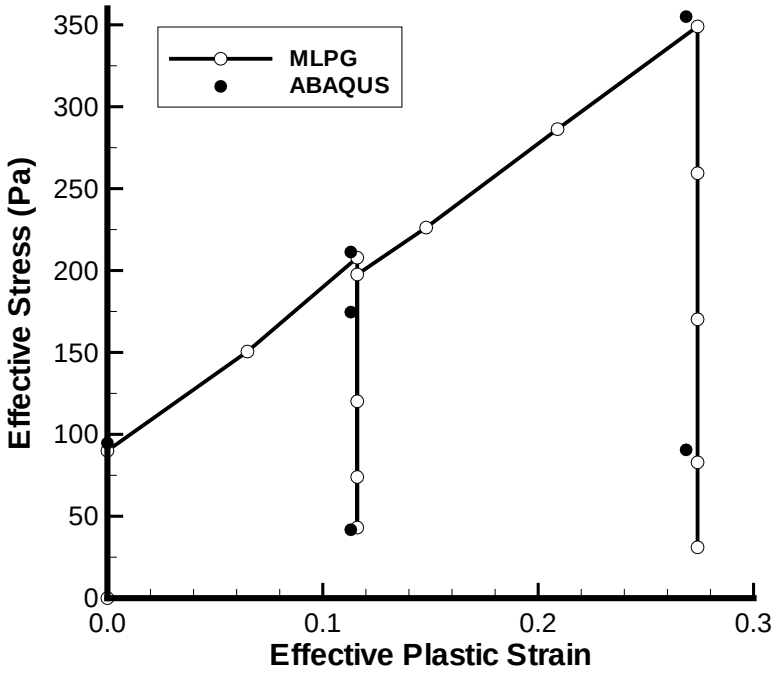
MLPG
ABAQUS
Effective Stress (Pa)
Effective Plastic Strain
0
50
100
150
200
250
300
350
0.0
0.1
0.2
0.3

(b)

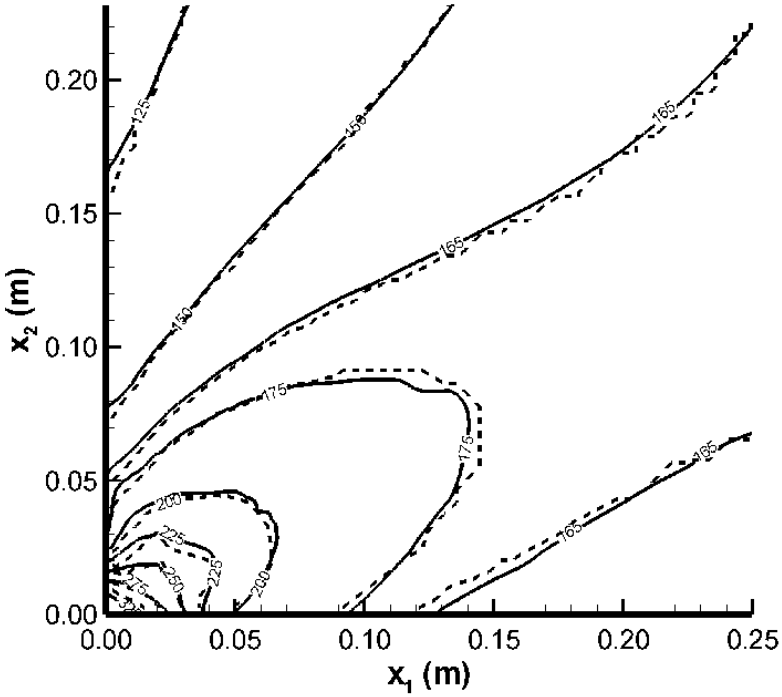

(c)

Figure 1.3: Comparison of the MLPG and the FE results for Problem B;

(a) Time histories of the effective stress and the effective plastic strain at the point $x_1 = x_2 = 0.025$mm.

(b) Effective stress vs. effective plastic strain at the point $x_1 = x_2 = 0.025$mm.

(c) Contours of the effective stress in a small region around the lower left corner.

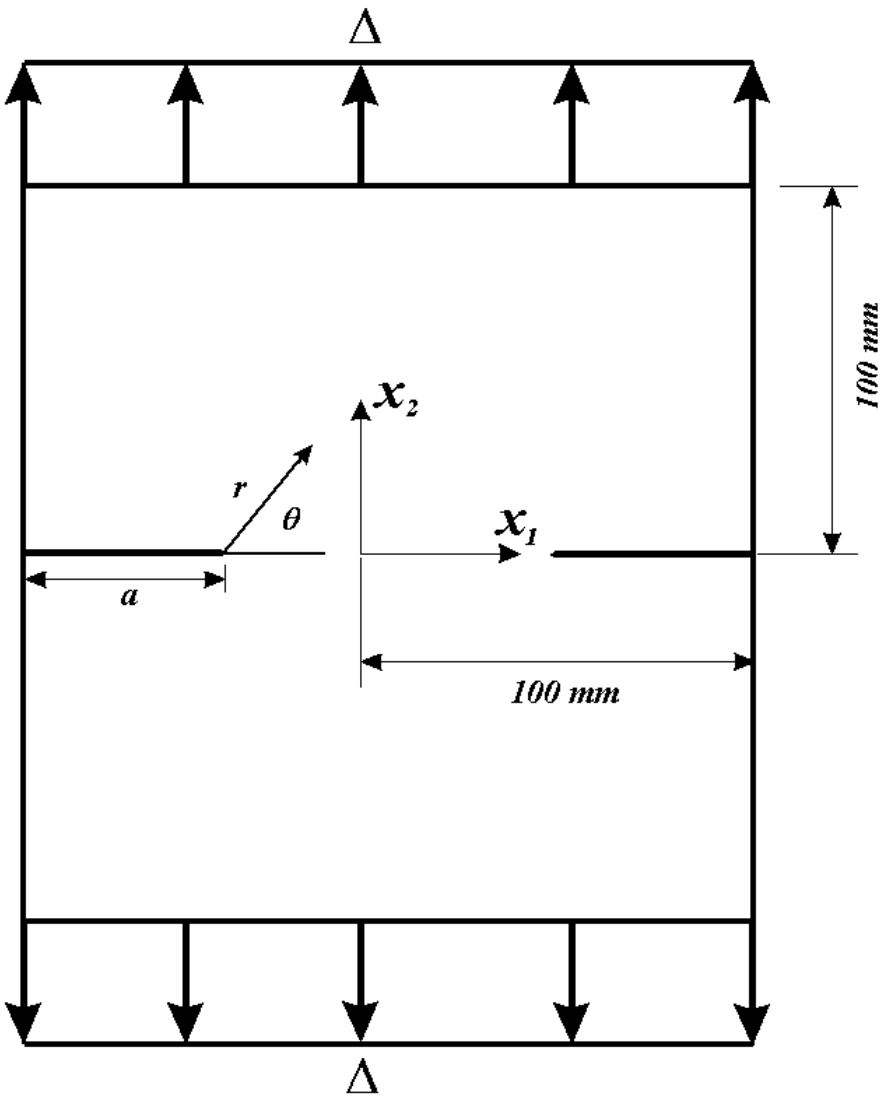

Figure 1.4: Schematic sketch of a double-edge-cracked plate with axial displacements prescribed on the top and the bottom surfaces. Locations of the Cartesian and the cylindrical coordinate axes are also shown.

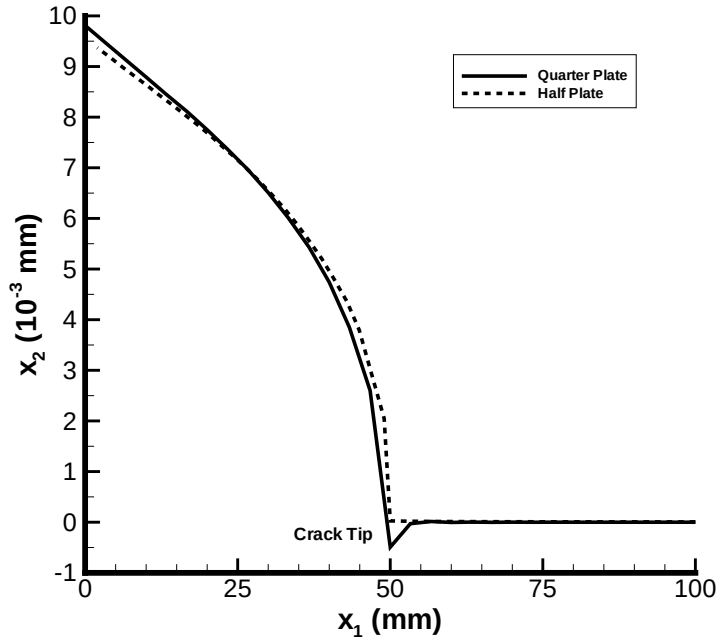

Figure 1.5a: Vertical displacements of points on the crack axis computed when essential boundary conditions are enforced by the penalty method and when deformations of half of the plate are studied.

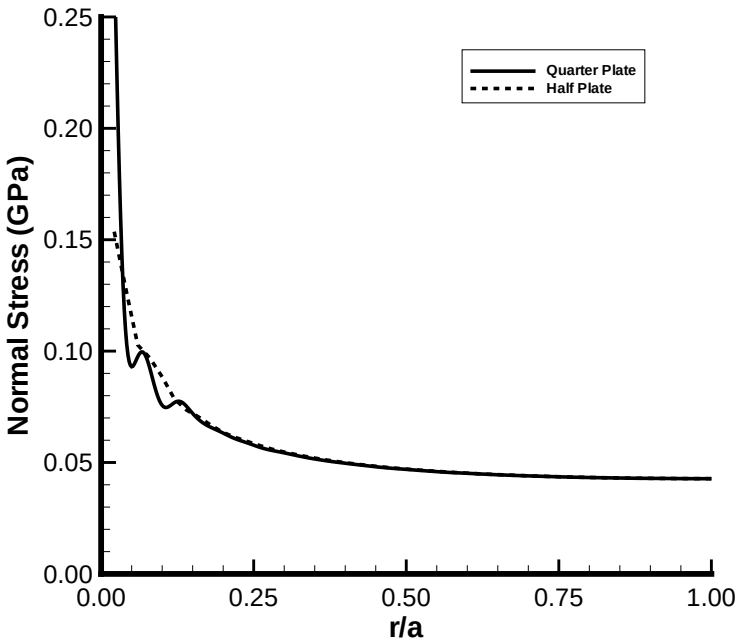

Figure 1.5b: Distribution of the normal stress at points on the crack axis computed with the solutions of the quarter plate and the half plate problems.

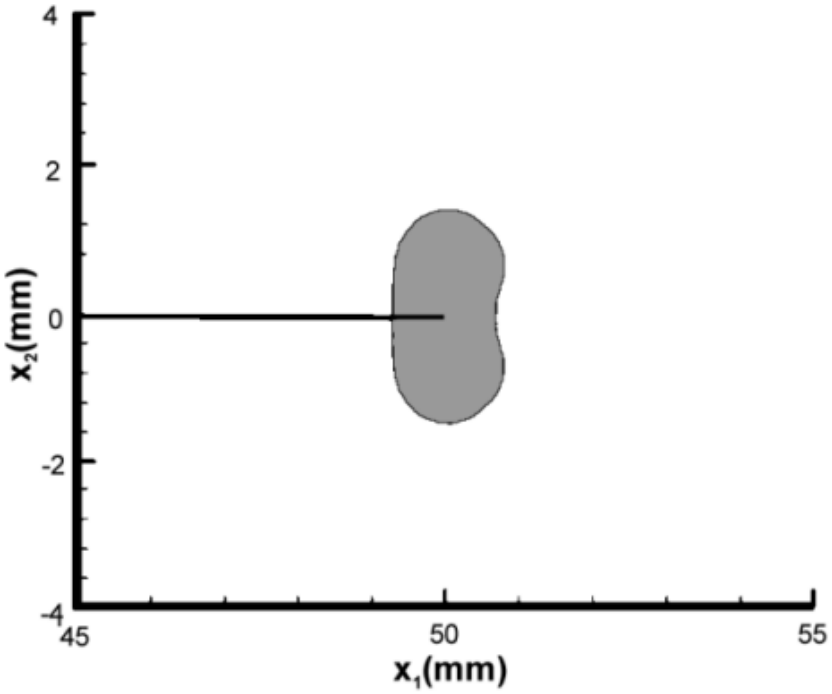

Figure 1.5c: Plastically deformed region around the crack-tip for $\Delta = 0.10$ mm.

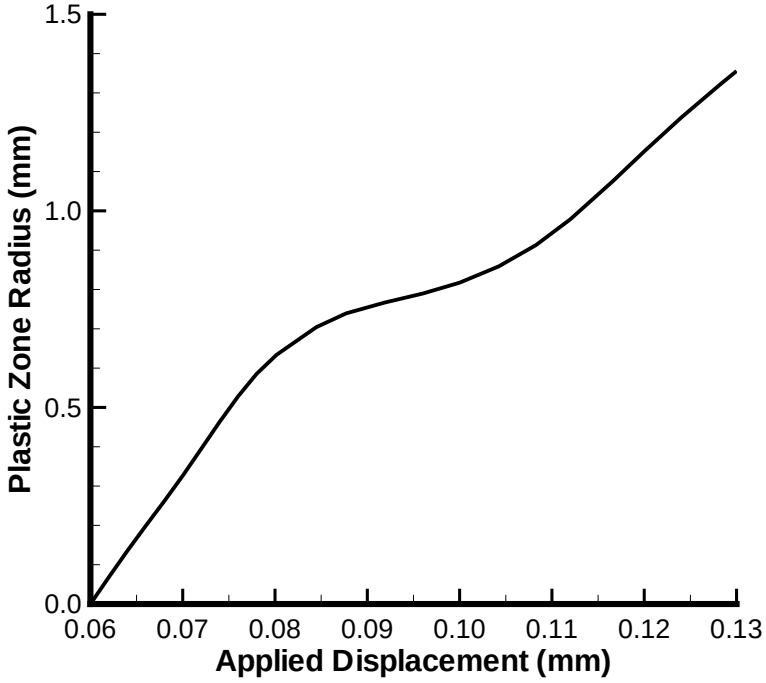

Figure 1.5d: Distance from the crack-tip of the farthest plastically deformed point on the crack axis vs. the axial displacement Δ.

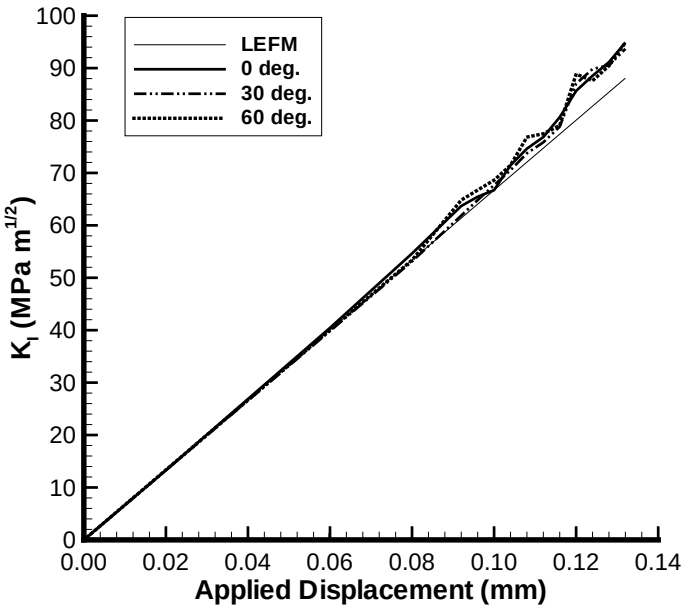

(a)

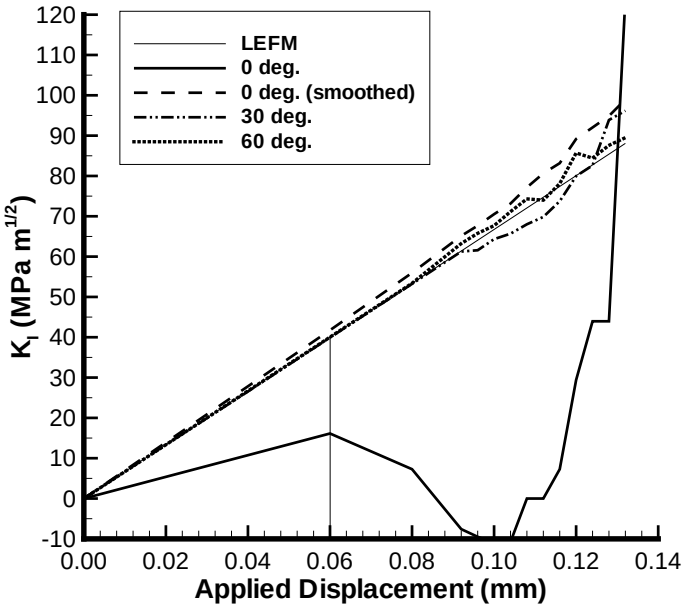

(b)

Figure 1.6: Mode-I stress intensity factor as a function of the applied axial displacement computed by

(a) the plot of log (stress) vs. the log (distance from the crack tip), and

(b) the Dally-Sanford method.

Chapter 2

Adiabatic Shear Banding in Plane Strain Tensile Deformations of Eleven Thermoviscoplastic Materials with Finite Thermal Wave Speed

2.1 Abstract

We study the initiation and propagation of adiabatic shear bands (ASBs) in eleven homogeneous materials each modeled as a microporous, isotropic and thermoviscoplastic, and deformed in plane strain tension. The heat conduction in each material is assumed to be governed by a hyperbolic heat equation; thus thermal and mechanical waves propagate with finite speeds. An ASB is assumed to initiate at a material point when the maximum shear stress there has dropped to 80% of its peak value for that material point and it is deforming plastically. Computed results show that at the time of initiation of an ASB, the axial load required to deform the body drops rapidly. By locating points where the ASB has initiated we find its current length, width, and speed. The eleven materials are ranked according to the time of initiation of an ASB under otherwise identical geometric and loading conditions, and the same initial nonuniform porosity distribution. This ranking of materials is found to differ somewhat from that ascertained by Batra and Kim (1992) who studied their simple shearing deformations, and by Batra, Zhang and Wright (1995) who analyzed torsional

deformations of thin-walled tubular specimens.

2.2 Introduction

Tresca (1878) and Massey(1921) observed hot lines, now called adiabatic shear bands (ASBs), in the form of an X during the hot forging of a rectangular platinum bar. By coating metals with wax and monitoring patterns and the extent of melting, Tresca concluded that at least 70% of the plastic working was converted into heating. Subsequently, Farren and Taylor (1925) and Taylor and Quinney (1937) found that, depending upon the material, this factor equaled 85-95%. Recently, Mason et al. (1994) have asserted that the fraction of plastic working converted into heating depends upon the plastic strain and the plastic strain-rate. Research activity in ASBs picked up since Zener and Hollomon (1944) observed them during the punching of a hole in a steel plate. They stated that a material point becomes unstable when softening of the material caused by its being heated up overcomes its hardening due to strain and strain-rate effects. Heat conduction is a slow process; thus under high rates of deformation there is not enough time for the heat produced at a point to be conducted away. The softened material within the heated zone is deformed even more during further deformations of the body resulting in a catalytic process which eventually ends with deformations of the material becoming unstable. Whereas heat conduction plays a negligible role till the time of initiation of an ASB, its role is significant during the development and propagation of an ASB (e.g. see Batra and Kim (1991), Batra and Chen (2001a)).

Considerè (1885) postulated that, under static deformations, a structure becomes unstable when the load supported by it reaches a maximum value. For simple shearing deformations, it is equivalent to the shear stress attaining a maximum value at the time of instability. Recht (1964) and Clifton (1980) used this criterion to find the nominal strain when a thermoviscoplastic material becomes unstable. Bai (1982) found the instability strain by examining the stability of a homogeneous solution of equations governing the transient simple shearing

deformations of a thermoviscoplastic body. Batra and Chen (2001b) and Wei and Batra (2003) have shown that the Considerè and the Bai criteria give essentially the same value of the instability strain for simple shearing deformations of a thermoviscoplastic body. Lindholm and Johnson (1983) calculated the instability shear strain for 12 materials by using the Considerè criterion and the Johnson-Cook (1983) relation for the dependence of the flow stress upon the plastic strain, the plastic strain-rate and the temperature. Batra, Zhang and Wright (1995) studied 3-dimensional torsional deformations of a thin-walled tube and ranked these 12 materials according to the nominal strain at the time of initiation of a shear band as signified by a sudden drop in the torque required to deform the tube. Batra and Kim (1992) analyzed transient simple shearing deformations of the same 12 materials, introduced an initial geometric defect to make deformations inhomogeneous and proposed that an ASB initiates at a point when the shear stress there has dropped to 80% of its peak value at that point and the material point is deforming plastically. The motivation for this ansatz was the experimental work of Marchand and Duffy (1988) that showed a drop in the torque required to deform a thin walled tube once an ASB had initiated. The ranking of materials according to the nominal shear strain at the initiation of an ASB found by Batra and Kim (1992) matched with that determined by Lindholm and Johnson (1983). Batra and Kim (1992) also computed the band width as a function of the defect size, the localized strain within an ASB, and the temperature rise in the ASB.

Much of the work on ASBs can be found in special issues of the Mechanics of Materials edited by Armstrong et al. (1994), the Applied Mechanics Reviews edited by Zbib et al. (1992), the International Journal of Fracture edited by Batra et al. (2000), and books Material Instability edited by Batra and Zbib (1994), and Localization and Fracture Phenomenon in Inelastic Solids edited by Perzyna (1998). Nearly all works on two and three-dimensional analysis of the ASBs have been numerical. Exceptions include the study on the asymptotic structure of ASBs in antiplane shear deformations by Wright and Walter (1996) and in mode-II deformations by Chen and Batra (1999). They assumed that an ASB propagates

with a uniform velocity and that it can be represented as a singular surface and deformations appear steady to an observer situated on the ASB tip. These are simplifying assumptions as an ASB has a finite width, and the 3-dimensional numerical study of the shear band propagation speed in torsional deformations of a thin-walled tube by Batra and Zhang (1994) had revealed that the shear band speed increased as it propagated along the circumference of the tube. The ASB speed, defined as the speed of propagation of a contour of the effective plastic strain of 1.0, increased with an increase in the nominal strain-rate. Except for the torsional problem, the speed of an ASB depends upon the value of the effective plastic strain at which an ASB is assumed to initiate.

Here we analyze plane strain tensile deformations of a microporous thermoviscoplastic body. Most of the experimental and numerical studies on ASBs have not explicitly defined the criterion employed for the initiation of an ASB. Following Batra and Kim (1992) we assume that an ASB initiates at a point when the maximum shear stress there has dropped to 80% of its peak value and the material point is deforming plastically. The latter condition rules out the initiation of an ASB during elastic unloading. By locating the tip of a propagating ASB as a function of time, we find its width, length, and speed. A distinguishing feature of the present work from earlier 2-dimensional studies is the use of a hyperbolic rather than a parabolic heat equation. Thus, thermal disturbances like mechanical perturbations propagate with a finite speed. Batra and Chen (2001b) concluded that the spacing among adjacent ASBs depends upon the thermal wave speed only when it equals a few m/s; otherwise results are essentially the same as those for the infinite wave speed admitted by a parabolic heat equation. Saad and Cha (1982) found that in heat transfer problems involving very brief time intervals of about 10 μs and/or very high fluxes of the order of $10^5 \mathrm{W/cm}^2$, results obtained from the hyperbolic and the parabolic heat equations are quite different. Chandrasekhariah (1986) has reviewed much of the literature on hyperbolic heat equations. Batra (1975) considered higher-order spatial and temporal derivatives of temperature and found that constitutive relations compatible with the Clausius-Duhem inequality admitted the feasibility of thermal

disturbances propagating with a finite speed; however, for such materials, either a linear problem has a unique solution or thermal waves propagate at a finite speed. Ideally, one will like to have both.

Under identical plane strain loading conditions and initial nonuniform distribution of porosity, we analyze the problem for the 11 materials whose torsional or simple shear deformations were studied by Lindholm and Johnson (1983), Batra and Kim (1992), and Batra, Zhang and Wright (1995). We find the time of initiation of an ASB, its speed of propagation, and rank these materials according to their susceptibility to adiabatic shear banding defined as the average axial strain at the instant of the initiation of an ASB. For two materials we also study the influence on the ASB initiation and propagation of the thermal conductivity, and for one material the effect of the nominal strain-rate. Batra and Jin (1994) studied plane strain tensile deformations of a steel specimen with a Batra-Litonski (e.g. see Batra (1988)) thermoviscoplastic relation and a parabolic heat equation. They showed that the porosity induced softening is more significant than thermal softening.

2.3 Formulation of the Problem

In rectangular Cartesian coordinates and in the absence of body forces and sources of internal energy, equations describing plane strain thermomechanical deformations of a microporous body in the updated Lagrangian description of motion are

$$[\rho(1-f)J]^{\bullet} = 0, \tag{2.1}$$

$$\rho_0(1-f_0)\dot{v}_i = T_{i\alpha,\alpha} \quad i,j = 1,2,\ \alpha = 1,2, \tag{2.2}$$

$$T_{i\alpha}F_{j\alpha} = T_{j\alpha}F_{i\alpha}, \tag{2.3}$$

$$\rho_0(1-f_0)\dot{e} = -Q_{\alpha,\alpha} + T_{i\alpha}\dot{F}_{i\alpha}. \tag{2.4}$$

Here ρ is the present mass density, f the porosity (i.e. the volume fraction of voids), $J = \det \mathbf{F}$, $F_{i\alpha} = \partial x_i/\partial X_\alpha$ the deformation gradient, $\mathbf{x}$ the present position at time t of a material

particle located at the place $\mathbf{X}$ in the reference configuration, $\mathbf{T}$ the first Piola-Kirchhoff stress tensor, e the specific internal energy, $\mathbf{Q}$ the present heat flux measured per unit reference area, $\mathbf{v}$ the velocity of a material particle, a superimposed dot indicates the material time derivative, and a repeated index implies summation over the range of the index. Equations (2.1) through (2.4) express respectively the balance of mass, the balance of linear momentum, the balance of moment of momentum and the balance of internal energy.

We assume that the material is isotropic and the strain-rate tensor $\mathbf{D}$ defined by $D_{ij} = (v_{i,j} + v_{j,i})/2$, $v_{i,j} = \partial v_i/\partial x_j$, has the additive decomposition into an elastic part $\mathbf{D}^e$ and a plastic part $\mathbf{D}^p$, viz.,

$$\mathbf{D} = \mathbf{D}^e + \mathbf{D}^p. \tag{2.5}$$

Equations (2.1)-(2.5) are supplemented with the following constitutive relations.

$$\dot{\sigma}_{ij} + \sigma_{ik}W_{kj} - \sigma_{jk}W_{ik} = \frac{E(1-f)}{1+\nu}D^e_{ij} + \frac{E(1-f)\nu}{(1+\nu)(1-2\nu)}(D^e_{kk} - \alpha\dot{\theta})\delta_{ij}, \tag{2.6}$$

$$\dot{e} = c\tau\ddot{\theta} + c\dot{\theta} + \frac{1}{\rho(1-f)}\sigma_{ij}D^e_{ij}, \tag{2.7}$$

$$T_{i\alpha} = J\sigma_{ij}(F^{-1})_{\alpha j}, \tag{2.8}$$

$$q_i = -\kappa\left(1 - \frac{3}{2}f\right)\theta_{,i},\ Q_\alpha = Jq_i(F^{-1})_{\alpha i}, \tag{2.9}$$

$$\phi \equiv \frac{\sigma_e^2}{\sigma_y^2} - 1 + 2f^*\beta_1\cosh\left(\frac{\beta_2\bar{p}}{2\sigma_y}\right) - \beta_1^2(f^*)^2 = 0,\ \sigma_e^2 = \frac{3}{2}\sigma'_{ij}\sigma'_{ij},\ i,j = 1,2,3, \tag{2.10}$$

$$D^p_{ij} = \dot{\lambda}\frac{\partial\phi}{\partial\sigma_{ij}} = \dot{\lambda}\left[\frac{3\sigma'_{ij}}{\sigma_y^2} - \frac{f^*\beta_1\beta_2}{\sigma_y}\sinh\left(\frac{\beta_2\bar{p}}{2\sigma_y}\right)\delta_{ij}\right],\ \sigma'_{ij} = \sigma_{ij} + p\delta_{ij}, \tag{2.11}$$

$$p = -(\sigma_{11} + \sigma_{22} + \sigma_{33})/3,\ \bar{p} = pH(-p-0), \tag{2.12}$$

$$\dot{\lambda} = \frac{(1-f)\sigma_y\dot{\bar{\varepsilon}}^p_e}{\sigma_{ij}\dfrac{\partial\phi}{\partial\sigma_{ij}}}, \tag{2.13}$$

$$\dot{f} = (1-f)D^p_{ii} + \frac{f_2\dot{\bar{\varepsilon}}^p_e}{s_2\sqrt{2\pi}}e^{-\frac{1}{2}\left(\frac{\bar{\varepsilon}^p_e - \varepsilon_n}{s_2}\right)^2}H(-p-0), \tag{2.14}$$

$$f^* = \begin{cases} f, \ f \le f_c, \\ f_c + \dfrac{f_u - f_c}{f_f - f_c}(f - f_c), \ f > f_c, \end{cases} \tag{2.15}$$

$$\sigma_y = (A + B(\varepsilon_e^p)^n)\left(1 + C\, ln\left(\frac{\dot{\varepsilon}_e^p}{\dot{\varepsilon}_0^p}\right)\right)\left(1 - \left(\frac{\theta - \theta_r}{\theta_m - \theta_r}\right)^m\right). \tag{2.16}$$

The left-hand side of equation (2.6) equals the Jaumann derivative of the Cauchy stress tensor $\boldsymbol{\sigma}$, $W_{ij} = (v_{i,j} - v_{j,i})/2$ is the spin tensor, E Young's modulus, ν Poisson's ratio, α the coefficient of thermal expansion, δ_{ij} the Kronecker delta, c the specific heat, τ the thermal relaxation time, κ the thermal conductivity of the solid material, and θ the present temperature of a material particle. Batra and Jaber (2001) found that the Jaumann and the Green-Naghdi stress rates in equation (2.6) give virtually identical results for a shear band originating from a notch tip in a prenotched plate. $\phi = 0$ describes the yield surface proposed by Gurson (1977) for a porous material, p is the hydrostatic pressure, and f^* the modified value of the porosity given by (2.15). Constants β_1 and β_2, introduced by Tvergaard (1981), provide a better fit of results computed from a finite element analysis of the formation of adiabatic shear bands in a plate having an array of large cylindrical voids with test observations, and $\dot{\lambda}$ is the factor of proportionality defined by (2.13). σ_y is the current yield stress of the material whose dependence upon the effective plastic strain ε_e^p, the effective plastic strain rate $\dot{\varepsilon}_e^p$ and the temperature θ is described by the Johnson-Cook (1983) relation (2.16) in which $A,\ B,\ C,\ \dot{\varepsilon}_0^p$, and m are material parameters, θ_r the room temperature and θ_m the melting temperature of the material. Parameters B and n characterize the strain hardening of the material, C and $\dot{\varepsilon}_0^p$ the strain-rate hardening and the last factor on the right-hand side of (2.16) its thermal softening. Equation (2.14) gives the evolution of the porosity; the first term on its right-hand side is derived by assuming that the matrix is incompressible and the elastic dilatation is negligible as compared to the plastic dilatation, and the second term is the strain based nucleation of voids introduced by Chu and Needleman (1980). f_2, s_2 and ε_n are material parameters; the rate of nucleation of voids is highest when ε_e^p equals ε_n and decays exponentially with the difference between ε_e^p and ε_n.

H is the Heaviside step function. Thus, the second term contributes to the evolution of the porosity at a point only when the hydrostatic pressure there is tensile. To account for the coalescence of neighboring voids, Tvergaard and Needleman (1984) enhanced the porosity, as given by eqn. (2.15), after it reaches its critical value f_c. In eqn. (2.15), f_f is the porosity at ductile fracture, and $f_u = 1/\beta_1$ is the porosity when the yield surface has shrunk to a point. Equations (2.10) and (2.16) imply that the radius of the von Mises yield surface increases due to strain- and strain-rate hardening of the material but decreases due to the softening induced by the temperature rise and the increase in porosity. The degradation of material properties due to the damage, taken here synonymous with the porosity, is indicated by equations (2.6) through (2.10). The affine variation with the porosity of Young's and the bulk moduli implies that the rule of mixture has been employed to find the effective moduli. The interaction, if any, among neighboring voids has been tacitly ignored. The shrinkage of the yield surface due to an increase in porosity described by equation (2.10) can be appreciated by plotting the yield surface for two different values of f while keeping other variables fixed. Perzyna (1998) has given a different equation for the evolution of porosity.

Initial and boundary conditions needed to complete the formulation of the problem are:

$$\begin{aligned} &\mathbf{x}(\mathbf{X},0) = \mathbf{X},\ \mathbf{v}(\mathbf{x},0) = \mathbf{0},\ \theta(\mathbf{X},0) = \theta_0,\ \dot{\theta}(\mathbf{X},0) = 0,\ \rho(\mathbf{X},0) = \rho_0, \\ &\dot{\varepsilon}_e^p(\mathbf{X},0) = 0,\ f(\mathbf{X},0) = f_0(\mathbf{X}), \\ &T_{i\alpha}N_\alpha = 0 \text{ on } \Gamma_t,\ x_i = \bar{x}_i \text{ on } \Gamma_v,\ Q_\alpha N_\alpha = 0 \text{ on } \partial\Omega. \end{aligned} \tag{2.17}$$

That is, the initial velocity and the initial rate of change of temperature are null, the initial temperature is uniform θ_0, and the initial mass density is uniform ρ_0. The part Γ_t of the boundary $\partial\Omega$ of the region Ω occupied by the body in the reference configuration is traction free and positions of material particles on Γ_v are given as a function of time. The entire boundary $\partial\Omega$ is thermally insulated at all times.

Substitution from equations (2.5), (2.7) and (2.9) into (2.4) gives the following hyperbolic

heat equation:

$$\rho_0(1-f_0)c(\tau\ddot{\theta}+\dot{\theta}) = \left(\kappa\left(1-\frac{3}{2}f\right)\theta_{,\alpha}\right)_{,\alpha} + J\sigma_{ij}D^p_{ij}. \tag{2.18}$$

The term $\sigma_{ij}D^p_{ij}$ equals the heating due to plastic working; thus the Taylor-Quinney parameter has been set equal to 1. Except for a delay in the time of initiation of an ASB, other results remain unaffected by a lower value of the Taylor-Quinney factor. The form (2.18) of the hyperbolic heat equation is due to Cattaneo (1958) and Vernotte (1958). The thermal relaxation time τ in it represents the time required to establish a steady state of heat conduction in an element suddenly exposed to a heat flux. According to Chester (1963) τ equals $3\kappa/\rho c V_0^2$ where V_0 is the speed of an elastic wave. Thus for a typical steel, $\tau = 1\times 10^{-12}$s, and $\tau \simeq 25\times 10^{-12}$s for copper. Here we will conduct a parametric study for different values of τ.

Let ρ_0, $\dot{\varepsilon}_R$, H, σ_0 and θ_R be the reference mass density, the reference strain-rate, the reference length, the reference stress and the reference temperature used to non-dimensionalize quantities. Then in terms of nondimensional variables indicated by the same symbols as before, equations (2.2) and (2.18) become

$$\alpha_I(1-f_0)\dot{v}_i = T_{i\alpha,\alpha}, \quad i=1,2,\ \alpha=1,2, \tag{2.19}$$

$$\rho_0(1-f_0)(\tau\ddot{\theta}+\dot{\theta}) = -\alpha_t\left(\left(1-\frac{3}{2}f\right)\theta_{,\alpha}\right)_{,\alpha} + J\sigma_{ij}D^p_{ij},\ i,j=1,2,3. \tag{2.20}$$

where

$$\alpha_I = \frac{\rho_0\dot{\varepsilon}_R^2H^2}{\sigma_0},\ \alpha_t = \frac{\kappa}{\rho_0 cH^2\dot{\varepsilon}_R},\ \theta_R = \frac{\sigma_0}{\rho_0 cH^2\dot{\varepsilon}_R}\ . \tag{2.21}$$

α_I and α_t are nondimensional measures of inertia and heat conduction effects. Thus, for a given material, inertia effects are directly proportional to the square of the reference strain-rate and the square of the reference length, say the specimen height, and heat conduction effects are inversely proportional to the reference strain-rate and the square of the specimen height. This nondimensionalization of variables is the same as that employed by Batra and Kim (1992). In terms of the prescribed axial velocity v_0 on the top surface, $\alpha_I = \rho_0 v_0^2/\sigma_R$, $\alpha_t = \kappa/\rho cHv_0$. Thus depending upon whether the nominal strain-rate or the prescribed

axial velocity on the top surface is controlled, the specimen height does or does not affect the value of α_I. However, the specimen height affects α_t in both cases. Batra and Chen (2001a) found that with the nominal shear strain-rate kept fixed, the shear band width equaled 5.8 and 8.32 μm for $H = 2.5$ and 25 mm respectively and the body deformed in simple shear. Henceforth we set $\dot{\varepsilon}_R$ = steady value of the average axial strain-rate in the specimen; thus the nondimensional time $\bar{t}(= t\dot{\varepsilon}_R)$ equals the average axial strain.

We note that Batra and Kim (1990), Batra and Jaber (2001) and Batra and Chen (2001a) have analyzed different aspects of shear banding with four different thermoviscoplastic relations, namely, the Johnson-Cook (1983), the Litonski-Batra (e.g. see Batra (1988)), the Bodner-Partom (1975) and a power law. These relations were calibrated to give nearly the same effective stress vs. the effective strain curve during homogeneous deformations of the body. However, during inhomogeneous deformations, each one of the relations gave qualitatively similar but quantitatively different results. The decision to use the Johnson-Cook relation here is based on the availability of values of thermomechanical parameters for the eleven materials.

2.4 Weak Formulation of the Problem

Equations (2.6), (2.8) and (2.3) imply that the balance of moment of momentum (2.3) is identically satisfied. The present mass density can be computed from equation (2.1) if the deformation gradient and the current value of the porosity are known. Thus, the dependent variables to be solved for are $\mathbf{x}$, f and θ and the independent variables are $\mathbf{X}$ and t. Equations (2.19) and (2.20) are second-order coupled non-linear hyperbolic partial differential equations for $\mathbf{x}$ and θ. These equations can not be written explicitly in terms of $\mathbf{x}$ and θ since $\mathbf{T}$ is given by (2.8) and σ by (2.6) which involves $\mathbf{D}^p$ and θ. In order to solve the problem numerically by the finite element method, we first derive its weak formulation.

Let $\mathbf{w}(\mathbf{X})$ be a smooth function that vanishes on Γ_v. We take the inner product of eqn.

(2.19) with $\mathbf{w}$, integrate the resulting eqn. over the region Ω occupied by the body in the reference configuration, and use the divergence theorem and the natural boundary condition $(2.17)_8$ on Γ_t to arrive at

$$\int_\Omega \alpha_I(1-f_0)\dot{v}_i w_i d\Omega = -\int_\Omega w_{i,\alpha} T_{i\alpha} d\Omega + \int_{\Gamma_t} w_i \bar{t}_i d\Gamma. \tag{2.22}$$

Let $\psi_1, \psi_2, \ldots, \psi_n$ be finite element basis functions defined on Ω. We write

$$\begin{aligned} v_i &= \sum_{A=1}^{\text{nodes}} \psi_A(\mathbf{X})\tilde{v}_{Ai}(t),\ i=1,2, \\ w_i &= \sum_{A=1}^{\text{nodes}} \psi_A(\mathbf{X}) c_{Ai},\ i=1,2. \end{aligned} \tag{2.23}$$

Here $\tilde{\mathbf{v}}$ is the vector of velocities of nodes, and $\mathbf{c}$'s are constants. Substituting from (2.23) into (2.22) and exploiting the fact that the resulting eqn. must hold for all choices of $\mathbf{c}$'s we get

$$\begin{aligned} \mathbf{M}\dot{\tilde{\mathbf{v}}} &= \mathbf{F}^{\text{ext}} - \mathbf{F}^{\text{int}}, \\ M_{AB} &= \int_\Omega \alpha_I(1-f_0)\psi_A\psi_B d\Omega, \\ F^{\text{int}}_{Ai} &= \int_\Omega \psi_{A,\alpha} T_{i\alpha} d\Omega, \\ F^{\text{ext}}_{Ai} &= \int_{\Gamma_t} \psi_A \bar{t}_i d\Gamma. \end{aligned} \tag{2.24}$$

In order to derive a weak form of eqn. (2.20) we first introduce an auxiliary variable defined by

$$\xi = \dot{\theta} \tag{2.25}$$

and follow the same procedure as that used to derive eqn. $(2.24)_1$ with the following result.

$$\begin{aligned} \dot{\tilde{\boldsymbol{\theta}}} &= \tilde{\boldsymbol{\xi}}, \\ \tau\mathbf{H}\dot{\tilde{\boldsymbol{\xi}}} + \mathbf{H}\tilde{\boldsymbol{\xi}} &= \mathbf{F}^\theta + \bar{\mathbf{Q}}, \end{aligned} \tag{2.26}$$

where

$$\begin{aligned} H_{AB} &= \int_\Omega \rho_0(1-f_0)\psi_A\psi_B d\Omega, \\ F^\theta_A &= \int_\Omega \alpha_t \left(1-\frac{3}{2}f\right)\theta_{,\alpha}\psi_{A,\alpha} d\Omega, \\ Q_A &= \int_\Omega \psi_A J\ \text{tr}(\boldsymbol{\sigma}\mathbf{D}^p) d\Omega. \end{aligned} \tag{2.27}$$

Note that the natural boundary condition of zero heat flux has been embedded in eqn. $(2.26)_2$.

We solve eqn. (2.16) for $\dot{\varepsilon}_e^p$ in terms of σ_y, ε_e^p and θ and derive its weak form in the same way as before except that the divergence theorem is not used. Recall that $\dot{\varepsilon}_e^p > 0$ only when a material point is deforming plastically as signified by the satisfaction of eqn. $(2.10)_1$; otherwise $\dot{\varepsilon}_e^p = 0$. Weak forms of eqns. (2.6) and (2.14) are also derived. At each node we thus have the following 10 unknowns: two components of velocity $\mathbf{v}$, auxiliary variable ξ, temperature θ, porosity f, effective plastic strain ε_e^p, and four components σ_{11}, σ_{22}, σ_{12} and σ_{33} of the Cauchy stress tensor $\boldsymbol{\sigma}$. These are computed by simultaneously integrating with respect to time t equations $(2.24)_1$, $(2.26)_1$, $(2.26)_2$ and those obtained from (2.16), (2.6) and (2.14). Batra and Jin (1994), and Batra and Jaber (2001) also employed a similar approach except that they used a parabolic heat equation and did not have to introduce the auxiliary variable ξ.

2.5 Computation and Discussion of Results

A finite element (FE) computer code employing 4-node isoparametric quadrilateral elements and 2×2 integration rule has been developed to find an approximate solution of the above formulated initial-boundary-value problem. The coupled ordinary differential equations resulting from the semidiscrete formulation of the problem are integrated with the subroutine LSODE (Livermore Solver for Ordinary Differential Equations). It adjusts the time step adaptively to compute the solution within the prescribed absolute and relative tolerances; each tolerance was set equal to 10^{-5}. It has been found that the time step chosen by LSODE decreases rapidly when the deformation begins to localize at one or more points in the body as indicated by the drop in the maximum shear stress at these points while they are deforming plastically.

The plane strain thermomechanical problem analyzed here is similar to that studied by

Batra and Jin (1994) and Batra and Jaber (2001) with the following two exceptions: We employ a hyperbolic heat equation instead of a parabolic one, and we use 4-node quadrilateral elements and they employed 3-node constant strain triangular elements. Batra and Jin (1994) adaptively refined the spatial mesh in which the size of an element generated was inversely proportional to the effective strain-rate (or any other scalar measure of deformation) at the element centroid. Batra and Jaber (2001) integrated eqns. (2.6), (2.14) and (2.16) at the centroid of each triangular element which reduces the number of unknowns. Both in their and in the present work, coordinates of nodes are updated after every increment of time.

The developed code was validated by solving several simple problems with $\tau = 0$ and comparing the computed solution with that found from the earlier code of Batra and Jin (1994). For $\tau > 0$, a heat conduction problem was solved for a nonporous rigid body and the computed speed of the thermal wave was found to match well with the analytical value. Finally, for $\tau = 0$, a shear band problem analyzed previously by Batra and Jin (1994) was solved with the present code; the two sets of computed results were found to match well.

We have studied the initiation and propagation of ASBs in eleven homogeneous and isotropic materials; values of thermomechanical parameters for these materials are listed in Table 2.3. We have also listed in the Table computed values of α_I and α_t for a prismatic specimen of square cross-section of each side 10 mm and deformed at an axial nominal strain-rate of 5,000/s. When computing α_I and α_t, we set $\sigma_0 = A$; however, other choices of the reference stress are possible (i.e., 0.2% offset) and will change values of α_I and α_t. As signified by the values of α_I and α_t, inertia effects are most predominant for copper and brass; heat conduction is most noticeable for copper and 7039 aluminum. Unless otherwise stated, the specimen size and the nominal strain-rate are kept fixed. A schematic sketch of the problem analyzed and the time history of the axial velocity v_2 prescribed on the top and the bottom surfaces are shown in Fig. 2.1. The rise time of 1 μs for the applied axial velocity to reach its steady value is typical of the experimental observations. Because of the symmetry of the geometry, the initial conditions and the boundary conditions about the horizontal and the

vertical centroidal axes, deformations of the material in the first quadrant are analyzed. This region is divided into 3600 uniform 4-node square elements in the reference configuration, and a 2×2 integration rule is used to evaluate various integrals appearing in the weak formulation of the problem. All bounding surfaces are taken to be thermally insulated and free of tangential tractions. Null normal velocities arising out of the problem symmetry are applied on surfaces DA and DC (cf. Fig. 2.1) a time dependent normal axial velocity is prescribed on CB, and null normal tractions are specified on AB. Initial conditions used are listed in (2.17).

A finer mesh could not be used because of the limited storage available and also to have a reasonable CPU time. Results computed with a coarser mesh agreed qualitatively with those obtained with the mesh of 3600 elements. An adaptively refined mesh will give a better value of the band width.

For the homogeneous body with uniform initial conditions, deformations will become inhomogeneous because of the interaction with the incident waves of waves reflected from the boundaries and corners. This may happen at different instants in the eleven materials because of the differences in their material properties. In order to ensure some kind of uniformity, an initial defect in the form of a nonuniformly distributed initial porosity given by

$$f_0(\mathbf{X}, 0) = f_{ce} \left(1 - \left(\frac{X_\alpha X_\alpha}{H^2} \right) \right)^9 e^{-5(X_\alpha X_\alpha / H^2)} \tag{2.28}$$

is introduced. Here f_{ce} is the initial porosity at the specimen centroid and may be thought of as representing the strength of the defect.

Values assigned to different parameters are listed below.

$$\begin{aligned} &\beta_1 = 1.5,\ \beta_2 = 1.0,\ f_2 = 0.04,\ s_2 = 0.1,\ \sigma_0 = A,\ \theta_r = 273K, \\ &\varepsilon_n = 0.5,\ f_c = 0.15,\ f_u = 2/3,\ f_f = 0.25,\ f_{ce} = 0.025 \text{ or } 0.05. \end{aligned} \tag{2.29}$$

In the following discussion, initial porosity distributions with $f_{ce} = 0.025$ and 0.05 are referred to as weak and strong defects respectively. Results for one material are computed for several

values of the thermal relaxation time, τ, to delineate the effect of the thermal wave speed on the initiation of an adiabatic shear band (ASB). Otherwise, τ is set equal to $10^{-8}s$.

We follow Batra and Kim's (1992) criterion and assume that an ASB initiates at a point when

$$\tau_{\max} = 0.8\tau_{\text{peak}} \text{ and } \dot{\varepsilon}_e^p > 0 \tag{2.30}$$

where $\tau_{\max}$ is the maximum shear stress at that point, and τ_{peak} is the peak value of $\tau_{\max}$ reached at that point. The accompanying condition, $\dot{\varepsilon}_e^p > 0$, ensures that the drop in the maximum shear stress is due to softening of the material and not due to elastic unloading. The necessity of the requirement $\dot{\varepsilon}_e^p > 0$ is illustrated by the plots in Fig. 2.2 of the time histories of $\tau_{\max}$ and ε_e^p at two material points in the 4340 steel specimen - one within (point W) an ASB and the other outside (point P) of an ASB. Even though $\tau_{\max}$ has dropped to 80% of its maximum value at each point, the effective plastic strain stops growing at point P but its rate of increase picks up at point W when $\tau_{\max}$ begins to decrease at each point. The rapid increase in $\dot{\varepsilon}_e^p$ signifies the onset of the localization of deformation at point W and $\dot{\varepsilon}_e^p = 0$ for elastic unloading at P. As mentioned in the introduction, the criterion (2.30) is motivated by experimental observations of Marchand and Duffy (1988) which indicated that the torque required to deform a thin-walled tube drops when an ASB initiates. Thus an ASB initiates at the point W at $\bar{t} = 0.325$. Batra and Rattazzi (1997) used the following four definitions for the initiation of an ASB at the root of a V-notch in a thick-wall steel tube: (i) the effective stress has dropped to 90% of its maximum value and the material point is deforming plastically, (ii) the effective stress has dropped to 80% of its maximum value and the material point is deforming plastically, (iii) the effective plastic strain equals 0.5, and (iv) the effective plastic strain equals 1.0. Each one of the four definitions gave a different value of the time of initiation and the speed of propagation of an ASB. Thus results herein depend upon the criterion (2.30) of the initiation of an ASB.

The velocity distribution in the deformed shape of the specimen at $\bar{t} = 0.35$ is exhibited

in Fig. 2.3. It is clear that the specimen has necked near the center where the defect is strongest. The specimen can be divided into three regions: one adjoining the top right edge moves upwards with the axial velocity varying from zero at the bottom left corner to essentially uniform and equal to the prescribed velocity a small distance from it, another near the bottom right corner moves to the left with horizontal velocity changing from zero at the bottom left corner to nearly uniform a small distance from it, and the shear banded material within the preceding two regions in which the velocity distribution across the shear banded region changes sharply through 90°. Recalling that the bottom left corner is stationary, the velocity distribution can not be uniform in the three regions. The region containing the bottom right corner decelerates. Since the normal velocity across the shear band must be continuous, the tangential velocity undergoes a jump to accommodate the sharp rotation of velocity vectors. Batra and Jin (1994) and Batra and Ko (1992, 1993) computed similar transitions in the velocity field across an ASB. This confirms Tresca's (1878) assertion that the tangential velocity is discontinuous across an ASB. None of the analytical studies on ASBs have modeled this discontinuity in the tangential velocity across an ASB.

Contours of the effective plastic strain at $\bar{t} = 0.35$ plotted in Fig. 2.4 evince that the deformation has localized into a narrow region inclined at an angle of approximately 45° with the horizontal axis; and that the effective plastic strain in this region exceeds 1.0. In the full cross-section, this region of localized deformation will look like an X observed by Tresca (1878) in compressed specimens. Batra and Ko (1992, 1993) simulated the compression of rectangular and cylindrical specimens. In the former case, the region of localized deformation had the shape of an X and in the latter case specimens barreled either outwards or inwards depending upon whether the top and the bottom surfaces contacting the loading device had infinite or no friction.

2.5.1 Effect of Thermal Wave Speed

For the 4340 steel and the weak defect, results have been computed for the thermal relaxation time $\tau = 0,\ 10^{-8},\ 10^{-7},\ 10^{-6},\ 10^{-5}$ and 10^{-4}s; corresponding speeds of a thermal wave equal ∞, 31.88, 10.08, 3.19, 1.01 and 0.32 m/s respectively. Note that the thermal wave speed is inversely proportional to $\sqrt{\tau}$. For several values of time, $\bar{t}$, the criterion (2.30) for the initiation of an ASB was applied at the centroid of every element in the problem domain; thus enabling us to determine when and where the ASB initiated. The time history of the length of the ASB so ascertained for the six values of τ and the weak initial defect is plotted in Fig. 2.5. The slopes of these curves equal the ASB speed. The ASB length has been non-dimensionalized by H that is one-half of the specimen height or 5 mm. The final ASB speed is computed at the instant when the porosity at the centroid of the specimen equals $0.8f_f$ or 0.2. The three curves for $\tau = 0$, 10^{-8} and 10^{-7}s are very close to each other signifying that for $\tau \leq 10^{-7}$s, the ASB initiation time and speed are virtually unaffected by the value of τ. However, as the thermal relaxation time is increased which results in lower speeds of thermal waves, the initiation of the ASB is delayed and its propagation speed is lowered; the initial and the final ASB speeds are listed in Table 2.1. This may be illustrated by setting $\alpha_t = 0$ in equation (2.20) which then becomes analogous to the equation of motion of a unit mass attached to a damper of viscosity $1/\tau$. With an increase in τ for this system, it takes a little longer for the temperature to reach its final value at a point. It is clear that for $\tau \leq 10^{-6}$s, the final ASB speed is nearly 2.3 times its initial speed. For torsional deformations of a thin-walled steel tube deformed at an average shear strain-rate of 5,000/s, Batra and Zhang (1994) found that the ASB increased from 180 m/s at the time of initiation of an ASB to 1,130 m/s when the ASB reached the diametrically opposite point. They took $\tau = \kappa = 0$, so there was neither heat conduction nor a thermal wave.

Table 2.1. For the 4340 steel and the weak defect, the initial and the final speeds of propagation of an ASB as a function of the thermal relaxation time.

Thermal relaxation time (s)	0	10^{-8}	10^{-7}	10^{-6}	10^{-5}	10^{-4}
Thermal wave speed (m/s)	∞	31.88	10.08	3.19	1.01	0.32
Avg. axial strain when ASB initiates	0.314	0.315	0.315	0.320	0.343	0.378
Initial speed of an ASB (m/s)	144	135	144	145	147	133
Final speed of an ASB (m/s)	318	318	318	347	299	336

Marchand and Duffy (1988) computed the shear band speed from their test observations to be 250 m/s in a high strength steel. Zhou et al.'s (1996a) test results indicated that the ASB speed increased with time to a maximum of around 1 km/s in a HY-100 steel. Batra and Rattazzi (1998) found that the computed speed strongly depends upon the thermal softening characteristics of the material. They analyzed the propagation of an ASB during torsional deformations of a thick-walled tube with a circumferential v-notch. They found that the affine thermal softening in the Johnson-Cook relation gave an ASB speed of about 250 m/s and the power law thermal softening in the thermoviscoplastic relation used by Zhou et al. (1996b) gave an ASB speed of about 1 km/s. The Johnson-Cook relation is based on torsional tests conducted at moderate strain rates and temperatures; its validity for strains, strain-rates and temperatures occurring in an ASB has not been established since there is very little test data at these deformation levels. One reason for not achieving a steady speed of ASBs during our computations is that the ASB has to travel a small distance before the effect of free boundaries becomes significant. After the ASB has reached nearly half way between the centroid and the free right surface, deformations at points on the free boundary where the ASB will intersect it begin to localize and an ASB starts to propagate inwards from there. For example, the width of the specimen in the necked region in Fig. 2.4 is 3.5 mm and the maximum distance an ASB can traverse is about 5.3 mm.

Figure 2.6 exhibits time histories of the evolution of the maximum shear stress at the centroid of the cross-section. The curves are qualitatively similar for each one of the six values of τ. When the state of deformation at the centroid satisfies the ASB initiation criterion (2.30), the maximum shear stress there begins to collapse. The rate of collapse of the maximum shear stress is virtually unaffected by the drop in the value of τ from 10^{-7} to zero.

2.5.2 Ranking of the Eleven Materials According to the ASB Initiation Time

For each one of the eleven materials studied, computed time histories of the length of an ASB with $\tau = 10^{-8}$s and for the weak and the strong defects are exhibited in Fig. 2.7a,b. It is clear that the strength of the defect does not alter the ordering of materials according to the time of initiation of an ASB; however, the time history of the evolution of its length and hence the speed of propagation are noticeably influenced by the defect size. For doubling of the defect strength, the average axial strain at the time of initiation of an ASB drops to about 2/3 of its value for the weak defect for each one of the eleven materials. For Depleted Uranium, Tungsten and S-7 tool steel, the final ASB speed is considerably higher than the initial ASB speed. For the weak defect the homologous temperature, defined as the ratio of the current temperature to the melting temperature of the materials, varies from a low of 0.03 for Armco iron to 0.24 for 2024 Aluminum. It depends upon the yield stress of the material, the strain at the instant of the initiation of an ASB, and the heat capacity of the material. For the weak defect, the ratio of the average axial strain at the instant of the initiation of an ASB to that when the maximum shear stress peaks has the lowest value of 1.32 for the cartridge brass and the highest value of 5.7 for the tungsten. The ratio of the corresponding values of the effective plastic strain for the two materials equals 1.43 and 14.8 respectively. The stress triaxiality ratio, defined as $\sigma_{kk}/3\sigma_{22}$, at the specimen centroid has the lowest value of 1.06 for 7039 Aluminum and Armco iron and the highest value of 1.43 for depleted Uranium. Vandergiessen et al. (1995) have suggested that higher values of the triaxiality factor enhance the nucleation of voids. Here the stress-controlled nucleation of

voids has not been considered. However, the triaxiality influences the development of the yield surface and the evolution of plastic strain-rates through equations (2.10) and (2.11). Batra and Ravisankar (2000) studied the initiation and propagation of an ASB from a notch tip in an impact loaded prenotched nonporous plate and found that $\sigma_{ii} < 0$ within an ASB.

We have listed in Table 2.4 the ranking of the eleven materials according to the times of initiation of an ASB and also the computed initial and the final speeds of propagation of the ASB. Note that the nondimensional time equals the average axial strain. From values of α_I and α_t listed in Table 2.3, it is clear that they do not correlate at all with the average strain when an ASB initiates. One reason is that α_I and α_t do not reflect the strain- and the strain-rate hardening and the thermal softening characteristics of the material. In Table 2.4 we have also listed the axial instability strain, ε_i, determined from the Considerè condition $d\sigma_y/d\varepsilon_e^p = \sigma_y$. Assuming that $d\dot{\varepsilon}_e^p/d\varepsilon_e^p = 0$, $\dot{\epsilon}_e^p = 5000/\text{s}$, elastic deformations and the heat conduction effects are negligible, $\tau = 0$, $d\theta = \sigma_y d\varepsilon_e^p/\rho c$, and the specimen is deformed in simple tension, ε_i is given by

$$\frac{nB\varepsilon_i^{n-1}}{A + B\varepsilon_i^n} - \frac{(A + B\varepsilon_i^n)(1 + C\, ln(\dot{\varepsilon}_i/\dot{\varepsilon}_0))}{\theta_m \rho c} = 1. \tag{2.31}$$

Note that we have studied plane strain transient deformations, and σ_{11}, σ_{12} and σ_{33} do not vanish as they do in the tension test. Thus the average axial strain predicted by the Considerè condition need not equal that when the maximum shear stress attains its peak value. The reduction in the area of cross-section is included in the derivation of eqn. (2.31) and is also considered in the plane strain deformations of the specimen. It is clear from values listed in Table 2.4 that the effective strain predicted from the Considerè condition (2.31) differs significantly from the effective plastic strain at the time of initiation of an ASB. Furthermore, the Consideré criterion does not accurately predict the ordering of materials according to when an ASB will initiate in them under otherwise identical conditions. Batra et al. (1995) numerically studied torsional deformations of a thin-wall tube made of each one of these eleven materials. The prescribed tangential velocity at the end faces of the tube

produced an average shear strain-rate of 5000/s. When ranked according to the average shear strain at the time of initiation of an ASB, the order determined by Batra et al. (1995) is: Tungsten, S-7 tool steel, Depleted Uranium, 2024-T351 aluminum, 7039-aluminum, 4340 steel, Armco iron, Carpenter Electric iron, 1006 steel, Cartridge brass, and OFHC Copper. It differs from that presently found suggesting that the ranking depends upon the type of test and/or the state of stress. The time histories of the evolution of the maximum shear stress, the effective plastic strain, the porosity and the temperature at the centroid of the cross-section are plotted in Fig. 2.8a-d. Oscillations in the maximum shear stress vs. the nondimensional time curves are due to the interaction among the incident and the reflected waves. These oscillations are predominant in materials having a large value of α_I such as the cartridge brass, copper, the carpenter electric iron, Armco iron and 1006 steel. The value of A in equation (2.16) is low for these materials; thus, plastic deformations ensue virtually instantaneously upon the arrival at the centroid of the initial tensile loading wave. This results in a sharp increase in the effective plastic strain and the porosity till the strain hardening effects and the compressive wave reflected from the top surface neutralize the effect of the initial tensile loading wave. Subsequent growth rate of f, ε_e^p and θ is consistent with that for the other six materials. The time of initiation of an ASB could also be identified as the instant when $\dot{\varepsilon}_e^p$ suddenly increases but this criterion is difficult to use in a computer code. Test observations on materials deformed under shock loading have revealed that a material point fails when the porosity there equals 0.25. With this failure criterion, depleted uranium, tungsten heavy alloy and S-7 tool steel will fail in plane strain tensile deformations at a nominal axial strain of about 0.14. The carpenter electric iron and the Armco iron will fail at an average axial strain of 0.45 which is higher than that for copper; these values depend upon the assumed initial porosity distribution. Due to a lack of the test data, values of f_2, s_2 and ε_n in equation (2.14) giving the evolution of porosity have been taken to be the same for the eleven materials. Thus the computed failure strains should not be expected to match very well with experimental findings. Since ε_e^p has exceeded ε_n for each one of the

eleven materials studied, therefore, significant nucleation of new voids has occurred. The nondimensional temperature in Fig. 2.8d is the homologous temperature. These plots reveal that the maximum value of the homologous temperature is 0.4; thus thermal softening has not been very significant.

In order to vividly illustrate the differences among the strains predicted by the Considerè condition, when the maximum shear stress peaks and when an ASB initiates, we have plotted in Fig. 2.9 the axial load vs. the non-dimensional time for the 4340 steel, 7039 aluminum and OFHC copper. It is clear that in the 4340 steel and 7039 aluminum, the load begins to drop severely at the instant of the initiation of the ASB; however, for copper the drop in the axial load subsequent to the initiation of the ASB is negligible. For each one of the three materials, the axial strain predicted by the Considerè condition is considerably smaller than that when the maximum shear stress peaks even though the decrease in the cross-sectional area during loading has been accounted for in the Considerè condition.

2.5.3 Effect of Thermal Conductivity

Batra and Kim (1991) have analyzed the effect of thermal conductivity κ on the initiation and development of an ASB in a thermoviscoplastic material deformed in simple shear. They found that it virtually has no effect on the initiation of an ASB but strongly influences the development of the ASB. Batra and Chen (2001a) found that during the final stage of the development of an ASB in a 4340 steel, 85% of the heat produced due to plastic working is conducted out of the ASB edges. Here we examine the effect of thermal conductivity in a two-dimensional problem on the initiation and propagation of an ASB in copper and 4340 steel. For each material the problem was analyzed again by setting $\kappa = 0$. As is evident from the plots in Fig. 2.10 of the ASB length vs. time, the initiation and the speed of propagation of an ASB in the 4340 steel for both $\kappa = 0$ and $\kappa > 0$ are essentially the same. However, in copper, the initiation of the ASB is enhanced by about 4% with $\kappa = 0$, and the initial and the final propagation speeds increase by 1.4% and 6.5% respectively. The two time

histories of the maximum shear stress shown in Fig. 2.11 reveal that the thermal conductivity significantly affects the rate of collapse of the shear stress after the band has initiated and hence its formation/development; similar results were obtained by Batra and Kim (1991) for simple shearing deformations with the Bodner-Partom (1975) thermoviscoplastic relation.

2.5.4 Effect of Nominal Strain-Rate

For the 4340 steel, the weak defect and for four values of the average axial strain-rate, Fig. 2.12a,b exhibits time histories of the evolution of the maximum shear stress at the centroid of the cross-section and of the ASB length. The nominal strain-rate was varied by changing the steady value of the axial velocity applied on the top and the bottom surfaces. The rise time t_r (cf. Fig. 2.1) was increased from 1 μs to 5 μs in order to successfully compute results for the highest axial strain-rate considered; $t_r = 5$ μs was used for each of the four cases. As expected, the initiation of an ASB is significantly delayed with an increase in the axial strain-rate; a similar result for the simple shear problem was obtained by Batra (1988). The drop in the maximum shear stress is less precipitous at the axial strain-rate of 40,000/s as compared to that at the axial strain-rate of 2000/s. Also, the initial shear band speed drops with an increase in the axial strain-rate, but the final ASB speed is essentially independent of the applied axial strain-rate. The computed shear band speeds for the four axial strain-rates are listed in Table 2.2. For the torsional deformations of a thin-wall tube, Batra and Zhang (1994) found that the initial speed of an ASB increased from 250 m/s at a nominal shear strain-rate of 5,000/s to 1,000 m/s when the nominal shear strain-rate equaled 25,000/s. In the torsional problem, the shear band propagates along the circumference of the tube that is also the direction of loading; its propagation is not restrained by the deformed material surrounding the ASB tip. However, in the plane strain compression problem, the ASB propagates along a direction that makes an angle of about 45° with the loading axis.

Table 2.2. The ASB initiation times, and initial and final speeds of the ASB for four values of the average axial strain-rate.

Avg. axial strain-rate (1/s)	Nondimensional ASB initiation time	Initial ASB speed (m/s)	Final ASB speed (m/s)
2,000	0.300	245	243
5,000	0.327	214	252
20,000	0.534	136	276
40,000	0.676	50	246

2.5.5 Variation of Effective Plastic Strain Along and Effective Plastic Strain Across an ASB

Figure 2.13a depicts, at three different instants of time during the development, the distribution of the effective plastic strain along an ASB in the 4340 steel. The tip of the ASB, marked with a vertical line, moves at an average speed of approximately 300 m/s. At the tip of the band the effective plastic strain-rate has the maximum value of 10^5/s and the effective plastic strain has the minimum value. As the band develops, the effective plastic strain-rate ahead of the band becomes uniform and nearly equals that at the ASB tip. During the early stage of the development of an ASB, the gradient of the effective plastic strain along the band is lower ahead of the band tip than that behind it. We have plotted in Fig. 2.13b the distribution of the effective plastic strain across an ASB in the 4340 steel. It is evident that the peak strain in the band equals 1.5, and its width varies from 125 μm to 500 μm depending upon whether it is defined as the thickness of the region with an effective plastic strain exceeding 1.4 or 0.5.

2.6 Conclusions

We have analyzed the problem of the initiation and propagation of an ASB in plane strain coupled thermomechanical deformations of a microporous, isotropic and homogeneous thermoviscoplastic material with a hyperbolic heat equation. The nominal strain at which an ASB initiates and its speed of propagation have been ascertained for eleven materials, namely,

depleted uranium, tungsten, S-7 tool steel, 4340 steel, 7039 aluminum, 2024 aluminum, 1006 steel, OFHC copper, cartridge brass, carpenter electric iron and armco iron. These materials are listed in the order of their decreasing susceptibility to adiabatic shear banding. This ranking is unaffected by the defect size. The same defect, in terms of a nonuniform distribution of initial porosity, was introduced in each of the eleven materials. For the 4340 steel, a parametric study has been conducted for seven values of the thermal wave speed. The initiation time of an ASB is noticeably affected by the thermal wave speed only when it drops down from infinity to a few m/s. For the 4340 steel and the OFHC copper, results have been computed with and without the effects of heat conduction. It is found that the assumption of locally adiabatic deformations does not influence the initiation time and the speed of an ASB in the 4340 steel; however, it does so in the copper. During the development of the ASB in copper, the rate of drop of the maximum shear stress is much higher for locally adiabatic deformations as compared to that when heat conduction is considered. Batra and Chen (2001a) found that during the late stages of the development of an ASB, nearly 85% of the heat produced due to plastic working is conducted out of the edges of the band. Thus heat conduction influences the band width and the time elapsed between the initiation and the full development of the band. The initial speed of propagation of an ASB is found to decrease and its time of initiation increase with an increase in the nominal axial strain-rate. During torsional deformations of a thin-wall tube, Batra and Zhang (1994) found that the ASB speed increased with an increase in the nominal strain-rate.

2.7 References

Armstrong R., Batra R. C., Meyers M., Wright T. W., (Eds.), Shear Instabilities and Viscoplasticity Theories, a special vol. of the *Mechs. of Materials*, **17**, 83-328 (1994)

Bai Y. L., Thermoplastic Instability in Simple Shear, *J. Mech. Phys. Solids*, **30**, 195-207 (1982)

Batra R. C., Chen L., Effect of Viscoplastic Relations on the Instability Strain, Shear Band Initiation Strain, the Strain Corresponding to the Maximum Shear Band Spacing, and the Band Width in a Thermoviscoplastic Material, *Int. J. Plasticity*, **17**, 1465-1489 (2001a)

Batra R. C., Chen L., Instability Analysis and Shear Band Spacing in Gradient-dependent Thermoviscoplastic Materials with Finite Speeds of Thermal Waves, *Archives of Mechanics*, **53**, 167-192 (2001b)

Batra R. C., Jaber N. A., Failure Mode Transition in an Impact Loaded Prenotched Plate with Four Thermoviscoplastic Relations, *Int. J. Fracture*, **110**, 47-71 (2001)

Batra R. C., Rattazzi D., Adiabatic Shear Banding in a Thick-walled Steel Tube, *Comp. Mechs.*, **5**, 426-442 (1997)

Batra R. C., Zhang X., Wright T. W., Critical Strain Ranking of 12 Materials in Deformations Involving Adiabatic Shear Bands, *J. Appl. Mechs.*, **652**, 252-255 (1995)

Batra R. C., Jin X. S., Analysis of Dynamic Shear Bands in Porous Thermally Softening Viscoplastic Materials, *Arch. Mech.*, **46**, 13-36 (1994)

Batra R. C., Zbib H. M., Material Instabilities: Theory and Applications, ASME Press (1994)

Batra R.C., Zhang X., On the Propagation of a Shear Band in a Steel Tube, *J. Engng. Mat. Tech.*, **116**, 155-161 (1994)

Batra R. C., Ko K. I., Analysis of Shear Bands in Dynamic Axisymmetric Compression of a Thermoviscoplastic Cylinder, *Int. J. Engng. Sci.*, **31**, 529-547 (1993)

Batra R. C., Kim C. H., Analysis of Shear Banding in Twelve Materials, *Int. J. Plasticity*, **8**, 425-452 (1992)

Batra, R. C., Ko, K.I., An Adaptive Mesh Refinement Technique for the Analysis of Shear Bands in Plane Strain Compression of a Thermoviscoplastic Solid, *Computational Mechanics*, **10**, 369-379, 1992.

Batra R. C., Kim C. H., Effect of Thermal Conductivity on the Initiation and Growth of Adiabatic Shear Bands in Steels, *Int. J. Engr. Sci.*, **29**, 949-960 (1991)

Batra R.C., Kim K. H., Effect of Viscoplastic Flow Rules on the Initiation and Growth of Shear Bands at High Strain Rates, *J. Mechs. Phys. Solids*, **38**, 859-874 (1990)

Batra R.C., Rajapakse Y.D.S., Rosakis A., Failure Mode Transitions under Dynamic Loading, a special volume of the *Int. J. of Fracture*, **101**, 1-180 (2000)

Batra R. C., Steady State Penetration of Thermoviscoplastic Targets, *Comp. Mech.*, **3**, 1-12 (1988)

Batra R. C., On Heat Conduction and Wave Propagation in Non-simple Rigid Solids, *Letters in Appl. and Engng. Sci.*, **3**, 997-107 (1975)

Bodner S. R., Partom Y., Constitutive Equations for Elastic-viscoplastic Strain-hardening Materials, *J. Appl. Mech.*, **56**, 385-389 (1975)

Cattaneo C., A Form of Heat Equation which Eliminates the Paradox of Instantaneous Propagation, *CR Acad. Sci.*, **247**, 431-433 (1958)

Chester M., Second Sound in Solids, *Phys. Rev.*, **131**, 2103-2015 (1963)

Chandrasekharaih D. S., Thermoelasticity with Second Sound: A Review, *Appl. Mech. Rev.*, **39**, 355-376 (1986)

Chen L., Batra R. C., The Asymptotic Structure of a Shear Band in Mode-II Deformations, *Int. J. Engng. Sci.*, **37**, 895-919 (1999)

Chu C., Needleman A., Void Nucleation Effects in Biaxially Stretched Sheets, *J. Engr. Mat. Tech.*, **102**, 249-256 (1980)

Clifton R. J., Adiabatic Shear in Material Response to Ultrahigh Loading Rates. NRC National Material Advisory Board (U.S.) Report NMAB-36 (Ed. W. Herrmann et al.), Washington, DC (1980)

Considerè A. G., Memiore sur L'emploi du fer et de L'acier dans les Constructions, *Annals des Ponts et Chaussees*, **9**, 574-775 (1885)

Farren W. S., Taylor G. I., The Heat Developed During Plastic Extrusion of Metal, *Proc. Royal Soc.*, **A107** (1925)

Gurson A. L., Continuum Theory of Ductile Rupture by Void Nucleation and Growth: Part I, *J. of Engr. Mater. and Tech.*, **99**, 2-15 (1977)

Johnson G. R., Cook W. H., A Constitutive Model and Data for Metals Subjected to Large Strains, High Strain-Rates, and High Temperatures, *Proc. 7th International Symp. on Ballistics*, 541-547 (1983)

Lindholm U. S., Johnson G. R., Material Behavior Under High Stress and Ultrahigh Loading Rates, *Sagamore Army Mater. Research Conf.*, **29**, 61-79 (1983)

Marchand A., Duffy J., An Experimental Study of the Formation Process of Adiabatic Shear Bands in a Structural Steel, *J. Mech. Phy. Solids*, **36**, 251-283 (1988)

Mason J. J., Rosakis A. J., Ravichandran G., On the Strain and Strain Rate Dependence of the Fraction of Plastic Work Converted to Heat: An Experimental Study using High Speed Infrared Detectors and Kolsky Bar, *Mechs. Materials*, **17**, 135-146 (1994)

Massey H. F., The Flow of Metal During Forging, *Proc. Manchester Assoc. of Engineers*,

21-26 (1928)

Perzyna P., Constitutive Modeling of Dissipative Solids for Localization and Fracture [In:] *Localization and Fracture Phenomenon in Inelastic Solids*, P. Perzyna [Ed.], 99-242, Springer, Berlin (1998)

Perzyna P. (Ed.) Localization and Fracture Phenomenon in Inelastic Solids, Springer-Verlag, Wien, New York (1998)

Recht R. F., Catastrophic Thermoplastic Shear, *J. Appl. Mech.*, **31**, 189-193 (1964)

Saad M. H., Cha C. Y., Axisymmetric non-Fourier Temperature in Cylindrically Bounded Domains, *Int. J. Nonlinear Mechanics*, **17**, 129-136 (1982)

Taylor G. I., Quinney H., The Latent Energy Remaining in a Metal After Cold Working, *Proc. Royal Soc.*, **A143**, 307-326 (1934)

Tresca H., On Further Application of the Flow of Solids, *Proc. Inst. Mech. Engrs.*, **30**, 301-345 (1978)

Tvergaard V., Influence of Voids on Shear Band Instabilities Under Plane Strain Conditions, *Int. J. Fracture*, **17**, 389-407 (1981)

Tvergaard V., Needleman A., Analysis of the cup-cone fracture in a round tensile bar, *Acta Metallurgica*, **32**, 157-169 (1984)

Vandergiessen E., Vanderburg M.W.D., Needleman A., Tvergaard V., Void growth due to creep and grain-boundary diffusion at high triaxialities, *Journal of the Mechanics and Physics of Solids*, **43**, 123-165 (1995)

Vernotte P., The True Heat Equation, *CR Acad. Sci.*, **247**, 2103 (1958)

Wei, Z., Batra, R.C., Dependance of Instability Strain Upon Damage in Thermoviscoplastic Materials, *Archives of Mechanics* (in press)

Wright T. W., Walter J. W., The Asymptotic Structure of an Adiabatic Shear Band in

Antiplane Motion, *J. Mechs. Phys. Solids*, **44**, 77-97 (1996)

Zbib, H. M., Shawki T., Batra R.C., [Eds.], Material Instabilities, special issue of *Appl. Mech. Rev.*, **45**, 1-173 (1992)

Zener C., Hollomon J. H., Effect of Strain Rate Upon Plastic Flow of Steel, *J. Applied Phys.*, **15**, 22-32 (1944)

Zhou M., Ravichandran G., Rosakis A., Dynamically Propagating Shear Bands in Impact-Loaded Prenotched Plates–II, *J. Mech. Phys. Solids*, **44**, 1007-1032 (1996)

Table 2.3 Values of Thermomechanical Parameters for the 11 Materials Studied

Material	A (MPa)	B (MPa)	C	m	n	θ_m (K)	α (10^{-6}/K)	κ (W/mK)	c (J/kgK)	ρ (kg/m^3)	ν	E (GPa)	α_I^* (10^{-3})	α_t^* (10^{-6})
1006 steel	350.25	275.0	0.022	1.00	0.36	1811	12.6	73	452	7890	0.27	207	14.08	163.8
4340 steel	792.19	509.51	0.014	1.03	0.26	1793	12.3	38	477	7840	0.27	210	6.19	81.3
S-7 tool steel	1538.89	476.42	0.012	1.00	0.18	1763	12.3	40	477	7750	0.27	220	3.15	86.56
2024 aluminum	264.75	426.09	0.015	1.00	0.34	775	23.0	119	875	2770	0.33	74	6.54	392.8
7039 aluminum	336.46	342.66	0.010	1.00	0.41	877	23.0	149	875	2770	0.33	69	5.15	491.8
Armco iron	175.12	379.99	0.060	0.55	0.32	1811	12.1	73	452	7890	0.29	196	28.16	163.8
Carpenter Electric iron	289.58	338.53	0.055	0.55	0.40	1811	12.1	73	452	7890	0.23	148	17.03	163.8
Cartridge Brass	111.69	504.69	0.009	1.68	0.42	1189	21.1	111	385	8520	0.34	100	47.68	270.7
OFHC Copper	89.63	261.64	0.031	1.09	0.31	1356	17.0	386	383	8960	0.33	120	62.48	899.9
Depleted Uranium	1079.01	1119.69	0.007	1.00	0.25	1473	19.0	28	117	18600	0.22	190	10.77	102.9
Tungsten	1505.79	176.50	0.016	1.00	0.12	1723	4.3	75	134	17000	0.20	406	7.06	263.4

*Values for an average axial strain rate of 5,000/s, $H = 5\text{mm}$, and $\sigma_0 = A$.

Table 2.4 For the eleven materials, values of the nominal axial strain, the effective plastic strain, and the homologous temperature when the maximum shear stress peaks and when an ASB initiates. Values of the triaxiality ratio at the specimen centroid and the speed of an ASB are also listed.

Material	Effective strain from Considerè's condition	Weak Defect									Strong Defect		
		$\tau_{\max}$ has peak value			When ASB initiates				ASB speed m/s		Axial Strain when ASB initiates	ASB speed m/s	
		Axial strain	Effective plastic strain	Homologous temperature	Axial strain	Effective plastic strain	Homologous temperature	Triaxiality ratio	Initial	Final		Initial	Final
Depleted Uranium	0.0498	0.038	0.0527	0.0216	0.124	0.4091	0.1598	1.430	124	496	0.072	193	334
Tungsten	0.045	0.024	0.0283	0.0123	0.137	0.4180	0.1757	1.255	140	648	0.086	165	357
S-7 tool steel	0.0173	0.044	0.0567	0.0169	0.168	0.5468	0.1627	1.147	157	517	0.114	247	357
4340 steel	0.0491	0.141	0.1980	0.0337	0.315	0.6794	0.1201	1.069	158	214	0.203	239	399
7039 aluminum	0.0818	0.207	0.2750	0.0821	0.330	0.6860	0.2127	1.056	235	244	0.233	265	355
2024 aluminum	0.1013	0.218	0.2810	0.0958	0.350	0.6806	0.2433	1.071	183	184	0.251	265	418
1006 steel	0.0782	0.183	0.2660	0.0204	0.374	0.6406	0.0525	1.117	98	42	0.260	198	46
OFHC copper	0.1810	0.262	0.3612	0.0198	0.391	0.5886	0.0351	1.081	107	45	0.270	206	26
Cartridge brass	0.2649	0.310	0.4187	0.0476	0.409	0.5951	0.0742	1.108	102	52	0.276	207	82
Carpenter electric iron	0.1194	0.181	0.2566	0.0138	0.427	0.6208	0.0359	1.093	105	22	0.280	199	92
Armco iron	0.1579	0.222	0.2998	0.0134	0.433	0.6099	0.0295	1.061	189	79	0.290	198	76

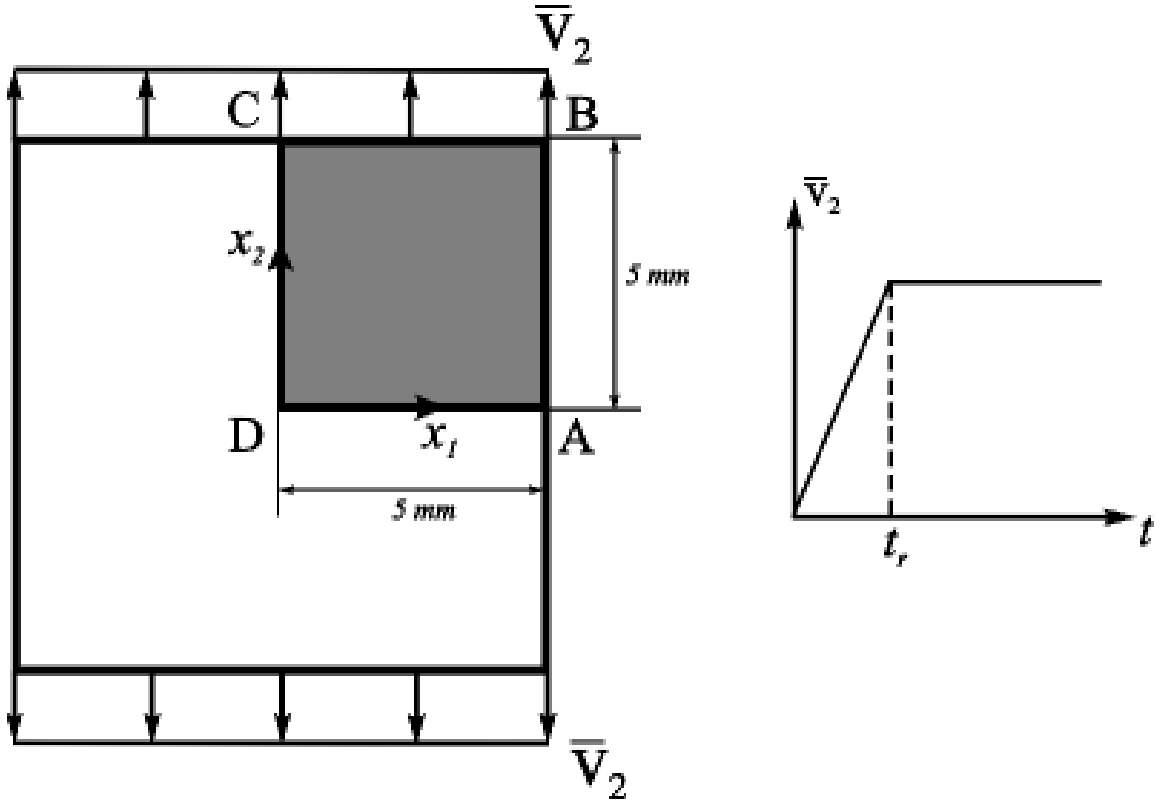

Figure 2.1. Schematic sketch of the problem studied, and the time history of the applied axial velocity.

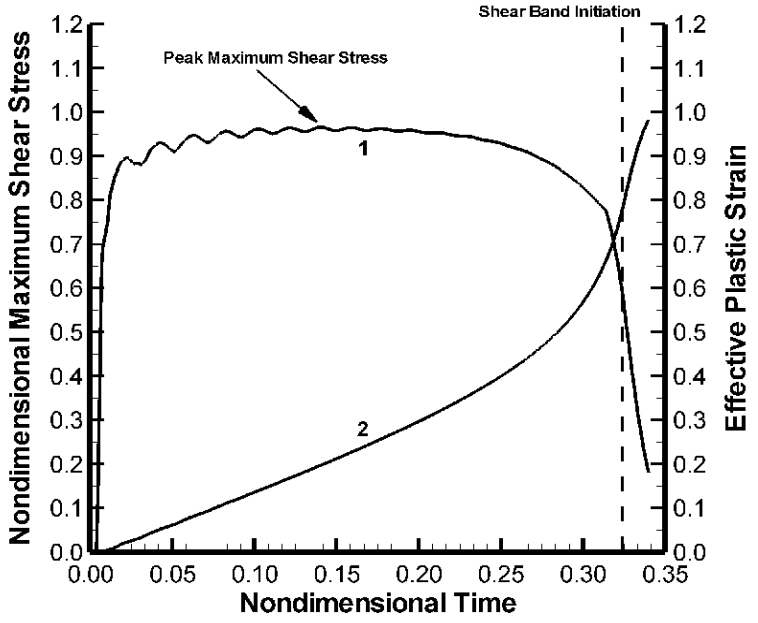

(a)

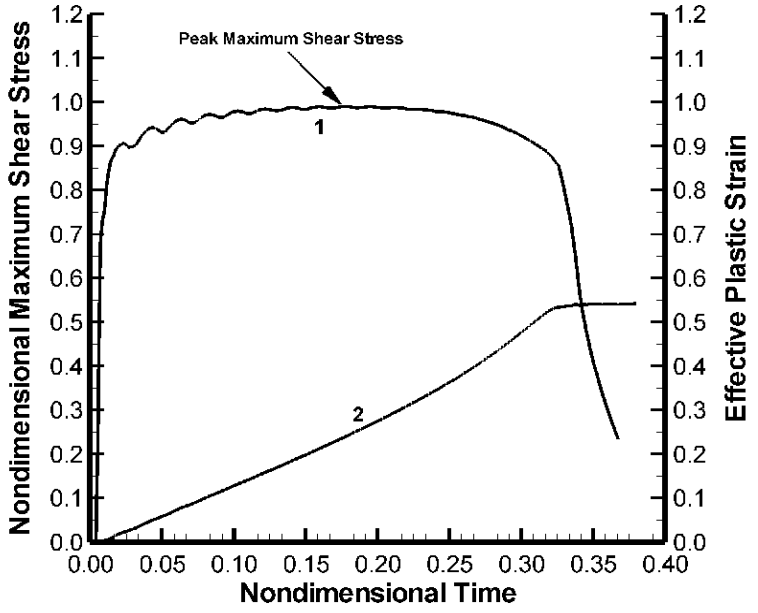

(b)

Figure 2.2. Time histories of the effective plastic strain and the maximum shear stress at two material points W and P in a 4340 steel specimen; Fig. 2a is for point W within an ASB, and Fig. 2b is for point P outside of an ASB.

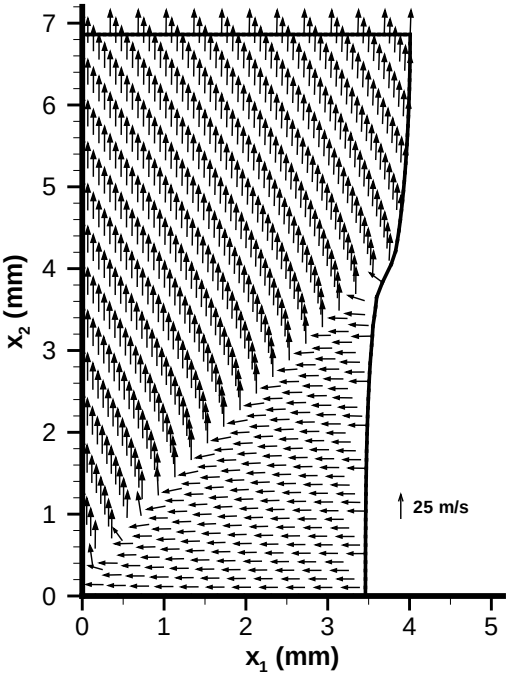

Figure 2.3. Velocity distribution in the deformed configuration at an average axial strain of 0.35.

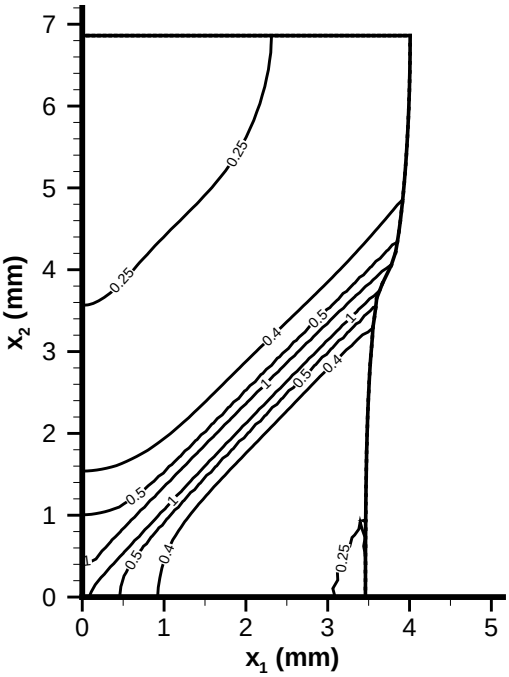

Figure 2.4. Contours of the effective plastic strain in the deformed configuration at an average axial strain of 0.35.

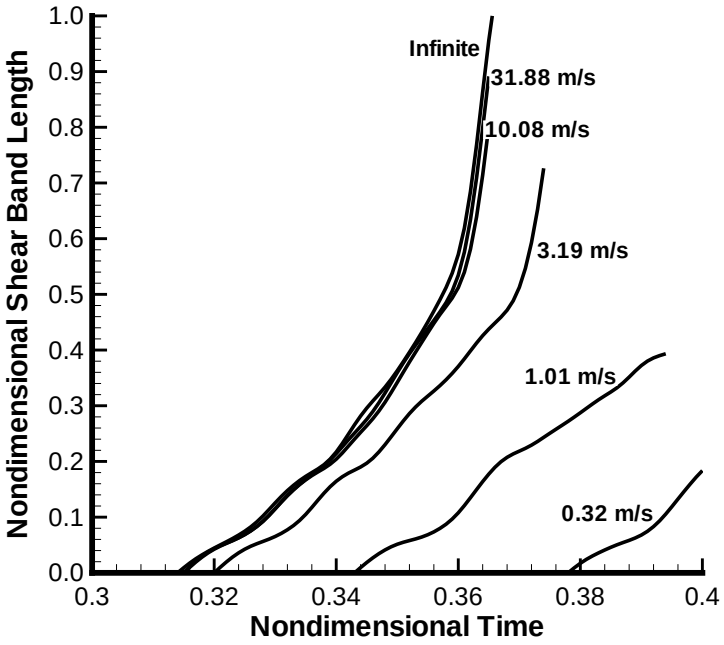

Figure 2.5. Time histories of the ASB length for six values of the thermal wave speed and the weak defect at the specimen centroid.

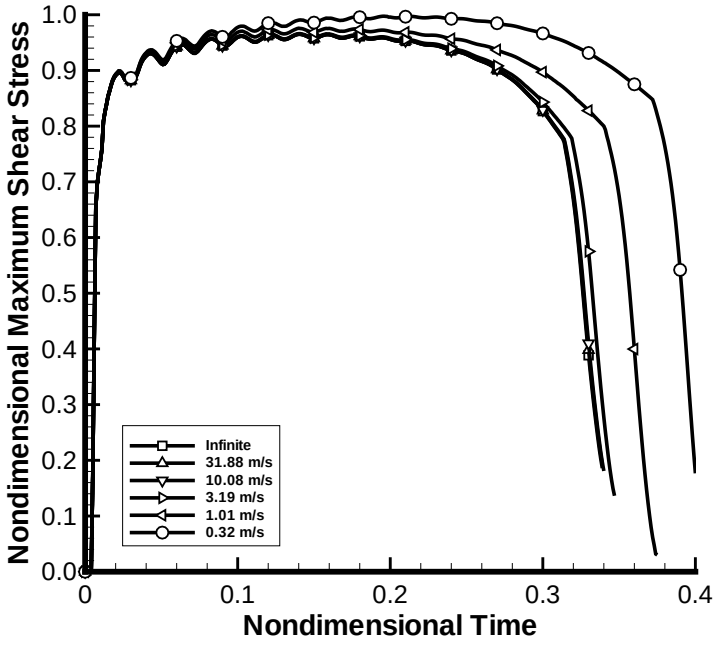

Figure 2.6. For six thermal wave speeds, time histories of the evolution of the maximum shear stress.

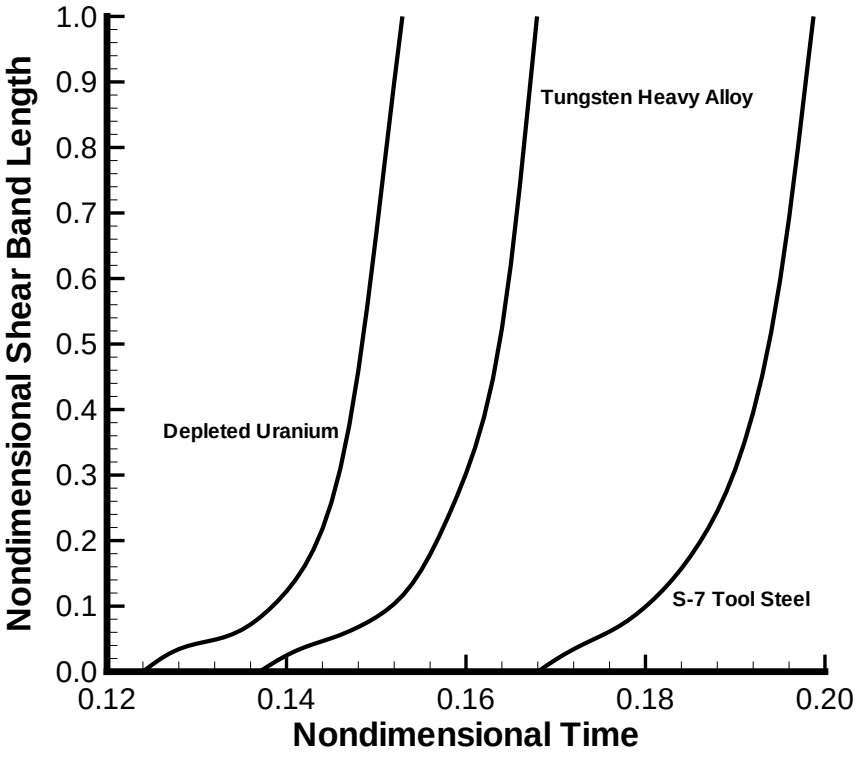
Nondimensional Shear Band Length
Nondimensional Time
Depleted Uranium
Tungsten Heavy Alloy
S-7 Tool Steel
0.0
0.1
0.2
0.3
0.4
0.5
0.6
0.7
0.8
0.9
1.0
0.12
0.14
0.16
0.18
0.20

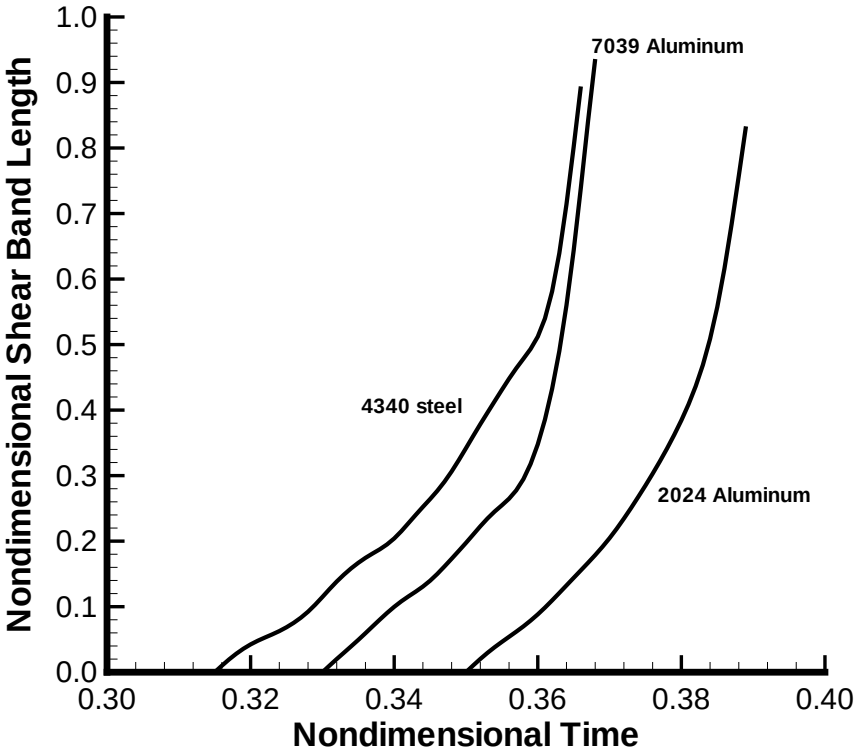
Nondimensional Shear Band Length
Nondimensional Time
7039 Aluminum
4340 steel
2024 Aluminum
0.0
0.1
0.2
0.3
0.4
0.5
0.6
0.7
0.8
0.9
1.0
0.30
0.32
0.34
0.36
0.38
0.40

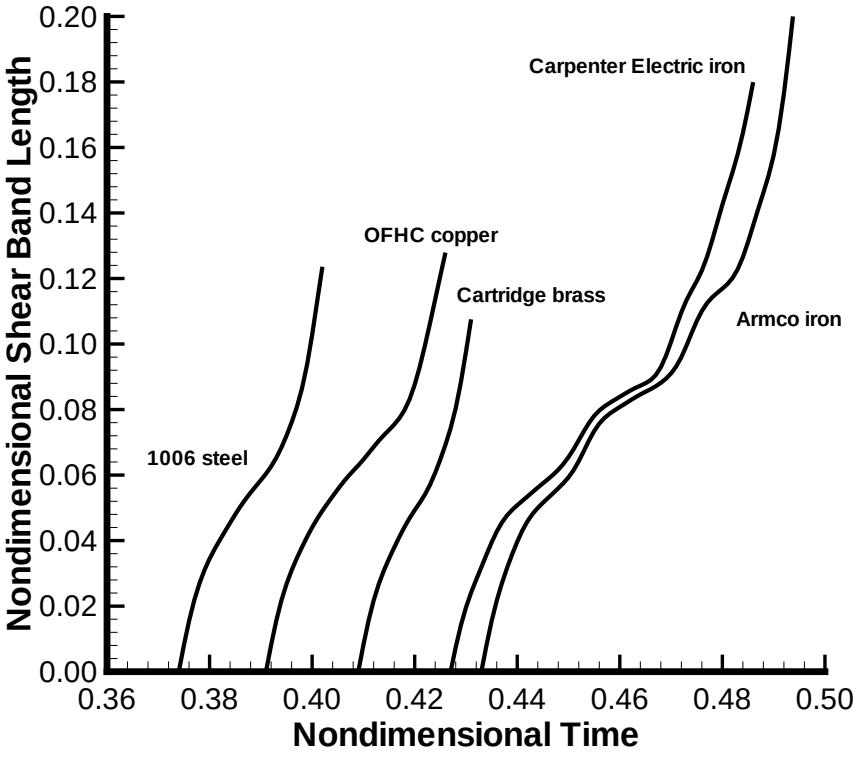
Nondimensional Shear Band Length
0.20
0.18
0.16
0.14
0.12
0.10
0.08
0.06
0.04
0.02
0.00
0.36
0.38
0.40
0.42
0.44
0.46
0.48
0.50
Nondimensional Time
Carpenter Electric iron
OFHC copper
Cartridge brass
Armco iron
1006 steel

(a)

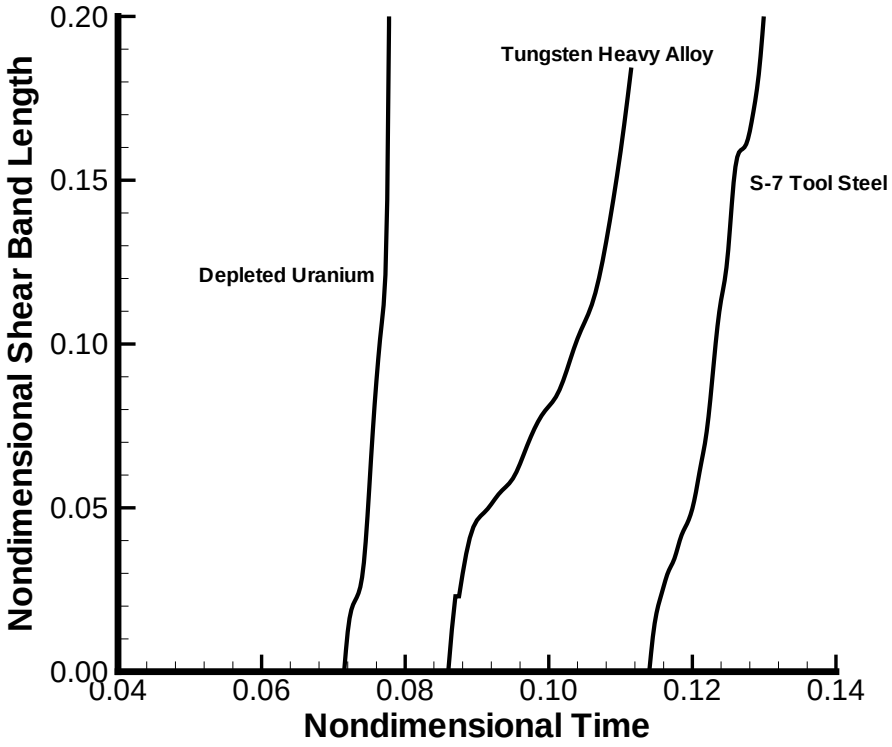
Nondimensional Shear Band Length
0.20
0.15
0.10
0.05
0.00
0.04
0.06
0.08
0.10
0.12
0.14
Nondimensional Time
Depleted Uranium
Tungsten Heavy Alloy
S-7 Tool Steel

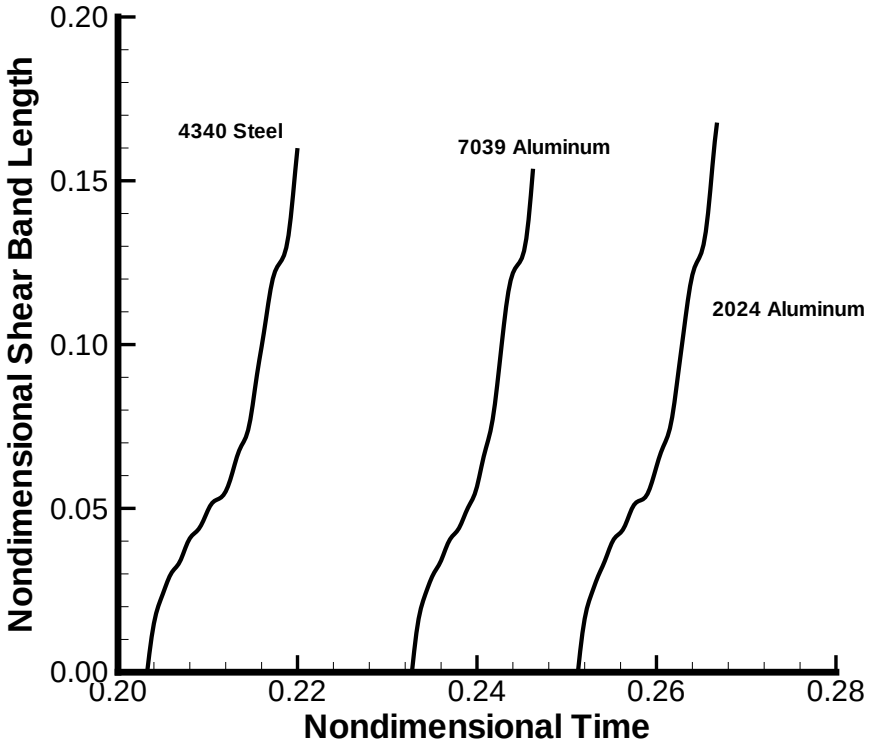
Nondimensional Shear Band Length
0.20
0.15
0.10
0.05
0.00
0.20
0.22
0.24
0.26
0.28
Nondimensional Time
4340 Steel
7039 Aluminum
2024 Aluminum

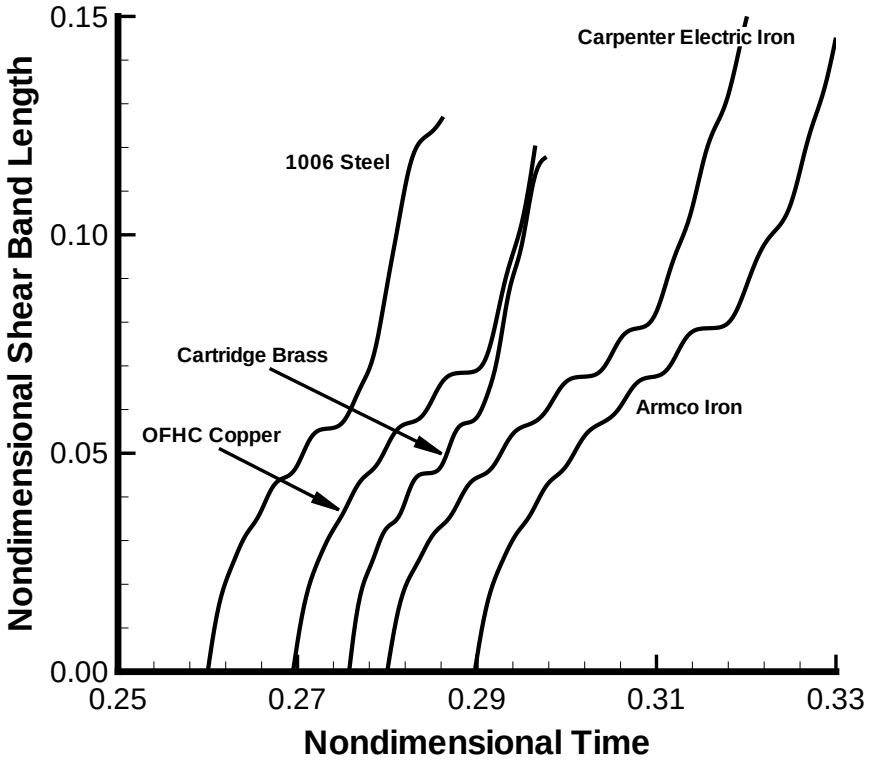

(b)

Figure 2.7. For the eleven materials studied, time histories of the length of an ASB for (a) the weak, and (b) the strong defects.

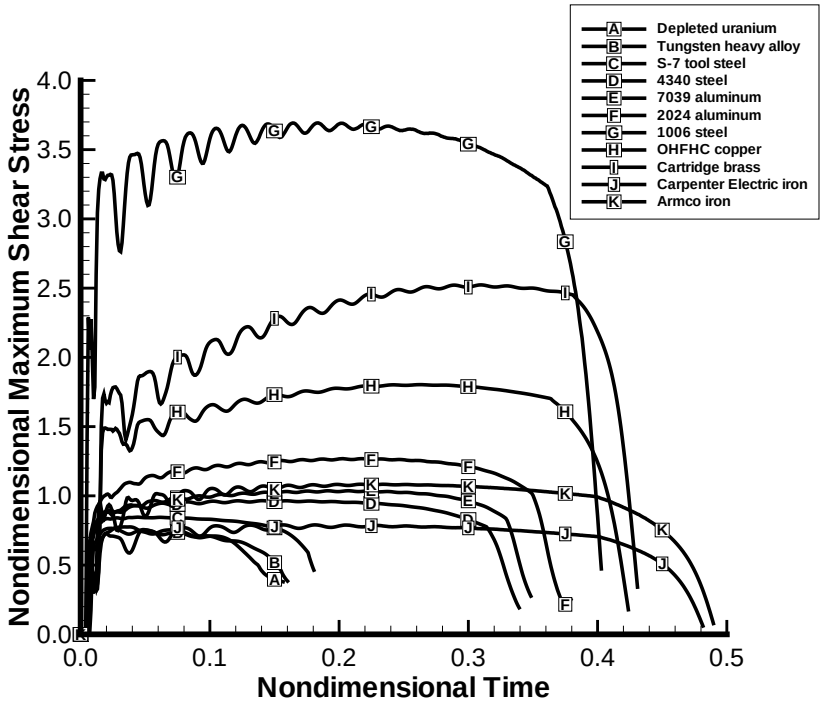
Nondimensional Maximum Shear Stress
Nondimensional Time
0.0
0.5
1.0
1.5
2.0
2.5
3.0
3.5
4.0
0.0
0.1
0.2
0.3
0.4
0.5
A Depleted uranium
B Tungsten heavy alloy
C S-7 tool steel
D 4340 steel
E 7039 aluminum
F 2024 aluminum
G 1006 steel
H OHFHC copper
I Cartridge brass
J Carpenter Electric iron
K Armco iron

(a)

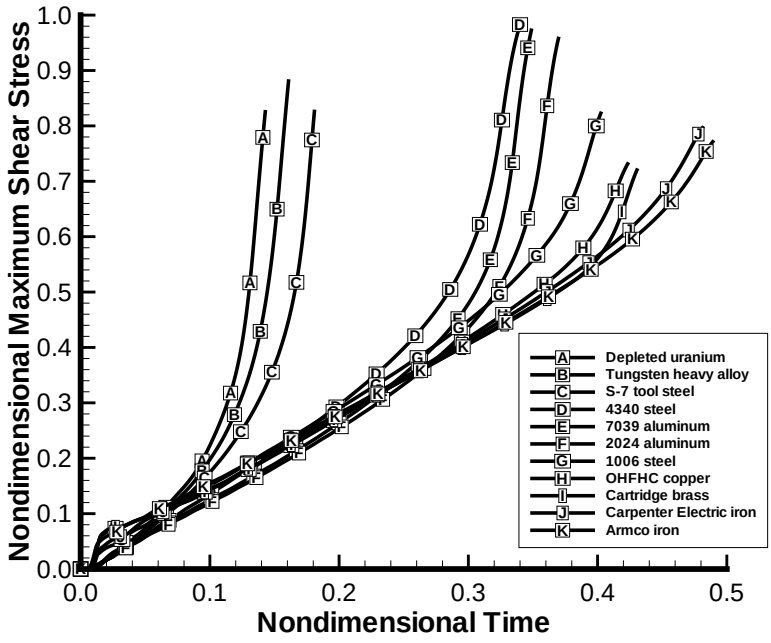
Nondimensional Maximum Shear Stress
Nondimensional Time
0.0
0.1
0.2
0.3
0.4
0.5
0.6
0.7
0.8
0.9
1.0
0.0
0.1
0.2
0.3
0.4
0.5
A Depleted uranium
B Tungsten heavy alloy
C S-7 tool steel
D 4340 steel
E 7039 aluminum
F 2024 aluminum
G 1006 steel
H OHFHC copper
I Cartridge brass
J Carpenter Electric iron
K Armco iron

(b)

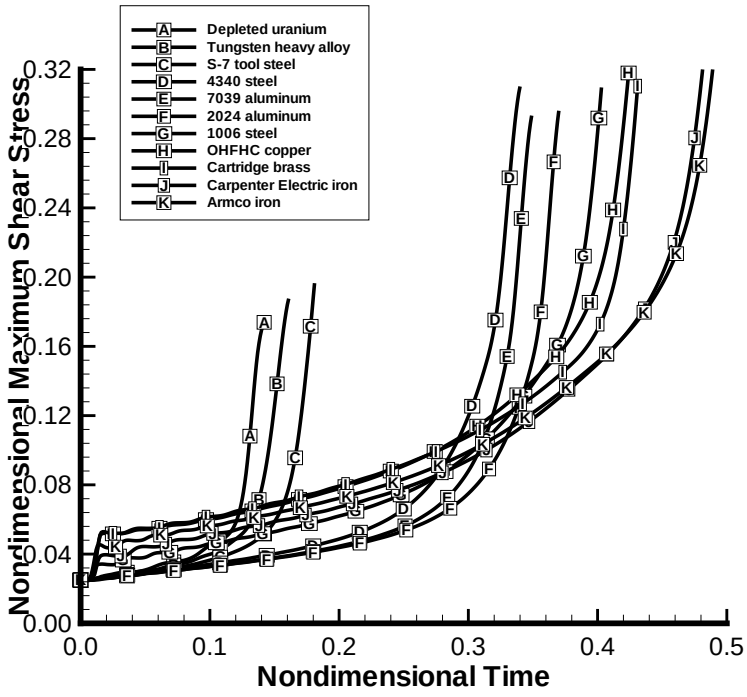

(c)

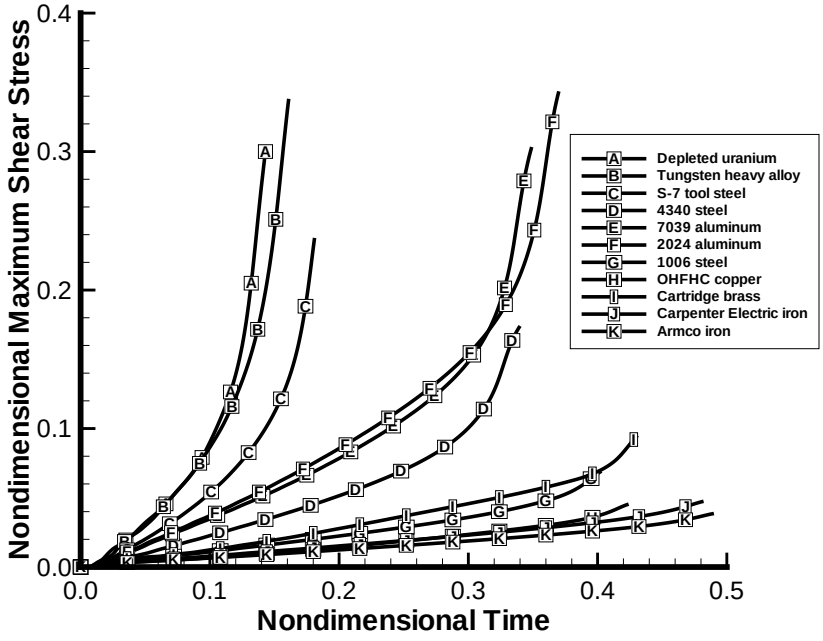

(d)

Figure 2.8. For each one of the eleven materials studied, time histories of the evolution of (a) the maximum shear stress, (b) the effective plastic strain, (c) the porosity, and (d) the temperature at the centroid of the cross-section.

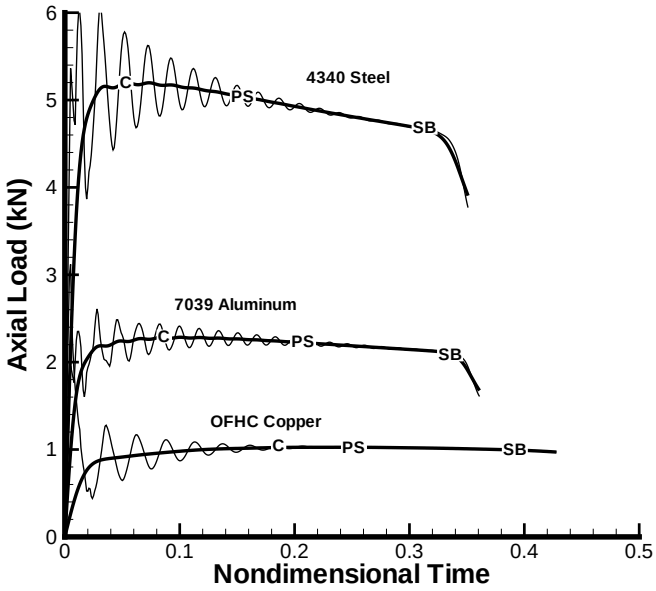

Figure 2.9. Axial load vs. the effective plastic strain for 4340 steel, 7039 aluminum, and OFHC copper with the effective plastic strain from the Considerè condition (C), at the peak maximum shear stress (PS), and at shear band initiation (SB) indicated.

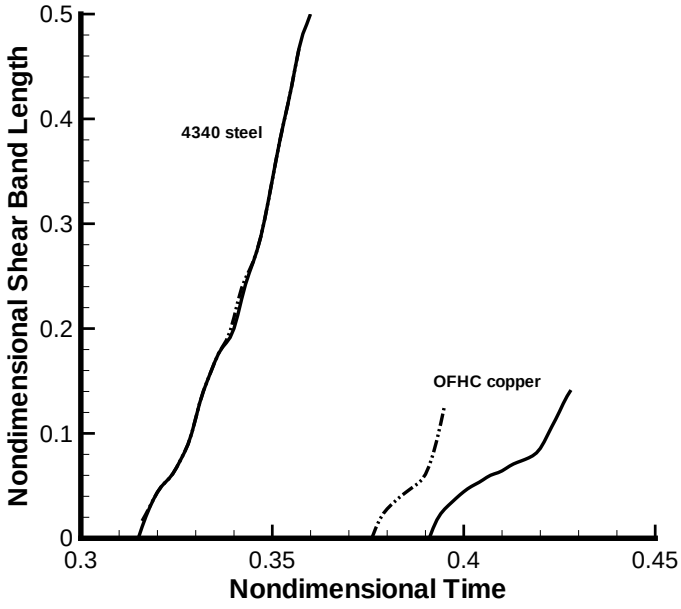

Figure 2.10. Time histories of the length of the shear band for OFHC copper and 4340 steel; the solid and the dashed lines are respectively with and without the effects of heat conduction.

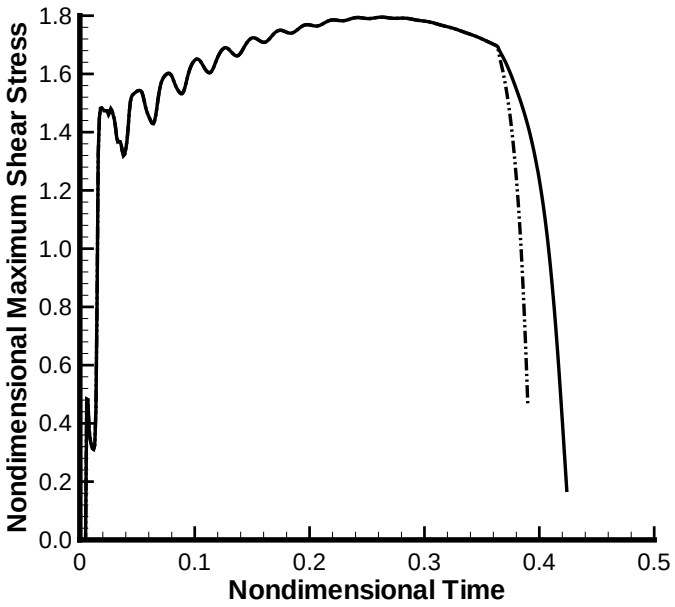

Figure 2.11. Time history of the evolution of the maximum shear stress for OFHC copper at the centroid of the cross section with (solid line) and without (dashed line) the effects of heat conduction.

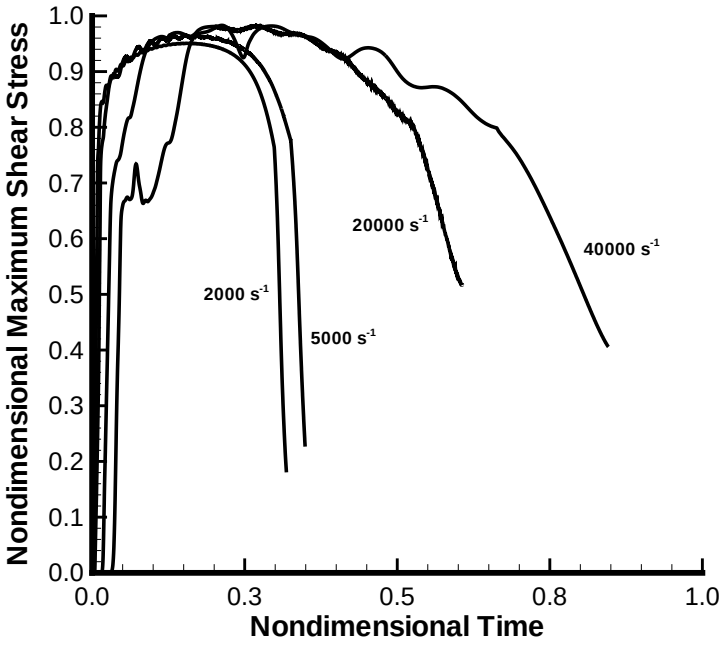

(a)

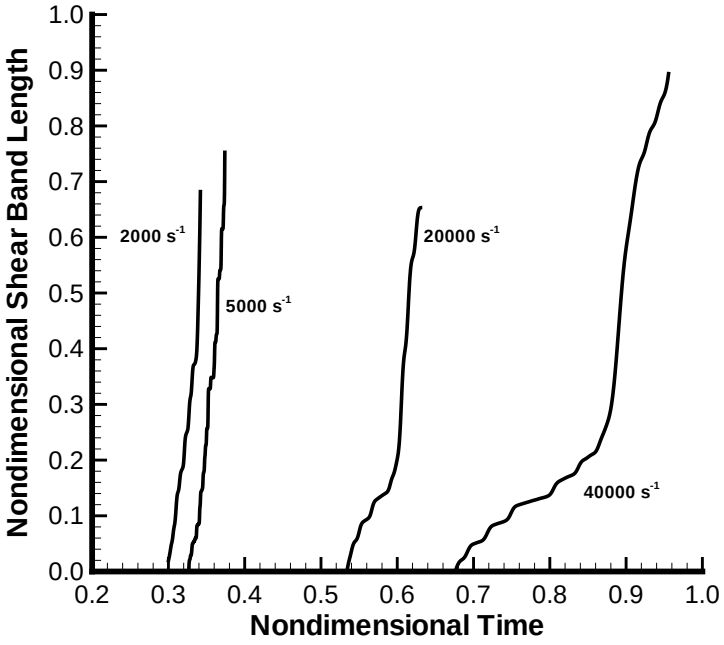

(b)

Figure 2.12. For the 4340 steel using four values of the applied axial strain-rate, time histories of (a) the evolution of the maximum shear stress, and (b) the length of the ASB.

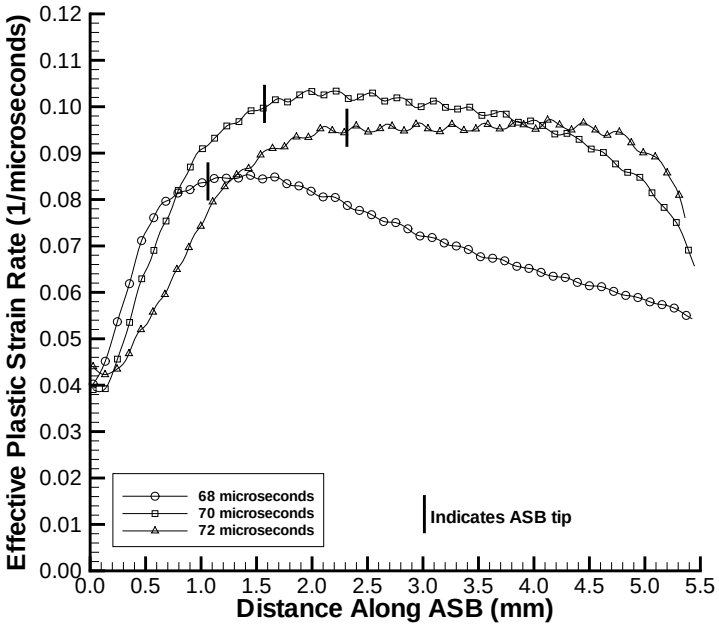

(a)

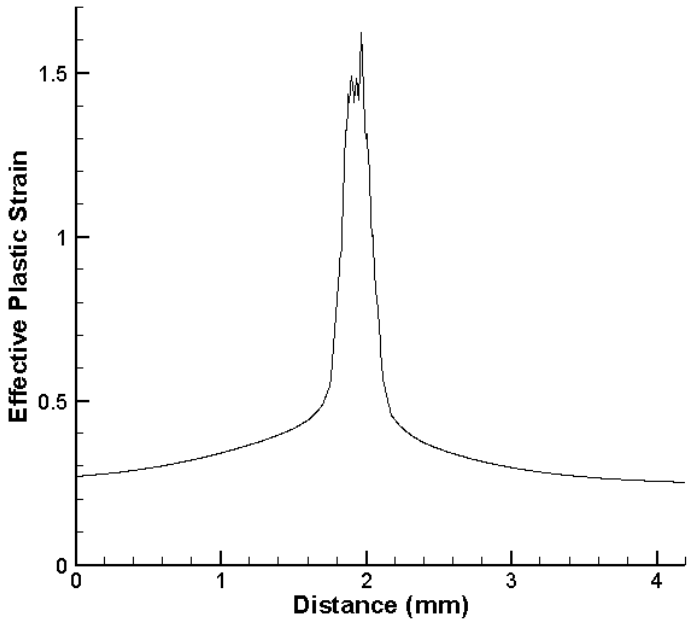

(b)

Figure 2.13. Variation of (a) the effective plastic strain rate along and (b) the effective plastic strain across an ASB in the 4340 steel.

Chapter 3

Simulation of Brittle and Ductile Fracture in an Impact Loaded Prenotched Plate

3.1 Abstract

We analyze the initiation and propagation of a crack from a point on the surface of a circular notch tip in an impact loaded prenotched plate. The material of the plate is assumed to exhibit strain hardening, strain-rate hardening, and softening due to the rise in temperature and porosity. Brittle failure is assumed to initiate when the maximum principal stress at a point reaches a critical level. Ductile failure is assumed to initiate when the effective plastic strain reaches a critical level. A crack initiating from the node where a failure first occurs is taken to propagate to the adjacent node that has the highest value of the failure parameter (the maximum tensile principal stress or the effective plastic strain). The opening and propagation of a crack are modeled by the node release technique. Surface tractions and the heat flux are taken to be null on the newly created crack surfaces. For the brittle failure, the stress field around the crack tip resembles that in mode-I deformations of a prenotched plate loaded in tension. The distribution of the effective plastic strain in a small region around the lower surface of the notch tip is not affected much by the initiation of a crack there except for a shift in the location of the point where the effective plastic strain is

maximum.

3.2 Introduction

Modeling the propagation of a crack during the solution of a transient mechanical problem by the finite element method (FEM) is challenging since the mesh needs to be modified and boundary conditions of null tractions imposed on the newly created crack surfaces. Three strategies used to study fracture are: (i) reducing stresses in the failed region through the evolution of damage in the material (Gurson (1977), Rousselier (1981)), (ii) representing a crack as two traction free surfaces, and (iii) introducing cohesive elements along interelement boundaries that are weak in shear and tension but very strong in compression (Needleman (1987)). Whereas every component of the stress tensor is assumed to drop instantaneously to zero in the first approach, only tractions normal and tangent to the crack surfaces drop suddenly to zero in the second approach. It is easier to model crack propagation along inter-element boundaries than to model intra-element crack propagation since in the former no new elements are created while in the latter they are. However, requiring a crack to propagate along an inter-element boundary requires an a priori assumption on the path of the propagating crack that may not correctly represent the crack's true path. Thus, the accuracy of the inter-element approach can be improved by using a very fine mesh in the region where cracks are expected to initiate and propagate. Here crack propagation along inter-element boundaries is used to analyze the initiation and propagation of brittle and ductile fractures from points in the vicinity of a notch-tip in an impact loaded prenotched plate. Previous studies (e.g. see Needleman and Tvergaard (1995), Zhou et al. (1996a,b), Batra and Nechitailo (1997), Batra and Gummalla (2000), Batra and Ravisankar (2000), Batra and Jaber (2001) and Batra et al. (2003)), of this problem have focused on the initiation of the two failure modes and the impact speed at which the failure mode transitions from brittle to ductile. The interest in the problem was generated by the experimental work of Kalthoff and Winkler (1987) and Kalthoff (1987) who observed that the failure

mode in an impact loaded prenotched plate transitioned from brittle to ductile with an increase in the impact speed. Whereas Batra and Ravisankar (2000) studied 3-dimensional locally adiabatic deformations of the impactor and the thermoviscoplastic plate, other works analyzed plane strain deformations of the system. Except for Batra and Nechitailo (1997), Batra and Ravisankar (2000) and Batra and Gummalla (2000), other works replaced the action of the impactor on the plate by prescribing a normal velocity on the impacted surface of the plate. The 3-dimensional simulations of Batra and Ravisankar (2000) have shown that deformations of the central 3/4th of the plate are analogous to those obtained from the assumption of plane strain but those of points on or adjacent to the front and the rear surfaces of the plate are quite different. Batra and Gummalla (2000) have delineated the effect of different material and geometric parameters on the initiation of the two failure modes. Batra and Jaber (2001) found that four thermoviscoplastic relations calibrated against the same torsion test data predicted quite different values of the impact speed at which failure mode transitions from brittle to ductile. However, deformations of points around the notch tip were qualitatively similar to one another for the four thermoviscoplastic relations; a similar result was obtained by Batra and Kim (1990) and Batra and Chen (2002) for simple shearing deformations of a thermoviscoplastic body.

3.3 Formulation of the Problem

A schematic sketch of the problem studied in shown in Fig. 3.1. A prenotched plate with two edge notches is struck, at normal incidence, by a cylindrical rod of diameter equal to the distance between the two notches. The impactor and the plate are made of the same material that is modeled as isotropic, homogeneous, microporous and thermoviscoplastic. We use rectangular Cartesian coordinates and the referential description of motion to describe their deformations which are governed by the balance of mass, the balance of linear momentum, the balance of moment of momentum, and the balance of internal energy. The local forms of these balance laws and constitutive relations are given in Section 3 of Chapter 2.

For initial conditions, we take

$$\boldsymbol{\sigma}(\mathbf{X},0)=\mathbf{0},\ f(\mathbf{X},0)=0,\ \rho(\mathbf{X},0)=\rho_0,\ \mathbf{v}(\mathbf{X},0)=\mathbf{0},\ \theta(\mathbf{X},0)=300\text{K},\varepsilon_e^p(\mathbf{X},0)=0. \quad (3.1)$$

That is, the plate is initially at rest, stress free, and at a uniform temperature of 300K. All bounding surfaces of the plate including the notch faces but excluding the impacted edge are taken to be traction free and thermally insulated. On the edge surface of the plate impacted by the cylindrical rod,

$$\begin{aligned} v_1(t)/v_0 &= \begin{cases} 0.3t, & 0\le t\le 2\,\mu\text{s},\\ (0.525+0.0375t), & 2<t\le 10\,\mu\text{s},\\ 0.9, & 10<t\le 30\,\mu\text{s},\\ 0.9+(5.4-0.18t), & 30<t\le 35\,\mu\text{s}, \end{cases} \\ T_{21}&=0,\ Q_1=0. \end{aligned} \quad (3.2)$$

Here, v_0 is the speed of the projectile, v_1 the velocity of the plate particles in the x_1-direction, the time t is reckoned from the instant of impact, and it has been assumed that the cylindrical rod contacts the plate edge for 35 μs. The expression (3.2) for v_1 is deduced by fitting straight lines to the data of Batra and Ravisankar (2000) who studied 3-dimensional deformations of the plate and the projectile. Equations $(3.2)_5$ and $(3.2)_6$ imply that the contact surface is smooth and thermally insulated.

A weak formulation of the problem is derived in the same way as in Chapter 2 except that now a weak form of

$$\dot{\mathbf{x}}=\mathbf{v}(\mathbf{X},t) \quad (3.3)$$

is also derived. We thus get coupled nonlinear ordinary differential equations

$$\dot{\mathbf{d}}=\mathbf{F} \quad (3.4)$$

where $\mathbf{d}$ is the vector of unknowns and $\mathbf{F}$ is the force vector that depends upon time t and $\mathbf{d}(t)$. The twelve unknowns at a node are $\{x_1,x_2,v_1,v_2,\sigma_{11},\sigma_{22},\sigma_{12},\sigma_{33},f,\theta,\xi,\varepsilon_e^p\}$. For a 3-node triangular element, each one of these variables is a polynomial of degree 1 in the X_1 and X_2 coordinates of nodes. Recall that natural boundary conditions are embedded in (3.4). Equations (3.4) are modified to enforce essential boundary conditions (3.2) at nodes on the

impact surface, and are then integrated by using the subroutine LSODE with parameter MF in the subroutine set equal to 10 and parameters $ATOL = RTOL = 10^{-7}$. $ATOL$ and $RTOL$ control the absolute and the relative tolerances in the computed solution. $MF = 10$ implies that the subroutine uses the Adam-Moulton method of integrating ODEs. LSODE adaptively adjusts the size of the time step and the order of the method in order to compute the solution within the prescribed accuracy.

In order to determine the speed at which the failure mode changes from brittle to ductile or vice-versa, we need a criterion for the failure mode initiation. Ritchie et al. (1973) have proposed that the brittle failure initiates at a point when $\sigma_p/\sigma_0 = 3.0$ over a certain length which is characteristic of the microstructure of the material and generally equals a grain diameter. Here σ_p is the maximum principal stress at a point. Tensile experiments of Hendrickson et al. (1958) at nominal stress rates of about 1 to 10^4 MPa s^{-1} show that brittle failure occurs at $\sigma_p/\sigma_0 = 2.34$ for a prenotched steel specimen with a yield stress of 705 MPa. This value of σ_p/σ_0 was found to be essentially independent of the temperature and the rate of loading. In numerical simulations, Zhou et al. (1996b), Batra and Gummalla (2000), Batra and Ravisankar (2000), Batra and Jaber (2001), and Batra et al. (2003) presumed that the brittle failure initiates when $\sigma_p/\sigma_0 = 3.0,\ 2.0,\ 2.0,\ 2.34$ and 2.34 respectively. For the configurations, the material, and the impact speeds studied by the first three investigations, no brittle failure initiated at any point in the prenotched plate. Here, we assume that the brittle failure initiates when $\sigma_p/\sigma_0 = 2.0$. Our goal is to analyze the effect crack propagation has on the deformation fields; thus, the precise value of σ_p/σ_0 at the instant of the brittle failure initiation is less critical. Ductile failure is generally believed to occur due to the nucleation and coalescence of voids within an adiabatic shear band (ASB). However, previous analyses of the problem by Needleman and Tvergaard (2000), and Batra and Jaber (2001) have shown that the porosity does not reach 0.25, the value for the initiation of a ductile failure (e.g. see Curran et al. (1987)). Accordingly, the ductile failure is assumed to initiate at a point as soon as an ASB forms there.

Batra and Rattazzi (1997) studied the initiation and propagation of an ASB in a thick-walled steel tube and found that the choice of the ductile failure criterion will affect the predicted initiation time. They used four different failure criteria: (i) $\varepsilon_e^p = 0.5$, (ii) $\varepsilon_e^p = 1.0$; (iii) the effective stress has dropped to 90% of its peak value and the material point is deforming plastically, and (iv) the effective stress has dropped to 80% of its maximum value and the material point is deforming plastically. Since the time of initiation of an ASB depends upon the criterion, the impact speed at which failure mode transition occurs will also be dependant upon the choice of the failure criteria.

In order to simulate crack initiation and propagation, we assume that as soon as a failure criterion is met at a node, say N, an additional node N^*, coincident with N but not connected to it, is added to the finite element mesh. The node N^* is connected to the node N^{**} that has the next highest value of σ_p for the propagation of the brittle failure and ε_e^p for the propagation of the ductile failure. The elements are adjusted such that all of the nodes originally connected to N on one side of the newly formed crack are connected to N^* instead. Thus lines NN^{**} and N^*N^{**} overlap at the instant of the initiation of a fracture and each is an interelement boundary between two adjoining elements. Note that no new element is created. Subsequent deformations of the body will either move N and N^* apart or tend to push them together. In the former case, surface tractions and the normal component of the heat flux are assumed to be null on the crack surfaces. In the later case, in order to prevent interpenetration of the material through the crack surfaces, small 2-node stiff-spring contact elements, weak in tension but stiff in compression, are added between nodes N and N^*. The constitutive relation for the stiff-spring is taken to be

$$F = kx_n, \tag{3.5}$$

where

$$k = \begin{cases} 0, & x_n/x_0 \geq 0, \\ E\ell\left[1 + (\eta E - 1)\left(\dfrac{x_n}{x_0}\right)^2\right], & -1 \leq x_n/x_0 < 0, \\ \eta E\ell, & x_n/x_0 < -1. \end{cases} \tag{3.6}$$

Here F is the normal force between nodes N and N^*, E Young's modulus of the matrix material, x_n the relative displacement between nodes N and N^* normal to the crack surface, ℓ a characteristic length, and η is constant. Equations (3.5) and (3.6) imply that the normal force between nodes N and N^* equals zero when they are separate but tends to push them apart in case of interpenetration.

3.4 Computation and Discussion of Results

Results are computed for a 4340 steel plate and impact speeds of 20, 50 and 60 m/s. Values of material parameters in the Johnson-Cook relation are listed in Table 2.1 and equation (2.25) of Chapter 2. Parameters in equations (3.5) and (3.6) are assigned the following values:

$$\eta = 10,\ x_0 = 0.01 \text{ mm},\ \ell = 1\,\text{mm}. \tag{3.7}$$

Because of the symmetry of the plate geometry and the initial and boundary conditions, deformations of the plate will be symmetric about the x_1 x_3-plane passing through the plate centroid. Thus deformations of the upper half of the plate are analyzed.

An unstructured mesh of 3,998 3-node triangular elements with 21 evenly spaced nodes around the notch tip generated using TECPLOT is used. The mesh and a blow-up of the mesh around the notch tip are shown in Fig. 3.2. Fine elements are placed in the region containing anticipated paths of the brittle and the ductile failures; Kalthoff (1987) and Kalthoff and Winkler (1987) have given these paths based on their tests. The results in figure 3.3 for the nondimensional maximum principal stress for $v_o = 20$ m/s and in figure 3.4 for the ratio of the effective plastic strain and the effective plastic strain at ductile failure ($\varepsilon_e^p/\varepsilon_c$) show that the results from this mesh are very similar to those from a finer mesh with 8,712 3-node triangular elements and 41 evenly spaced nodes around the notch tip. In order to prevent contact between points on the two surfaces of a notch during deformations of the prenotched plate, the surface of the notch that is away from the impacted edge is taken to be inclined rather than being horizontal; the same strategy was adopted by Batra and

Nechitailo (1997), and Batra and Gummalla (2000). It should not affect deformations of the material directly ahead of the impacted surface and of material points on the notch tip.

The impact of the plate by the rod causes a compressive longitudinal wave to travel into the plate towards the notch tip. For values of E, ν, and ρ used for the plate material, analytical speed for the longitudinal wave equals 5.77 mm/μs. Because of the interaction among nodes as represented by nondiagonal mass and stiffness matrices, the computed wave speed is usually larger than the analytical value; the difference between the two speeds depends upon the finite element mesh. Upon arrival of the wave at the notch tip, the material there is significantly deformed because deformations are essentially singular. The computed velocity field in the plate is similar to that plotted in Fig. 4 of Batra and Gummalla's (2000) paper and is not shown here. Material particles adjacent to the lower traction free surface of the notch move to the right, i.e., in the direction of the applied velocity v_0, and those close to the upper traction free surface of the notch are stationary till the loading wave arrives at the notch tip. The displacement in the direction of v_0 of particles on the lower surface of the notch stretches material lines on the curved surface of the notch, distorts the shape of the notch tip, and induces a tensile hoop stress at points on the upper surface of the notch tip. The maximum tensile principal stress occurs at a point inside the body near the notch surface at a point that in the reference configuration makes an angle of approximately 70° counterclockwise with the notch-axis. This point is hereafter referred to as point B and is indicated in figure 3.2b. The effective plastic strain is a maximum at a point on the lower notch surface. This point is hereafter referred to as point D and is indicated in figure 3.2b. Coordinates of points B and D in the reference configuration are (50.09 mm, 25.20 mm) and (50.08 mm, 24.87 mm), respectively. Lines joining B and D to the center of the circular notch tip make angles of 65.8° counterclockwise and 58.4° clockwise with the axis of the notch. These are in general agreement with the observations of Kalthoff and Winkler (1987), and also of previous numerical investigations (e.g. see Batra and Jaber (2001)). For an impact speed of 50 m/s, Fig. 3.5a depicts contours of the nondimensional maximum principal stress,

($\sigma_p/2\sigma_o$) in a small region around the notch tip immediately prior to the occurrence of the brittle failure ($\sigma_p/2\sigma_o = 1$). Here σ_o is taken to be A from Eqn. 2.16. For an impact speed of 60 m/s, figure 3.5b depicts the contours of the ratio of the effective plastic strain and the effective plastic strain at ductile failure ($\varepsilon_e^p/\varepsilon_c$) in a small region around the notch tip immediately prior to the onset of the ductile failure ($\varepsilon_e^p/\varepsilon_c = 1$). It is clear from figure 3.5 that brittle failure will initiate at a point close to the upper notch surface and ductile failure will initiate at a point on the lower notch surface. At plate particles directly ahead of the notch-tip, we have plotted in Fig. 3.5c the variation of the non-dimensional shear stress (σ_{12}/σ_o) with the distance from the notch-tip. The traction free boundary condition on the notch surface requires that $\sigma_{12} = 0$ at the notch tip ($r = 0$). For $v_o = 20$ and 50 m/s, the shear stress variation evinces a boundary layer in the sense that its magnitude increases rapidly, attains a maximum at $r = 0.2$ mm, and then gradually decreases. The maximum value of $|\sigma_{12}|$ is not that much affected by the impact speed. Ching and Batra (2001) were the first to identify this boundary layer; they analyzed static elastic deformations of the prenotched plate by the meshless local Petrov-Galerkin method.

Time histories of evolution of the maximum principal tensile stress at point B and of the effective plastic strain at point D are exhibited in Fig. 3.6a,b. These plots reveal the following: (i) the rate of the rise of the effective plastic strain at point D and the maximum principal stress at point B increase with an increase in impact speed, (ii) the change in the peak value of the maximum principal stress induced at B is miniscule when the impact speed is increased from 50 m/s to 60 m/s; however, the increase in the effective plastic strain at D is considerable when the impact speed is increased from 50 m/s to 60 m/s, and (iii) the brittle failure will likely initiate first at impact speeds of 20 and 50 m/s and the ductile failure at an impact speed of 60 m/s. The failure mode transition speed can be read from figure 3.7 where plots of the time of initiation of the two failure modes against the impact speed are shown. Figure 3.7 indicates that the transition speed for this material and configuration is approximately 54 m/s. This failure mode transition speed differs noticeably from the 23

m/s computed by Batra and Jaber (2001) because of the differences in the values of the material parameters and the criteria employed for the initiation of the brittle and ductile failures. Values of the material parameters used by Batra and Jaber (2001) were such that the material exhibited considerably more thermal softening than the material studied herein. Values of other material parameters in the two studies are also quite different. We note that times of initiation of the brittle and the ductile failures indicated in fig. 3.7 are without the opening of a crack. Once a crack starts from point B, the initiation of the ductile failure occurs at $t = 52$ and 22.2μs for $v_o = 20$ and 50 m/s, respectively. Thus, the opening of a crack delays the initiation of the ductile failure, and the time lag is significant at low impact speeds. Similarly, for $v_o = 60$ m/s when a crack develops at point D, the initiation of the brittle failure at point B is postponed by 1.7μs.

To simplify the computations for the study of crack propagation, fracture is assumed to initiate either at a point on the notch surface or at a point on the nearly circular arc next to the notch surface. As shown in figure 3.5, this method will accurately capture ductile fracture; however, it will not precisely capture the time of initiation of the brittle fracture. Using this assumption, the failure initiation times were 24.5 μs, 18.5 μs, and 15.2 μs for $v_0 = 20, 50$, and 60 m/s, respectively. The actual failure initiation times were found to be 21.4 μs, 18.16 μs, and 15.2 μs. For $v_0 = 20$ m/s, Fig. 3.8a,b exhibits contours of the maximum principal stress at $t = 25$ μs with and without modeling the opening of a crack at the point of initiation of the brittle failure. Contours of the maximum principal stress around the crack tip at $t = 45$ μs are depicted in Fig. 3.8c. A comparison of the computed stress field with that given in Fig. 19 of Kalthoff (2000) shows that a predominantly mode-I stress field forms around the brittle crack tip. When stress fields in Figs. 3.8b and 3.8c are compared with each other, it becomes apparent that the crack shifts the concentration of the stresses from a point straight ahead of the starter notch tip to that near the crack tip. The sharp gradients in the effective stress formed adjacent to the traction free crack surfaces are due to oscillations associated with the formation of new surfaces and consequent

emanation of elastic unloading waves; the magnitude of oscillations diminishes with time. These transients could possibly have been diminished by gradually rather than immediately reducing the surface tractions to zero at points on the newly created surfaces. However, this was found to inhibit the growth of the crack.

Computed results can only be compared qualitatively with those of Kalthoff (1987) since this paper listed only the hardness number for the material of the plate. The time history of the crack length is given in Fig. 3.9a for $v_0 = 20$ and 50 m/s. For both cases, the crack growth exhibits an approximately affine behavior with a crack propagation speed of 1.6 km/s or 28% of the longitudinal wave speed for this material. For both impact speeds, the crack propagated along a path that made an angle of approximately 60° counterclockwise with the axis of the notch. In Kalthoff's (1987) and Kalthoff and Winkler's (1987) experiments, the angle between the crack path and the notch axis equaled 70°. The deformed shape of the plate at after complete perforation ($t = 80\mu$s) for $v_o = 50$ m/s is shown in fig. 3.9b.

For $v_0 = 60$ m/s, ductile failure preceded the brittle failure and initiated from point D on the notch surface. The ductile failure propagated along a line that in the present configuration makes an angle of 15° clockwise with the notch axis. We have plotted in Figure 3.10a-d, contours of the effective plastic strain just before, immediately after, and a few μs subsequent to the initiation of a crack due to ductile failure. It is clear that the presence of a crack due to the ductile failure does not have a significant effect on the general distribution of the effective plastic strain in a small region surrounding the lower portion of the notch tip. However, at points close to the crack surface, the effective plastic strain is considerably higher than that at other points. In the deformed configuration depicted in Fig. 3.10c, a leaflet like opening has formed in the intensely deformed region surrounding the lower surface of the notch tip; a similar deformation pattern was computed by Batra and Gummalla (2000) who used DYNA2D, a mesh comprised of 4-node quadrilateral elements and neglected the effects of heat conduction and porosity. As the crack due to ductile failure propagates, the leaflet is incorporated into the crack surface (cf. Fig. 3.10c,d). For $v_o = 50$ m/s, fig. 3.11a depicts

the time history of the evolution of the effective plastic strain at point D both with and without the opening of a crack from point B where brittle failure first occurs. It is clear that the opening of the crack at point B significantly influences the effective plastic strain developed at point D. However, as should be apparent from the results plotted in fig. 3.11b, the principal stress at point B is not influenced by the opening of a crack at point D because the crack starting from D has not propagated much into the plate.

Contours of the temperature in the vicinity of the crack plotted in Fig. 3.12a,b reveal that the maximum temperature near the crack tip increases from about 475 K to 775 K which equal approximately 25% and 45% of the melting temperature of the material. The maximum temperature occurs at a point on the crack surface and is behind the crack tip. The analysis was halted at $t = 34$ μs due to the excessive distortion of the mesh in the vicinity of the leaflet region. The crack length of 0.36 mm at this instant indicates that the ductile failure has not propagated much into the plate. A possibility is to adaptively refine the mesh within the severely deformed region and transfer from the previous mesh the state of deformation at nodes of the new mesh; however, this was not pursued because it smears out the deformation fields.

3.5 Conclusions

We have analyzed transient coupled thermomechanical deformations of a prenotched 4340 steel plate whose edge between the two parallel notches is impacted by a cylindrical projectile of diameter equal to the distance between the notches. The novel feature of the work is the simulation of the initiation and propagation of cracks due to brittle and ductile failures. It has been found that the brittle failure initiates first at low impact speeds and the ductile failure occurs first at high impact speeds and that for this configuration and material failure mode transition occurs at an impact speed of approximately 54 m/s. The crack due to the brittle failure propagates all the way through the plate and splits it into two pieces. However,

due to excessive distortion of the mesh in the intensely deformed region, the propagation of only a small crack due to the ductile failure could be simulated. The temperature rise in the vicinity of this small crack equaled approximately 45% of the melting temperature of the material.

3.6 References

Batra, R. C., Nechitailo, N. V., Analysis of Failure Modes in Impulsively Loaded Pre-notched Plates, *Int. J. Plasticity* **13**, 291-308 (1997)

Batra, R. C., Gummalla R. R., Effect of Material and Geometric Parameters on Deformations Near the Notch-tip of a Dynamically Loaded Prenotched Plate. *Int. J. of Fracture* **101**, 99-140 (2000)

Batra, R. C., Ravisankar M. V. S., Three-dimensional Numerical Simulation of the Kalthoff Experiment, *Int. J. Fracture* **105**, 161-186 (2000)

Batra, R. C., Jaber, N. A., Failure Mode Transition in an Impact Loaded Prenotched Plate with Four Thermoviscoplastic Relations, *Int. J. Fracture*, **110**, 47-71 (2001)

Batra, R. C., Jaber, N. A., Malsbury, M. E., Analysis of Failure Modes in an Impact Loaded Thermoviscoplastic Prenotched Plate, *Int. J. Plasticity*, **19**, 139-196 (2003)

Batra, R. C., Chen L., Effect of Viscoplastic Relations on the Instability Strain, Shear Band Initiation Strain, the Strain Corresponding to the Maximum Shear Band Spacing, and the Band Width in a Thermoviscoplastic Material, *Int. J. Plasticity*, **17**, 1465-1489 (2001)

Batra R.C., Kim, K. H., Effect of Viscoplastic Flow Rules on the Initiation and Growth of Shear Bands at High Strain Rates, *J. Mechs. Phys. Solids*, **38**, 859-874 (1990)

Batra, R. C., Rattazzi, D., Adiabatic Shear Banding in a Thick-walled Steel Tube, *Comp. Mech.*, **20**, 412-426 (1997)

Curran, D. R., Seaman, L., Shockey, D. A., Dynamic Failure of Solids, *Physics Reports*, **147**,

253-388 (1987)

Gurson, A. L., Continuum Theory of Ductile Rupture by Void Nucleation and Growth: Part I, *J. of Engr. Mater. and Tech.*, **99**, 2-15 (1977)

Hendrickson, J. A., Wood, D. S., Clark, D. C., The Initiation of Brittle Fracture in Mild Steel, *J. Mech. Phys. Solids*, **50** 656-681 (1958)

Kalthoff, J. F., Shadow Optical Analysis of Dynamic Shear Failure, *SPIE, Photomechanics and Speckle Metrology* **814**, 531-538 (1987)

Kalthoff, J. F., Modes of Dynamic Shear Failure in Solids, *Int. J. Fracture* **101**, 1-31 (2000)

Kalthoff, J. F., Winkler, S., Failure Mode Transition at High Rates of Shear Loading, *Impact Loading and Dynamic Behavior of Materials* **1**, 185-195 (1987)

Needleman, A., A Continuum Model for Void Nucleation by Inclusion Debonding, *J. App. Mech.* **54**, 525-531 (1987)

Needleman, A., Tvergaard, V., Analysis of a Brittle-Ductile Transition Under Dynamic Shear Loading, *Int. J. Solids Struct.* **32**, 2571-2590 (1995)

Needleman, A., Tvergaard, V., Numerical Modeling of the Ductile-Brittle Transition, *Int. J. Fracture* **101**, 73-97 (2000)

Ritchie, R. O., Knott, J. F., Rice, J. R., On the Relationship Between Critical Tensile Stress and Fracture Toughness in Mild Steel, *J. Mech. Phys. Solids* **21**, 395-410 (1973)

Rousselier G., Ductile Fracture Models and their Potential in Local Approach to Fracture, *Nuclear Engr. and Design*, **105**,97-111 (1987)

Zhou, M., Ravichandran, G., Rosakis, A., Dynamically Propagating Shear Bands in Impact-Loaded Prenotched Plates–I, *J. Mech. Phys. Solids*, **44**, 981-1006 (1996a)

Zhou, M., Ravichandran, G., Rosakis, A., Dynamically Propagating Shear Bands in Impact-Loaded Prenotched Plates–II, *J. Mech. Phys. Solids*, **44**, 1007-1032 (1996b)

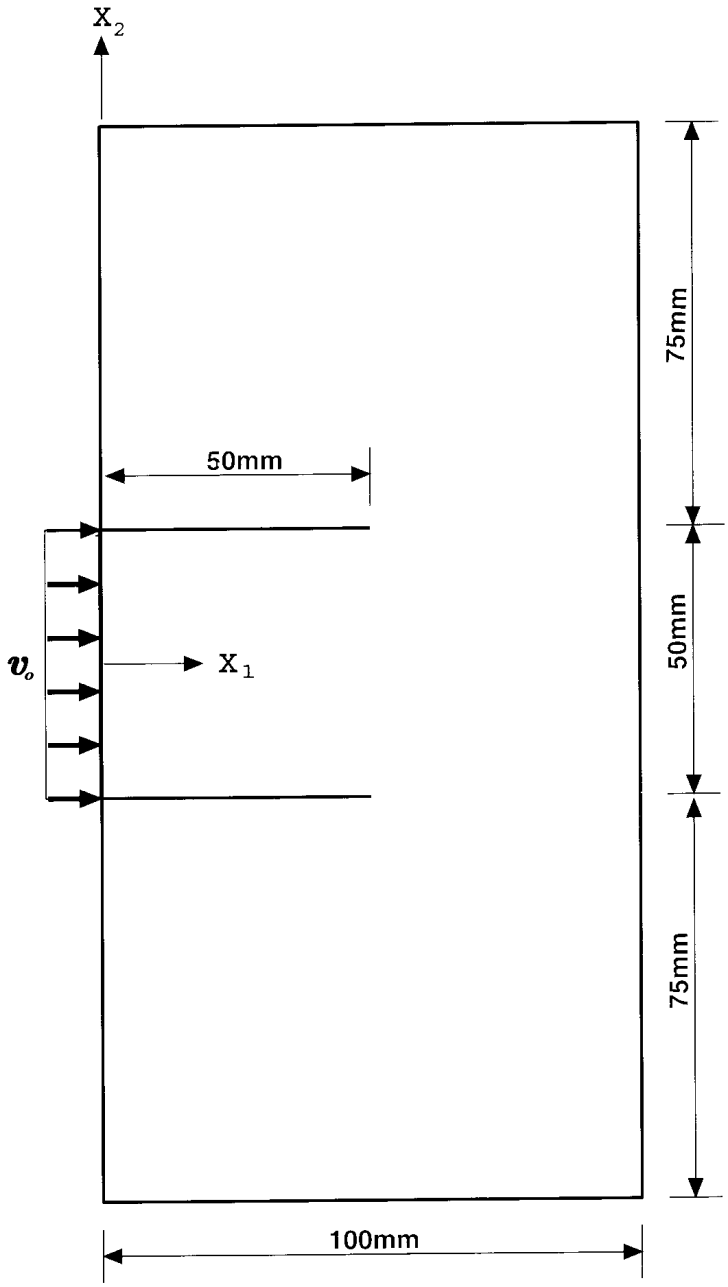

Figure 3.1. Schematic sketch of the problem studied. The notch tip radius is 0.15 mm.

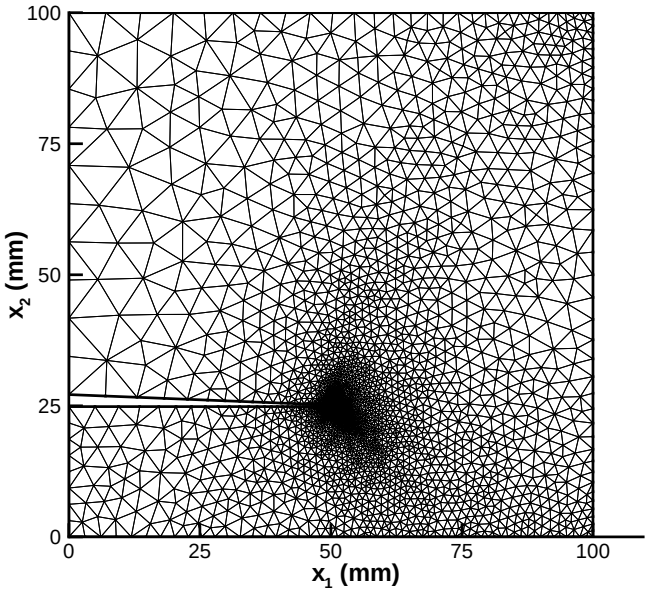

(a)

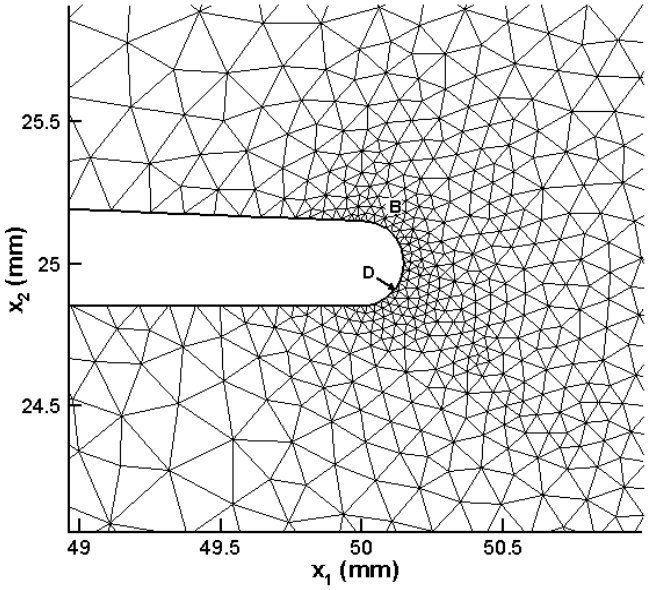

(b)

Figure 3.2. (a) Finite element discretization of the upper half of the plate, and (b) the finite element mesh in a small region surrounding the notch tip. Locations of point B (50.09 mm, 25.20 mm) and point D (50.08 mm, 24.87 mm) where the maximum principal tensile stress and the maximum effective plastic strain occur are also indicated.

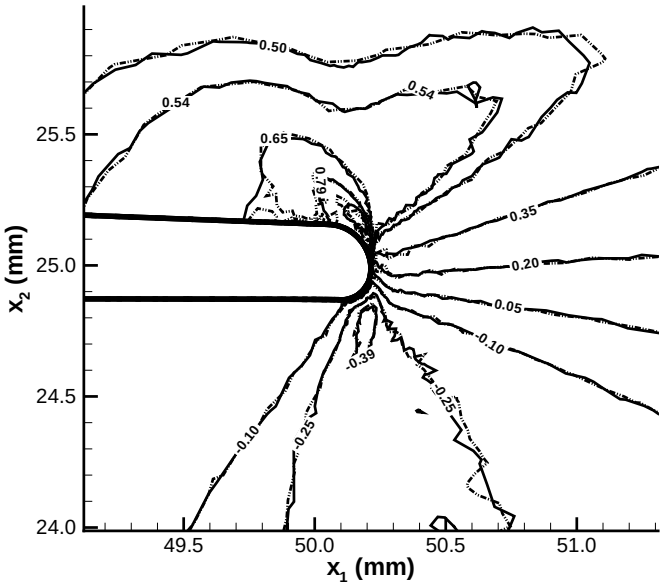

Figure 3.3. For $v_o = 20$ m/s, contours of the nondimensional maximum principal stress for two meshes at $t = 20\mu$s. Dashed lines are for a mesh with 3,998 3-node elements, and solid lines are for a mesh of 8,712 3-node elements.

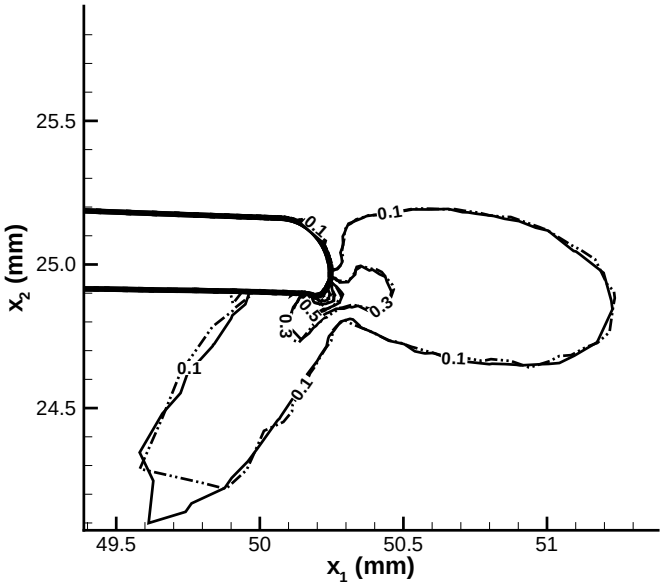

Figure 3.4. For $v_o = 50$ m/s, contours of $\varepsilon_e^p/\varepsilon_c$ for two meshes at $t = 20\mu$s. Dashed lines are for a mesh with 3,998 3-node elements, and solid lines are for a mesh of 8,712 3-node elements.

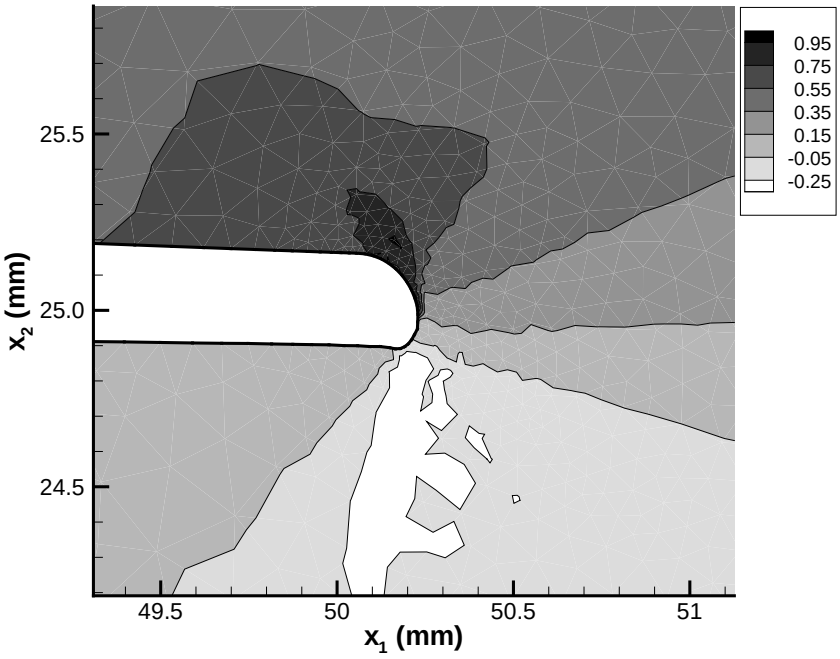
0.95
0.75
0.55
0.35
0.15
-0.05
-0.25
25.5
25.0
24.5
x_2 (mm)
49.5
50
50.5
51
x_1 (mm)

(a)

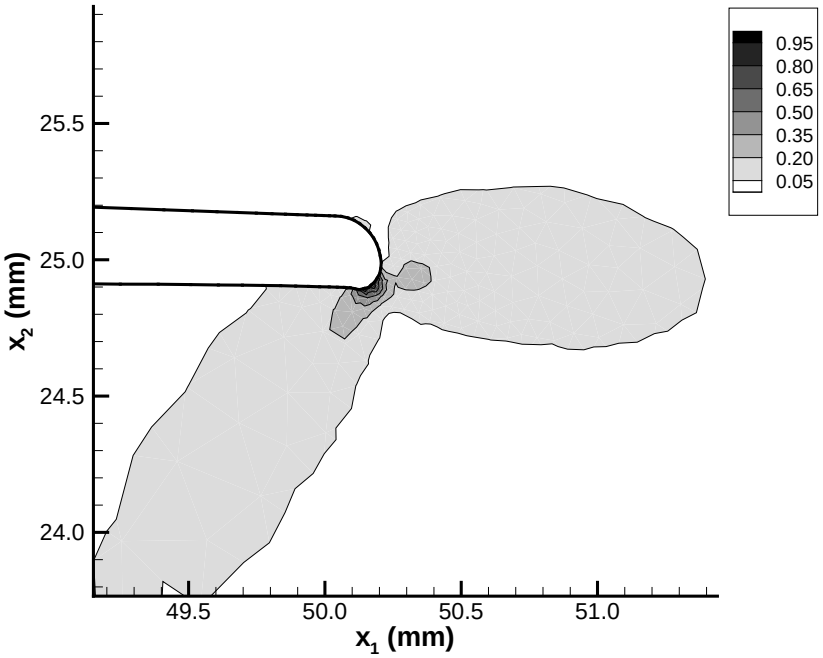
0.95
0.80
0.65
0.50
0.35
0.20
0.05
25.5
25.0
24.5
24.0
x_2 (mm)
49.5
50.0
50.5
51.0
x_1 (mm)

(b)

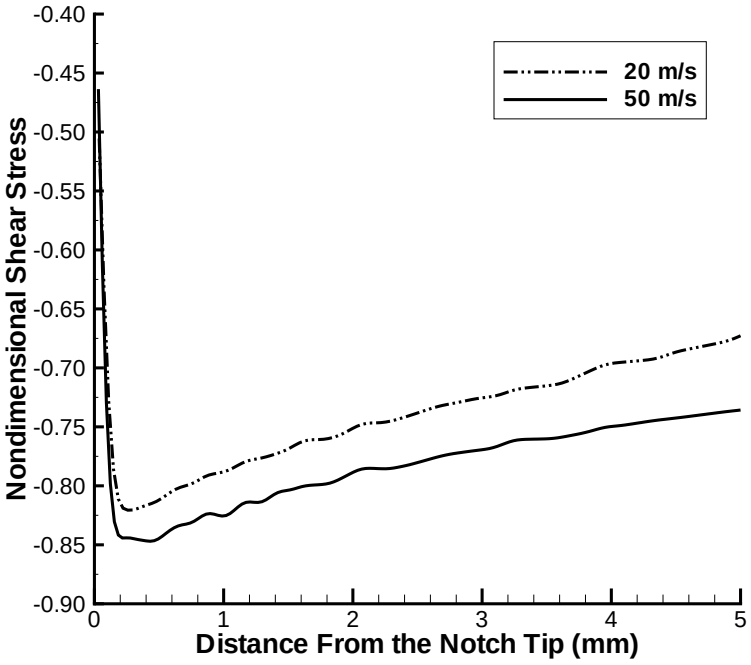

(c)

Figure 3.5. Contours of the (a) nondimensional maximum principal stress at $t = 18\mu$s for $v_o = 50$ m/s, (b) contours of $\varepsilon_e^p/\varepsilon_c$ at $t = 15.1\mu$s for $v_o = 60$ m/s, and (c) the variation of the nondimensional shear stress at points directly ahead of the notch tip.

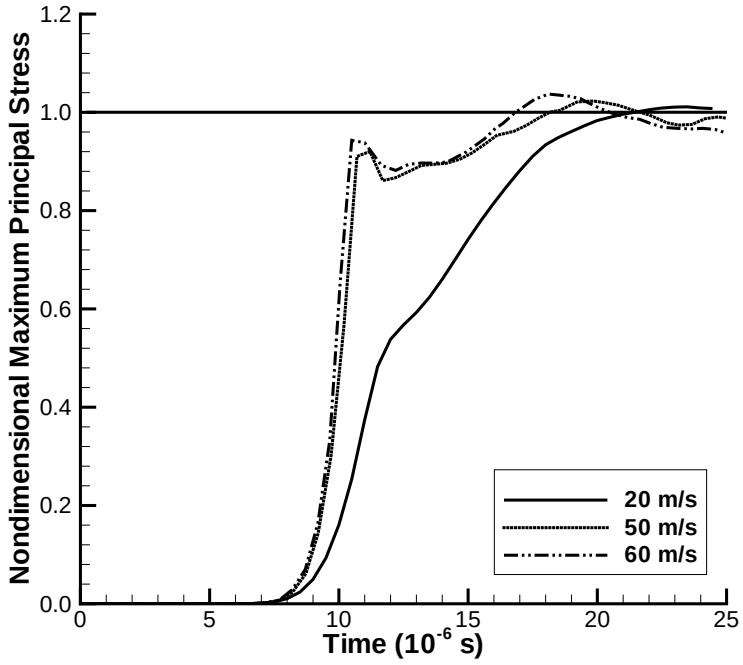

(a)

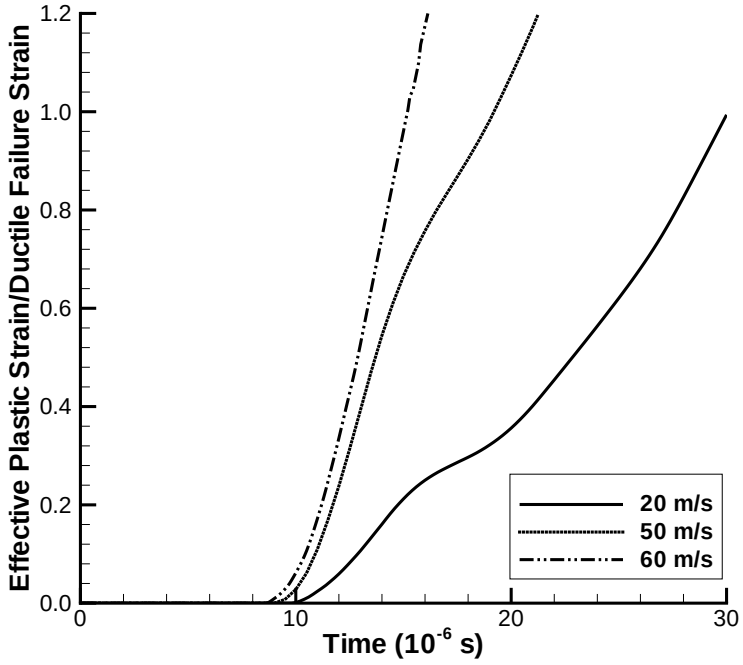

(b)

Figure 3.6. For $v_o = 20, 50$, and 60 m/s, the time history of the evolution of (a) the nondimensional maximum principal stress at point B and (b) $\varepsilon_e^p/\varepsilon_c$ at point D.

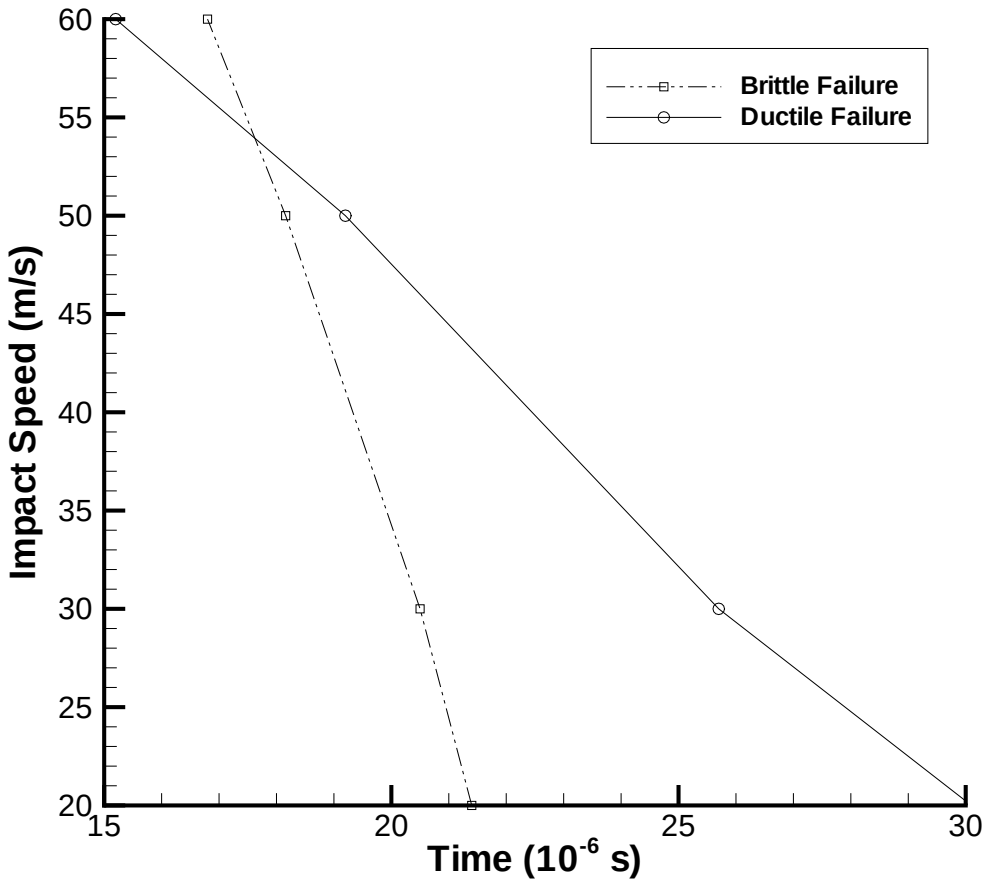

Figure 3.7. The dependance of the time of intiation of the brittle and the ductile fracture upon the impact speed, v_o.

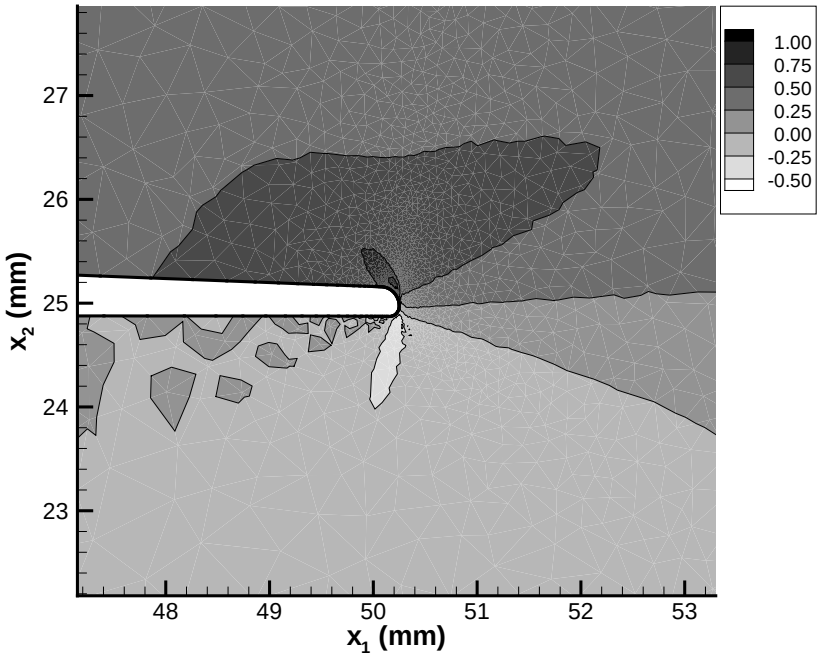
1.00
0.75
0.50
0.25
0.00
-0.25
-0.50
27
26
25
24
23
x2 (mm)
48
49
50
51
52
53
x1 (mm)

(a)

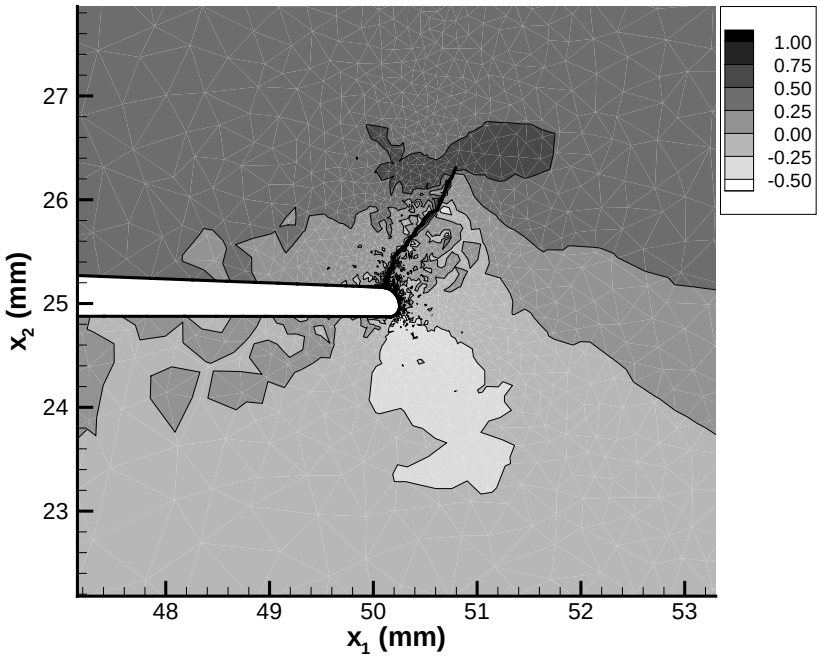
1.00
0.75
0.50
0.25
0.00
-0.25
-0.50
27
26
25
24
23
x2 (mm)
48
49
50
51
52
53
x1 (mm)

(b)

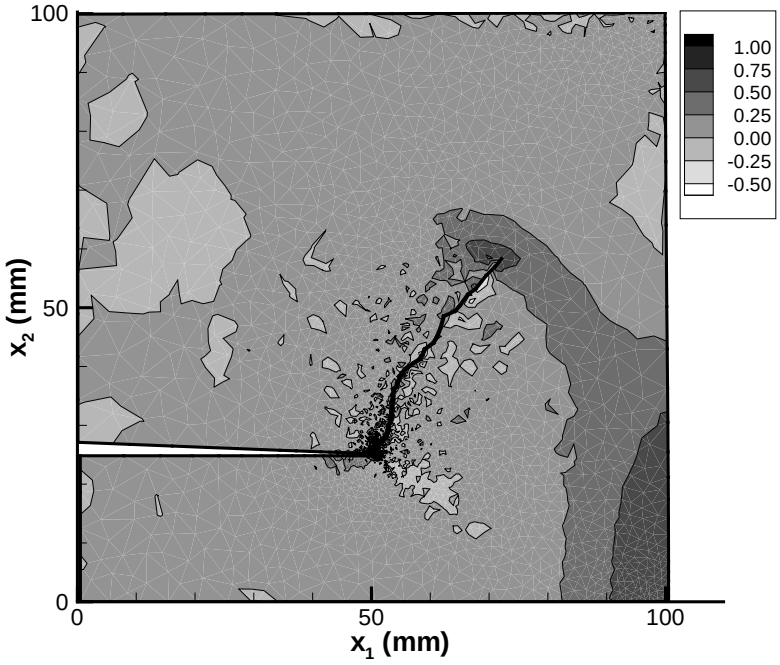

(c)

Figure 3.8. For $v_o = 20$ m/s, contours of the nondimensional maximum principal stress around the notch tip at $t = 20\mu$s (a) without and (b) with the opening of a crack at the point where brittle failure initiates. (c) For $v_o = 20$ m/s, contours of the nondimensional maximum principal stress at $t = 45\mu$s with the opening of a crack at the point where brittle failure initiates.

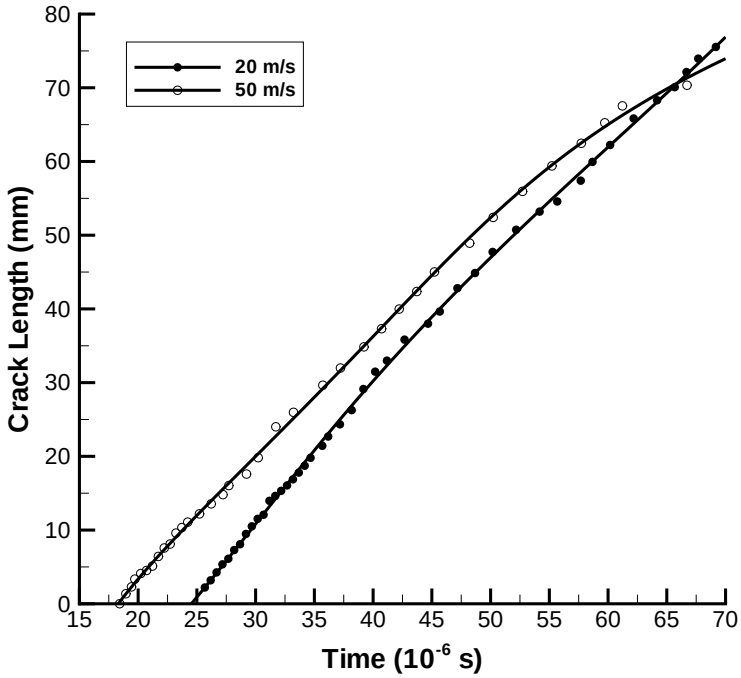

(a)

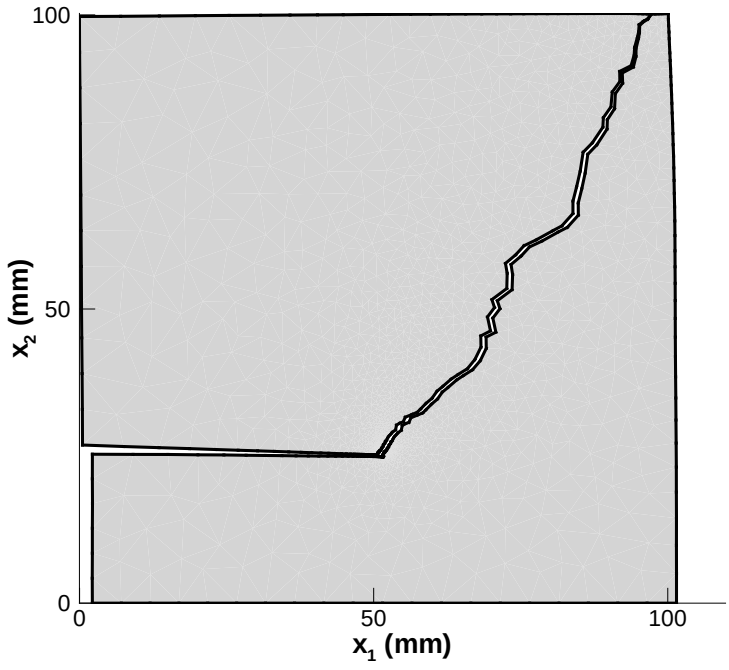

(b)

Figure 3.9. (a) The time history of the crack length for brittle failure for $v_o = 20$ m/s and $v_o = 50$ m/s and (b) the deformed shape of the plate at $t = 100\mu$s for $v_o = 50$ m/s.

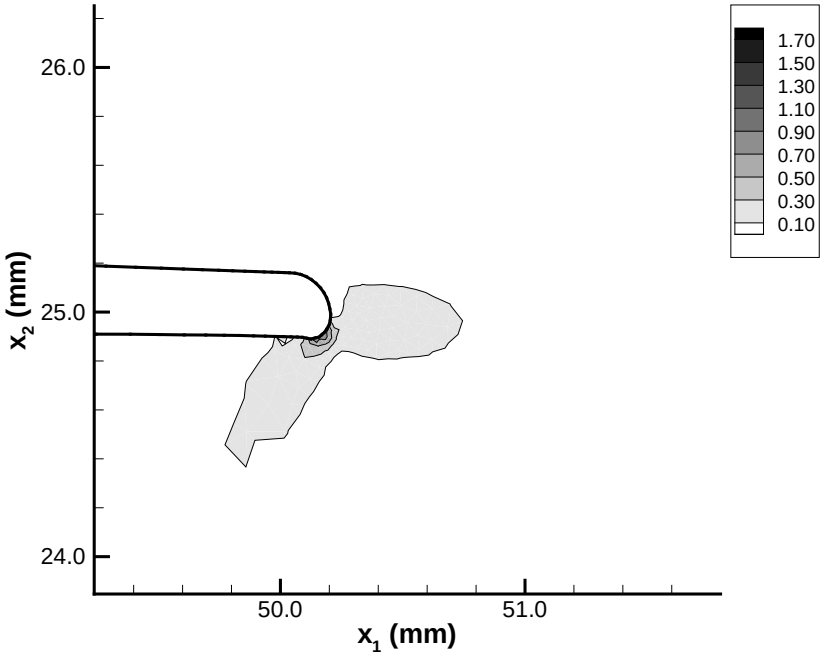
1.70
1.50
1.30
1.10
0.90
0.70
0.50
0.30
0.10
26.0
25.0
24.0
50.0
51.0
x2 (mm)
x1 (mm)

(a)

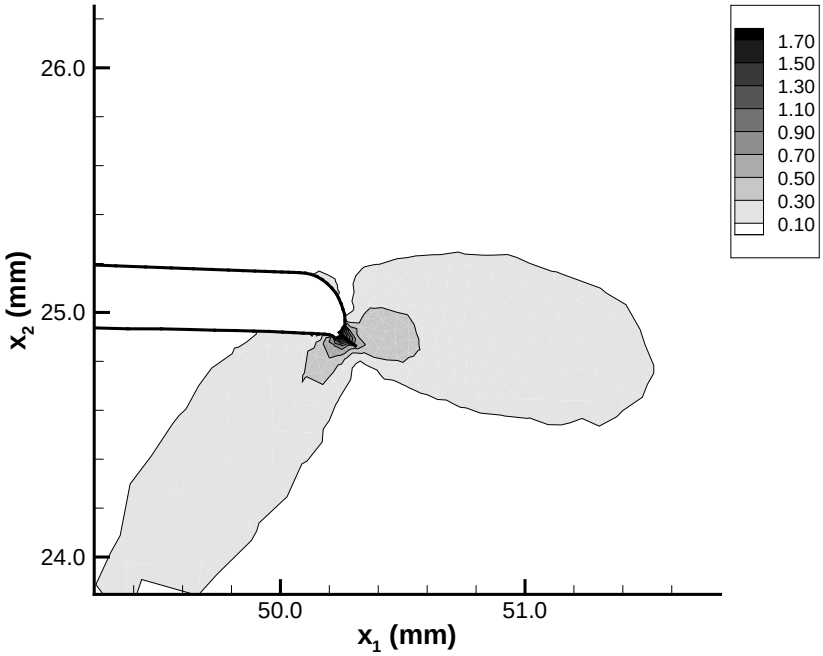
1.70
1.50
1.30
1.10
0.90
0.70
0.50
0.30
0.10
26.0
25.0
24.0
50.0
51.0
x2 (mm)
x1 (mm)

(b)

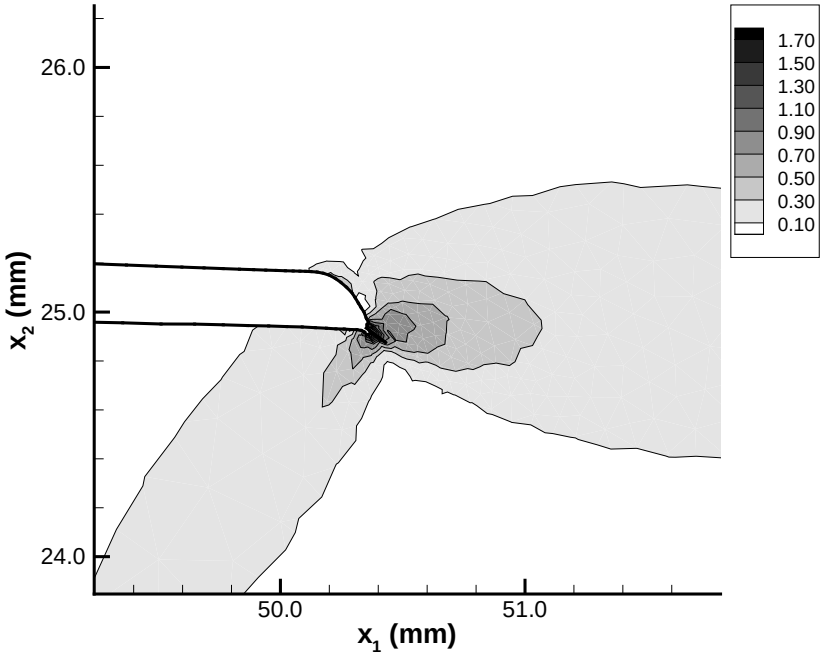

(c)

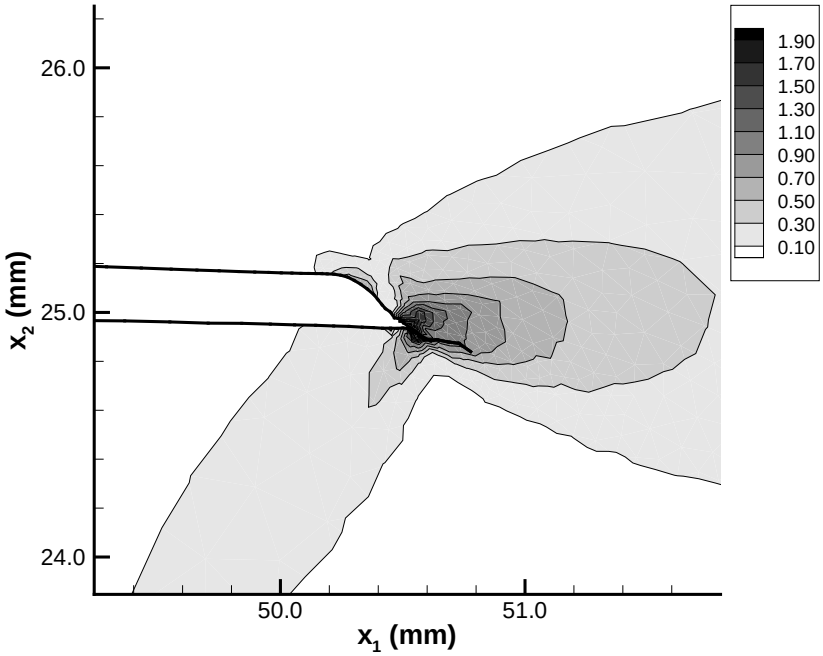

(d)

Figure 3.10. For $v_o = 60$ m/s, contours of $\varepsilon_e^p/\varepsilon_c$ in a small region around the notch tip at (a) $t = 15\mu$s, (b) $t = 21.5\mu$s, (c) $t = 28\mu$s, and (d) $t = 33.5\mu$s.

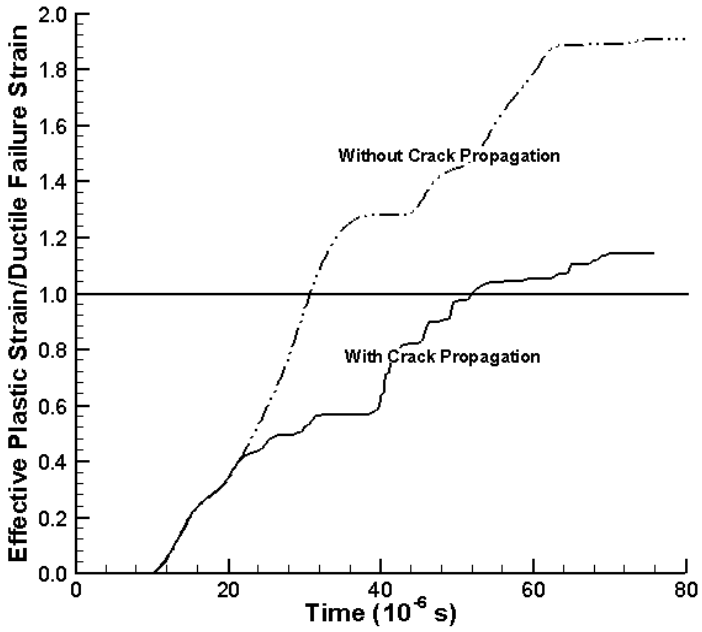

(a)

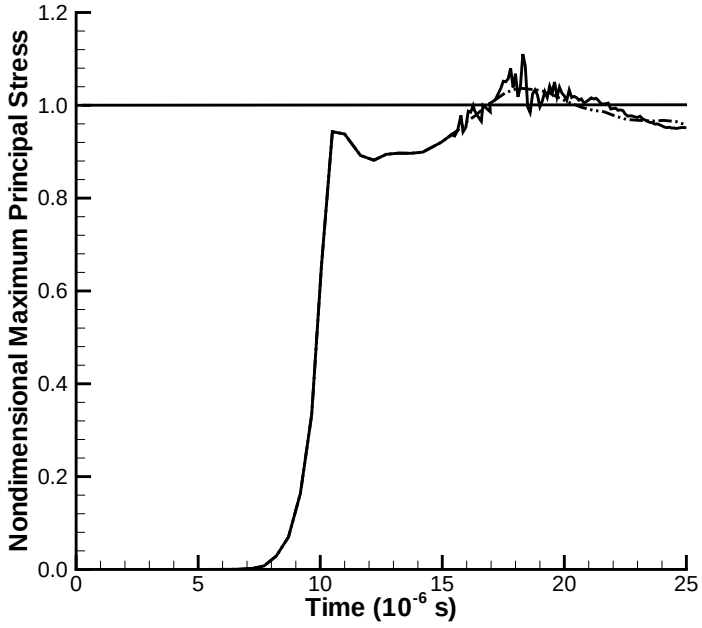

(b)

Figure 3.11. (a) The time history of $\varepsilon_e^p/\varepsilon_c$ at point D both with and without the opening of a crack at point B and (b) the time history of the nondimensional maximum principal stress at point B both with (solid line) and without (dotted line) the opening of a crack at point D.

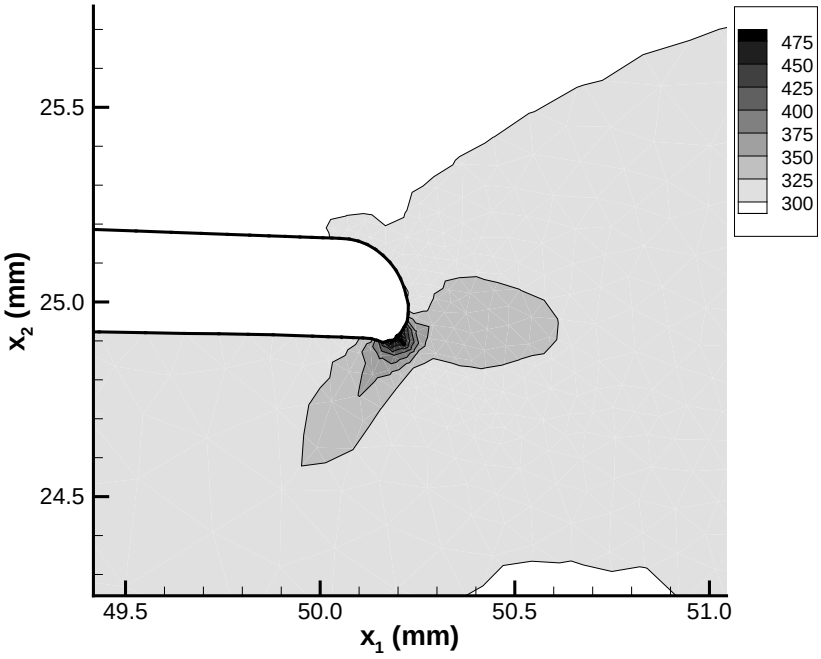

(a)

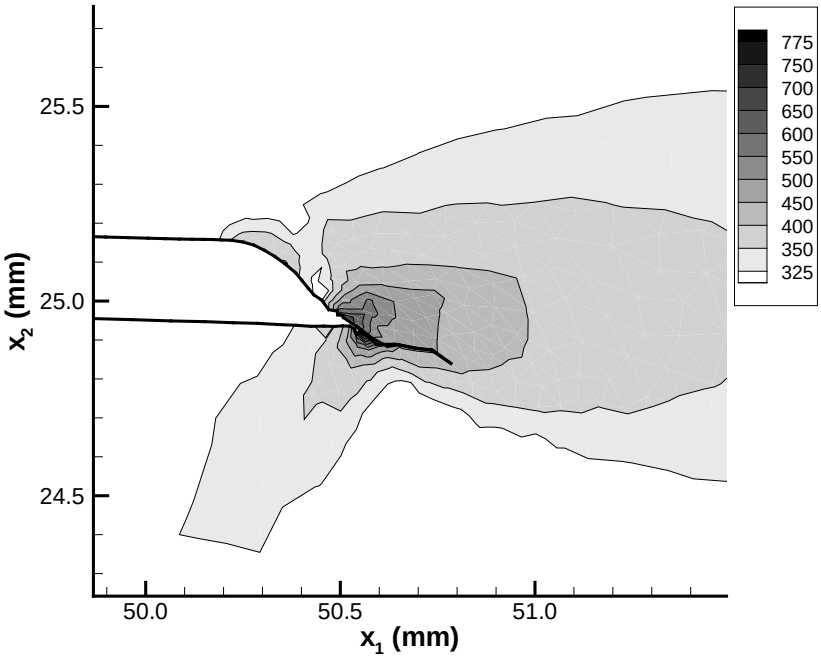

(b)

Figure 3.12. For $v_o = 60$ m/s, contours of the temperature rise in a small region around the notch tip at (a) $t = 17.1\mu$s, (b) $t = 33.7\mu$s.

Chapter 4

Contributions

4.1 Chapter 1

The work in Chapter 1 represents the first attempt to incorporate an elastoplastic material model into the MLPG method. The code was validated against existing FE solutions. It is found that nodal refinement is necessary when unloading and reloading occurs. It was also found that the penalty method cannot adequately enforce essential boundary conditions when used along the plane of a sharp crack and the error introduces oscillations in the deformations field about the crack tip. When the higher order extrapolation technique of Dally and Berger (1996) is used in this region the results are invalid; however, results from the log-log method are still reasonable. It is also found that for a small plastic zone (3% of the cracked length) the SIFs do not differ significantly from their values for the corresponding linear elastic problem.

4.2 Chapter 2

This work is the first to study the development of an ASB under plane strain tension with a hyperbolic heat equation (finite thermal wave speed). It was found that only for unrealistically small values of the thermal wave speed do the results differ signicantly from those with the parabolic heat equation. It is, therefore, concluded that for this type of problem a parabolic heat equation is justified. The ranking of eleven materials based upon their

susceptability to the formation of an ASB was completed and it was found that this ranking differed from previous work which considered simple shearing deformations. A parametric study of the effect of thermal conductivity, nominal strain-rate, and the initial defect strength for this configuration was also conducted. It is found that thermal conductivity, κ, does influence ASB initiation and propagation for materials with large values of κ and that for such materials an adiabatic model may not be adequate. The effects of initial defect strength and the nominal strain-rates were both found to be consistent with simple shearing studies except that the ASB propagation speed was found to decrease with increasing nominal strain-rate. To date there is no de facto criterion for ASB initiation and the lack of criterion has led to substantial confusion and in some cases questionable results. In this chapter, three common instability measures are compared. It was found that only that due to Batra and Kim (1992) accurately predicted the onset of global collapse.

4.3 Chapter 3

This chapter represents the first attempt to study the propagation of the brittle and the ductile fracture in an impact loaded double edge-notched specimen. Previous studies have only studied the initiation of the fracture and have not allowed its propagation. It is found that a propagating crack has a significant effect upon the stress field in the plate and acts to divert the stress concentration from the prenotch tip to the newly formed crack tip. This stress field is found to be consistent with the experiments of Kalthoff (2000). As in the experiments of Kalthoff (1987) and Kalthoff and Winkler (1987) the brittle fracture is found to completely perforate the plate. The ductile fracture is found to be coincident with the leaflet like opening that forms along the lower edge of the prenotch and that this leaflet is eventually incorporated in to the newly cracked surface. The leaflet was previously observed by Batra and Gummalla (2000). The failure mode was found to transition from the brittle mode to the ductile mode at an impact speed of approximately 54 m/s. This transition from brittle to ductile failure is consistent with previous experimental and numerical studies.

Vita

Mr. Lear was born January 28, 1970 in Lewistown, PA, USA. He graduated from the Pennsylvania State University with a B.S. in Aerospace Engineering in 1992. After graduation, he worked as a defense consultant to the United States Air Force (USAF) until 1993 when he began his masters studies. In 1996, Mr. Lear graduated from the University of Florida with an M.S. in Engineering Mechanics. He then began work as an Aerospace Engineer for the USAF at Eglin AFB, Florida where he was the technical representative to the drone aircraft development program. From 1997 through 1999, he worked as a Test Engineer for the munitions test division at Eglin. Mr. Lear started his doctoral studies at Virginia Tech in August of 1999 and graduated in May of 2003.